Terrafirma Extension

Technical Note

Algorithmic PSI Improvement in Mountainous Areas by Atmosphere Mitigation

DLR-IMF – Remote Sensing Technology Institute

prepared:

N. Adam Date

DOCUMENT CHANGE CONTROL

date	version	change
30.07.2012	1.0	- initial setup of document
17.08.2012	2.0	- finished document structure - conversion into new word-format for bibliography
21.08.2012	2.1	- changed structure of section 3 (troposphere effects in PSI)
07.09.2012	2.2	- added initial section on error propagation in NWP method
11.09.2012	2.3	- separated section on rel. and abs. error prop. in NWP method - removed section on ray bending (unexpected result, needs check in numeric of simulation)
17.10.2012	2.4	- update for recent NWP results
26.10.2012	2.5	- added section on estimation from InSAR data - removed section on NWP error propagation
30.10.2012	2.6	- added preliminary summary
15.01.2013	2.7	- added section on GPS zenith path delay
21.01.2013	2.8	- added prediction of coherence gain
07.01.2013	2.9	- added section on processing workflow and algorithms
01.06.2014	3.0	- started error propagation assessment - changed mbar into hPa (i.e. SI conform unit)
08.010.2014	3.1	- updated error assessment in NWP - added all respective equations - replaced plots of absolute error assessment - added tables with expected hindcast accuracy - complemented tables in appendix
14.10.2014	3.2	- fixed typo - added correction of integration path length in LOS path delay (in sec. 8.1.2)
27.11.2014	3.3	- incorporated feedback from Tim Wright - fixed equation 7

TABLE OF CONTENTS

1 LIST OF ACRONYMS AND ABBREVIATIONS

DEM	digital elevation model
EPN	European permanent network
EUREF	geodetic reference network for Europe
GNSS	global navigation satellite system
InSAR	SAR interferometry
NWP	numerical weather prediction
PS	persistent scatterer
PSI	persistent scatterer interferometry
SRTM	shuttle radar topography mission
TN	technical note
WAP	wide area product

2 LIST OF FORMULA SYMBOLS AND UNITS

symbol	description	unit
C_I	covariance matrix of sum of segment integrals	
C_{SII}	covariance matrix of segment integrals	
d_*	range error of the respective component	m (or mm)
$e_w\ (P_w)$	partial water pressure	hPa
h	topography height	m
H_r	relative humidity	percent
$I_{Dry}[i]$	integral over the dry refractivity component for the section with index i	mm
$I_{total}[i]$	integral over the wet and dry refractivity component for the section with index i	mm
$I_{Wet}[i]$	integral over the wet refractivity component for the section with index i	mm
n	index of refraction	dimension one
N	refractivity	dimension one
N_r	scaled up refractivity	dimension one
P_{tot}	total pressure (sum of partial pressures of mixed gases)	hPa
P_d	partial pressure of dry air	hPa
$Q_{Kg/Kg}$	water vapour mass mixing ratio	dimension one
$\vec{r}$	three dimensional line of sight vector (LOS)	$(m,m,m)^T$
t	time	s
T_K	temperature	°K
T_C	temperature	°C
Δh	topography height difference	m
ϑ	incidence angle	rad
σ_N^2	variance of estimated refractivity	no unit
$\sigma_{P_{tot}}^2$	variance of hindcast total pressure	hPa^2
$\sigma_{Q_{Kg/Kg}}^2$	variance of hindcast water vapour mixing ratio	$(Kg/Kg)^2$

$\sigma^2_{T_K}$	variance of hindcast temperature	$°K^2$
φ	interferometric phase	rad

3 INTRODUCTION

This technical note (TN) focuses on the assessment of the atmospheric effects and their compensation in SAR interferometry and especially in persistent scatterer interferometry (PSI). Different strategies to reduce atmospheric effects exist for mountainous areas. These methods are compared and the related assessment is described in this technical note. The output is a recommendation how to implement the atmosphere mitigation in mountainous areas. In practice, this assessment has a significant impact on the estimation precision and finally (similar to the GPS- based calibration) on the sustainability of the WAP.

In principle, the topographically-correlated atmospheric phase can be estimated [1]

- directly from the data,
- from global coarse grid GPS zenith path delay data [1] [2] and
- from numerical weather prediction models (NWP) [3] [4].

Each of these methods has its characteristic, advantages and limitation. In detail, the GPS zenith path delay is a direct measurement of the path delay and a by-product of the routine GPS orbit determination process. The numerical weather prediction is a physics model based interpolation (hindcast) into a finer temporal and spatial resolution from coarse atmosphere state data. The hindcast provides practically temperature, total pressure and water vapour mixing ratio which are indirect parameters. These need to be transferred based on an empirical model into a refractivity and consequently into a path delay. In contrast to this complicated method, the direct estimation based on interferometric phase data is straight forward to implement and does not require additional atmosphere state or GPS data. The Greece wide area product (WAP) is used as a test case for the demonstration and the assessment of the characteristic of each method in this report.

This document starts with a description of the atmospheric signal components and their characteristics. Afterwards, the straight forward estimation of the expected stratification based on interferometric phase data is described and demonstrated. In a brief section, the estimation from available GPS zenith delay data is presented. However, the NWP based troposphere effect mitigation is actually considered the state of the art. Several algorithms and their error propagation are described in the main section of this report. In order to support the error propagation assessment, the precision and accuracy of the WRF hindcast is checked using independent sounding data. Sounding is a direct measurement of the atmosphere state variables with a high vertical resolution. The comparison finally provides an estimate of the expected standard deviation of the WRF hindcast output parameters which are the basis for the prediction of refractivity and path delay and need consequently be considered in the error propagation assessment. The demonstration of the actual atmosphere mitigation implementation concludes this report.

4 TROPOSPHERE EFFECTS IN PSI

The troposphere induced phase in a single radar acquisition is a result of wave propagation effects along the line of sight (LOS). These can be quantified as a one way distance change d_{atmo} (excess path or propagation range error) and is given by:

$$d_{tropo} = R_g - R_0 \quad (1)$$

In the equation above, R_0 describes the pure theoretical (i.e. wave propagation in vacuum) range distance and R_g the observed range distance (i.e. optical propagation in atmosphere). Actually, the dominant effect for the wave propagation is the refraction in the troposphere. Practically, two things can be observed as a result of refractivity. On the one hand, a bending of the path $d_{bending}$ and on the other a change in the speed of the radar wave $d_{velocity}$ results.

$$d_{tropo} = d_{velocity} + d_{bending} \quad (2)$$

Both effects ($d_{velocity}$ and $d_{bending}$) increase the distance with respect to the theoretical wave propagation. For the first term $d_{velocity}$ in the equation (2), we measure an increased distance, because a constant speed of light is assumed for the propagation of the radar wave in the atmosphere in all SAR and InSAR processing steps. In practice, the speed of light

$$c = 299792458\,m/s \quad (3)$$

is typically used in geometry computations. However, the speed of a radar wave v_w is reduced by the index of refraction n

$$v_w = c/n \quad (4)$$

The well-known equation

$$c = \lambda \cdot f \quad (5)$$

describes the relation between the speed of light, the wavelength λ and the frequency f. Actually, the wavelength is shorter in a pathway compared to the vacuum. However, the frequency f of the wave remains constant.

The second term $d_{bending}$ in the equation (2) is a geometrical effect. The bending (visualized in Figure 1) is a result of a wave's passing from one medium into another with a different index of refraction n. The change of direction (i.e. the angles θ_1, θ_2 with respect to the boundary layer normal) is given by Snell's law:

$$\frac{\sin\theta_1}{\sin\theta_2} = \frac{n_2}{n_1} = \frac{v_{w1}}{v_{w2}} \quad (6)$$

In SAR interferometry, the bending effect $d_{bending}$ is typically neglected [5].

This is the reason, the range error d_{tropo} can be approximated by the integrated refractivity $N(\vec{r})$ along the LOS $\vec{r} = [longitude, latitude, height]^T$ of the radar beam from the scatterer $\vec{R}_{scatterer}$ to the sensor location $\vec{R}_{sensor}$:

$$d_{tropo} \approx d_{velocity} = 10^{-6} \cdot \int_{\vec{R}_{scatterer}}^{\vec{R}_{sensor}} N(\vec{r}) d(\vec{r}) \quad (7)$$

It is computed from the scaled-up atmospheric refractivity $N(\vec{r})$ which is defined based on the atmospheric refractive index $n(\vec{r})$:

$$N(\vec{r}) = 10^6 \cdot [n(\vec{r}) - 1] \quad (8)$$

Neglecting the frequency dependence of the refractivity $N(\vec{r})$, it can be parameterized by the Smith-Weintraub equation [6]:

$$N(\vec{r}) = k_1 \cdot \frac{P_d(\vec{r})}{T(\vec{r})} + k_4 \cdot \frac{P_c(\vec{r})}{T(\vec{r})} + k_2 \cdot \frac{e_w(\vec{r})}{T(\vec{r})} + k_3 \cdot \frac{e_w(\vec{r})}{T^2(\vec{r})} \quad (9)$$

It reveals the two main components i.e. the dry and wet part of the atmosphere influencing the refractivity:

$$N(\vec{r}) = N_{dry}(\vec{r}) + N_{wet}(\vec{r}) \quad (10)$$

In equation (9), the dry air components $N_{dry}(\vec{r})$ are described by the partial pressures of dry air (i.e. nitrogen and oxygen but without carbon-dioxide) P_d and of carbon-dioxide P_c . In contrast, the wet component $N_{wet}(\vec{r})$ is described by the water vapour partial pressure e_w. All refractivity components depend on the actual temperature T. The coefficients k_{1-4} in equation (9) are fitted from observations.

Equation (9) models the dominant effects only and consequently the influence of liquid water (e.g. rain drops) $N_{liquid}(\vec{r})$ is ignored. In order to model the refractivity completely, the liquid water effect needs to be considered:

$$N(\vec{r}) = N_{dry}(\vec{r}) + N_{wet}(\vec{r}) + N_{liquid}(\vec{r}) \quad (11)$$

Because SAR includes a two way propagation of the radar wave, phase and excess path are related by

$$\varphi_{tropo}^{idx} = \frac{4 \cdot \pi}{\lambda} \cdot d_{tropo}^{idx} \quad (12)$$

Practically for the troposphere, the dry φ_{dry}^{idx} (also named hydrostatic atmosphere), the wet φ_{wet}^{idx} atmosphere and the liquid water content φ_{liquid}^{idx} influence the slant range distance due to the change in refractivity along the LOS.

$$\varphi_{tropo}^{idx} = \varphi_{dry}^{idx} + \varphi_{wet}^{idx} + \varphi_{liquid}^{idx} \quad (13)$$

Both i.e. the dry and the wet phase component are the main error source for InSAR applications due to their spatial and temporal characteristic. Practically, the dry atmosphere does not change significantly over time scales of hours to days. However, it

has a strong dependence on the topography which is made extremely spatially variable due to layover during the radar mapping. In contrast to the temporally relatively static dry atmosphere, the wet atmosphere component is spatially and temporally very dynamic. Section 5 provides more detailed information on their characteristics.

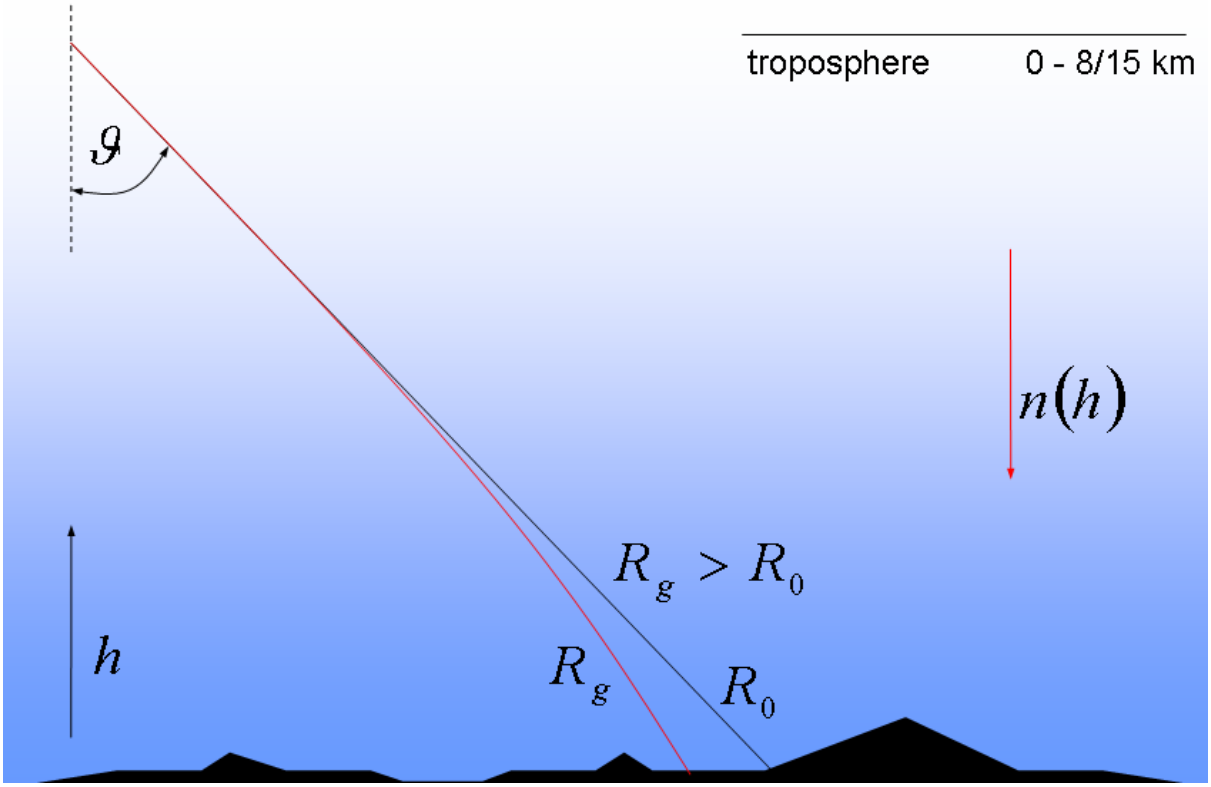

Figure 1: The density of the air changes with altitude and result in a change of refractivity. Snell's law states that radar waves are bent toward the denser gas. In this figure, arrows point into direction of increasing values.

5 CHARACTERISTIC OF THE ATMOSPHERE SIGNAL COMPONENTS

In this section, the implemented Troposphere Effect Mitigation Processor (TEMP) is used to demonstrate the characteristic of the generated data. An appropriate test site is the Island of Crete in Greece. The concrete area is visualized in Figure 2 together with the along track direction and the radar illumination direction. Two aspects make this area interesting. On the one hand, maritime air includes lots of water vapour and the troposphere is spatially and temporally very dynamic caused by wind. On the other, significant topography (i.e. more than 2300 m height difference within the SAR scene) allows to describe atmosphere effects related to pure geometry i.e. topography. Indeed, the Island surrounding water areas cannot provide InSAR measurements. However, this area supports the demonstration of troposphere effects free of topography.

Figure 2: The red rectangle describes the test site ERS data stack location. It has a dimension of 100 x 100 km. The yellow arrows illustrate the along track and the range direction.

Once again, the troposphere affects the SAR acquisition deterministically. According to section 4, it increases the observed range distance due to a change in refractivity along the LOS. A problem is that the state of the troposphere at the time of acquisition is not precisely known in order to correct this systematic effect as is typically done with topography. Because atmosphere changes quickly in time, it needs to be handled as a random signal in repeated SAR acquisitions.

The mean radar brightness of the SAR scenes and the topography of the test site in radar geometry are visualized in Figure 3. The example SAR scenes have an acquisition time at 09:05:04.427 [UTC]. In the implemented TEM-processor, the NWP is generated for a time with a maximum deviation of 30 seconds. The reason is the temporal prediction sampling in steps of minutes. In this example, the simulated data are for the UTC 09:05:00 and the time deviation is only 4.43 seconds. In the following, pixel coordinates are in slant range and with respect to the factor of two oversampled master radar scene.

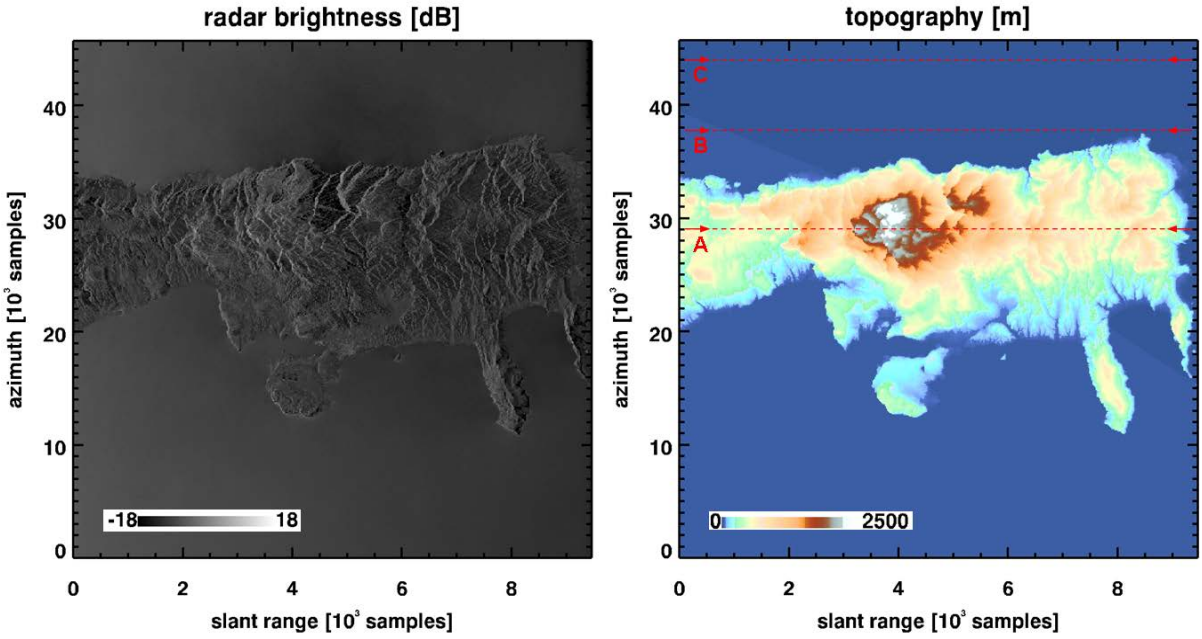

Figure 3: left: test site Crete radar brightness of SAR acquisition; right: topography in radar geometry. The red dotted lines A, B, B indicate the locations of the slices along range used in this section.

5.1 Spatial Comparison of Dry und Wet Air without Topography

As will be shown later, topography introduces a significant spatial effect on the mapping of troposphere effects into the radar image. In order to demonstrate the spatial characteristic of the dry and wet component it is advantageous to keep out the topography during the mapping of refractivity effects into the radar scene and use the WGS84 reference surface. However, the NWP still uses a coarse DEM and consequently it is necessary to extrapolate the atmosphere parameters of the lowest data layer onto the ellipsoid.

Figure 4 provides overlays of the dry and wet effect on the radar brightness i.e. in radar geometry. It allows to compare the spatial dynamic with respect to typical geo-features which change e.g. ground cover and topography. As a first impression, the dry air effect is spatially very smooth and correlates only little with the geo-features. Compared to this characteristic, the wet component has a higher spatial variation and correlation with ground cover and topography.

It is a typical characteristic for a scene that the range error of dry air d_{dry}^{idx} is as an absolute value much larger compared to the wet air effect d_{wet}^{idx}. Figure 5 directly compares both effects. In this example, the dry air component is very large with 2.8 m - 3.0 m compared to the wet air component d_{wet}^{idx} with 16 cm - 23 cm. In a single SAR observation, the dry air is the dominant effect and causes a significant range error in the geolocation. I.e. the scene is in range shifted by about three meters and scaled by 20 cm. In contrast, the wet component adds only a shift in the order of 20 cm. This example also demonstrates the systematic effect over range for the dry air which causes the

above mentioned scaling and is not important for the wet air. It is more clearly elaborated in Figure 6. In near range, the range distance is 831.6 km and in far range 869.0 km. This suggests that increasing the one way propagation path by 37.4 km causes ca. 20 cm more dry refractivity effect.

The wet air component does not show this range dependency. This suggests that the dry and wet air layers are differently thick. Namely, the dry air layer is significant in the spatial order of 20 – 30 km and the wet air is thin with 5-7 km only. It is confirmed by Figure 7. It visualizes the scaled-up refractivity computed from Eq. (9) for the wet (left) and dry (right) component for the vertical slice along the red line in the top figure. The stratification of the troposphere is clearly visible. Also the dry air is dominant due to its absolute value (i.e. up to 261 N-units) and the spatial vertical extension.

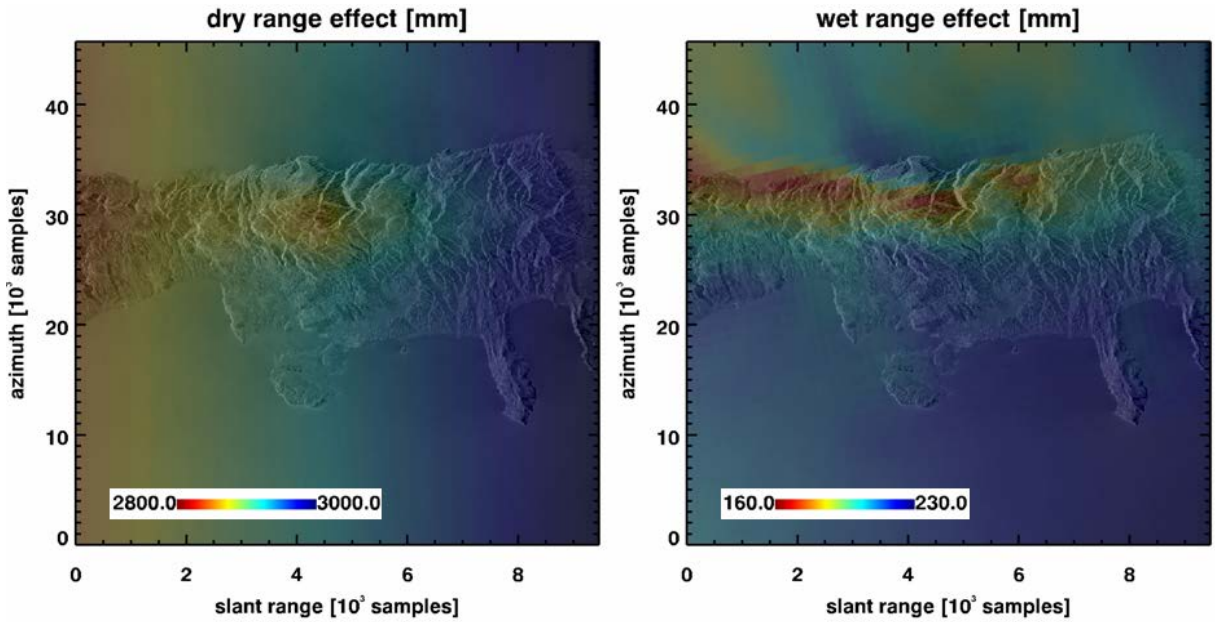

Figure 4: dry (left) and wet (right) troposphere effect without topography; only WRF uses topography. The visualisation is a superposition of the radar brightness and the respective troposphere effect.

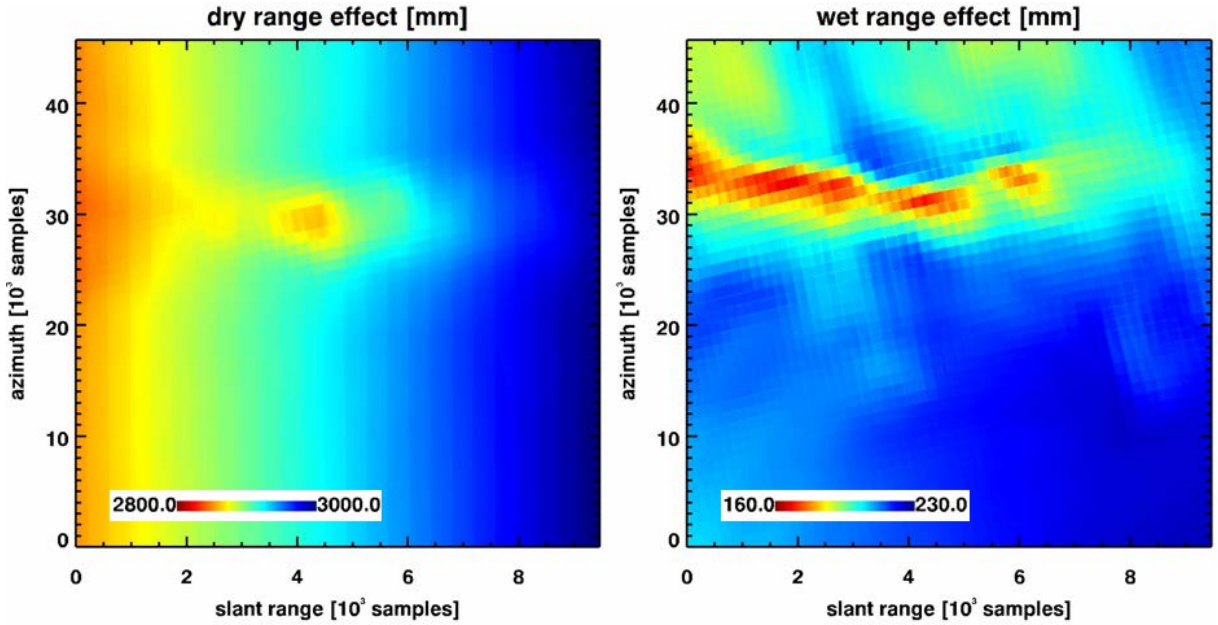

Figure 5: spatial variability of dry and wet component. left is dry: little spatial variation and dependency on ground cover but with topography; right wet: high spatial variation and correlation with ground cover and topography

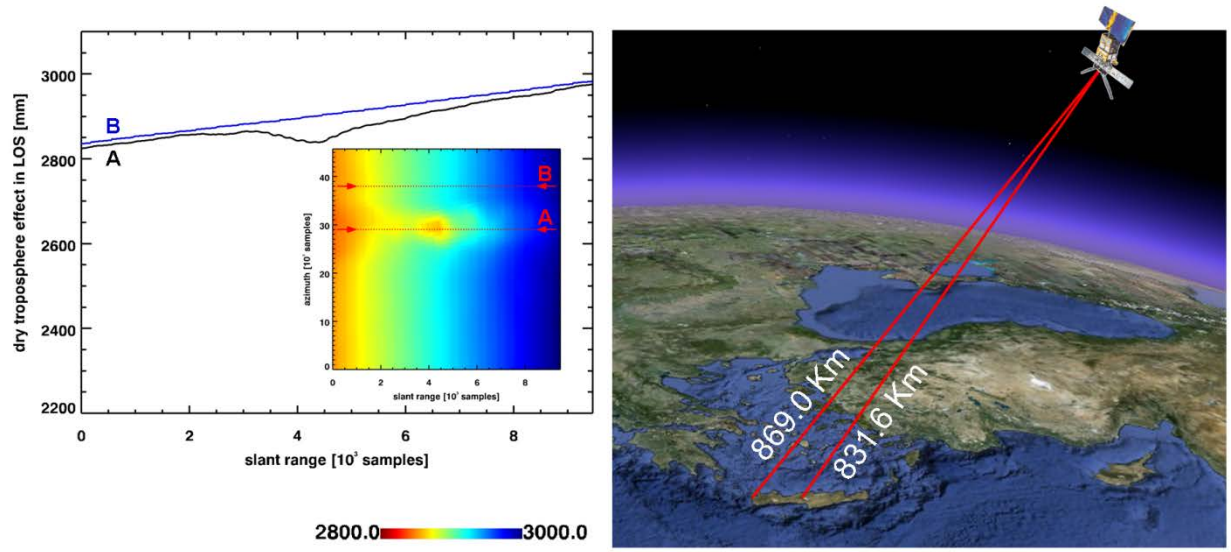

Figure 6: left: dry air caused systematic range error in a radar scene along slice A and B. The systematic effect is best demonstrated by slice B and is caused by the increase of range distance from 831.6 km to 869.0 km (Δ=37.4 km) from near to far range. Slice A also demonstrates error propagation which is related to topography. Details are given in this section. right: corresponding observation geometry

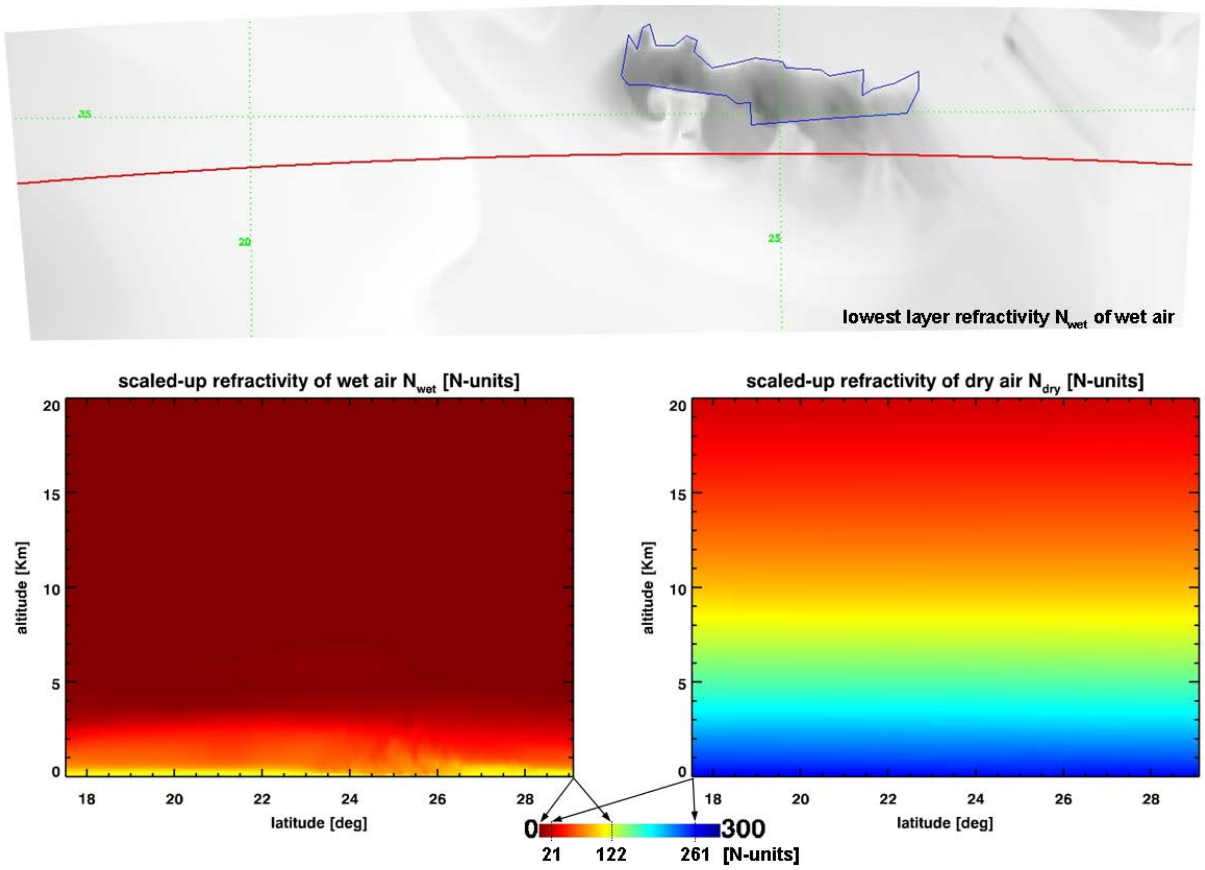

Figure 7: vertical spatial characteristic of N_{wet} above the ground, lower left and right: spatial characteristic of N_{wet} and N_{dry} component along the red line (top figure)

5.2 TEMPORAL COMPARISON OF DRY AIR WITHOUT TOPOGRAPHY

Weather is known to be temporally very variable with sometimes unpredictable behaviour. And consequently, no temporal systematic in these observations could be expected. However, there are periodic seasonal effects and fix physical circumstances e.g. stratification of atmosphere which even allow a characterisation using a standard atmosphere model. The relative temporal dynamic (i.e. related to its absolute value) of the dry air range error d_{dry}^{idx} is rather small. It becomes visible comparing two examples from winter and summer in Figure 8. It is difficult to observe a difference between the left and the right dry effect. Both seasons represent the atmosphere state with the most distinct parameters. However, the change itself is a clear effect in the interferometric measurement and needs to be compensated.

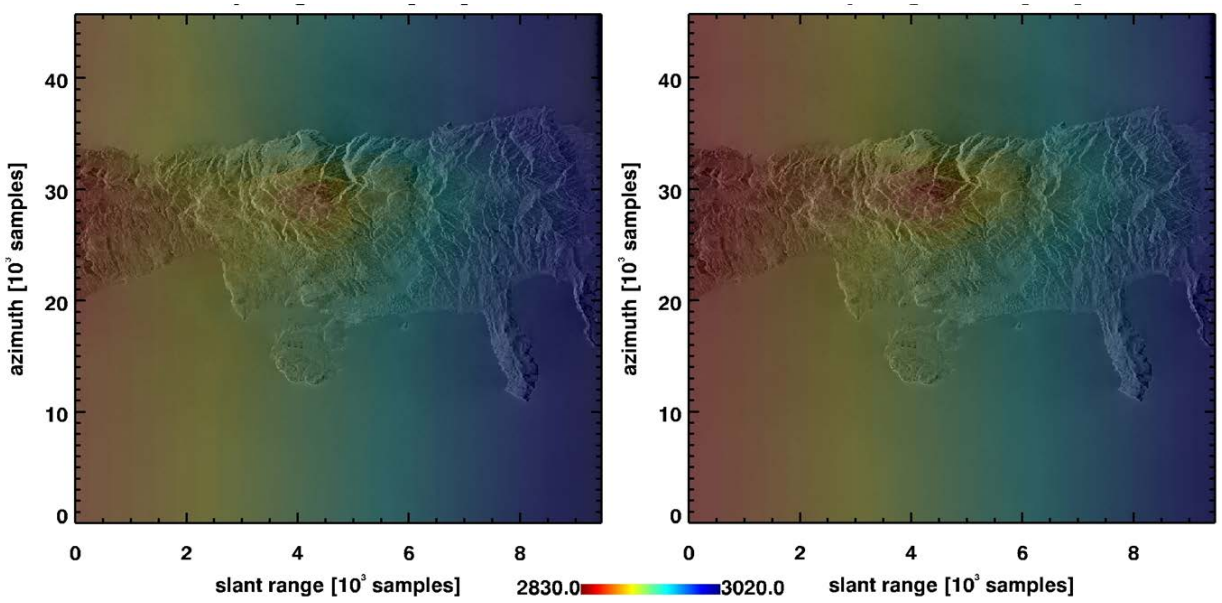

Figure 8: absolute value of the dry range effect in units of mm in winter (left) and summer (right) without the topography effect

5.3 TEMPORAL COMPARISON OF WET AIR WITHOUT TOPOGRAPHY

The absolute value of the wet effect is much smaller in winter compared to summer. In this example, the winter has a range delay of about 70 to 75 mm. In contrast the summer delay is in the order of 220 to 256 mm i.e. three times larger. The small spatial variation of only 5 mm in winter and 6 mm in summer over the 100 km x 100 km scene proves the fact, that the relative estimation in the PSI processing can compensate this effect in the estimation.

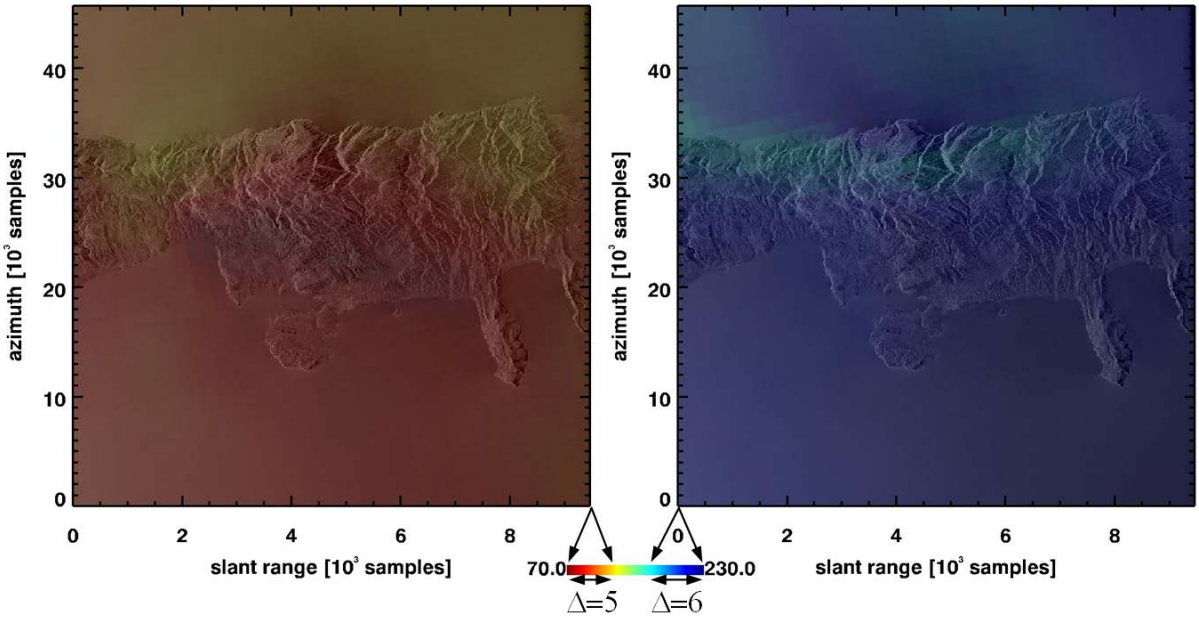

Figure 9: absolute value of the wet range effect in units of mm in winter (24. December on the left) and summer (24. July on the right). The variation (delta) is given in cm.

5.4 TOPOGRAPHY EFFECT CAUSED BY VERTICAL STRATIFICATION

Figure 7 visualizes the scaled up-refractivity and demonstrates the vertical stratification of the atmosphere. Topography intercepts these layers and consequently, the atmosphere signal is modulated according to the topography. Hence, the most dominant atmosphere effect and error source results for InSAR and PSI. Practically, this effect is systematic and can be compensated in case the topography and refractivity is known beforehand. Figure 11 provides an example for its severe variability in space (along a slice) and time (i.e. winter and summer season). Finally, this variability is the reason for the need to mitigate this effect. Even a relative estimation over short distance arcs in PSI cannot compensate this influence. Instead of one kilometre distance the maximum range between scatterers should be below 500 m. Typically, usable persistent scatterers in mountainous areas are not dense enough to generate a working reference network with such an arc length.

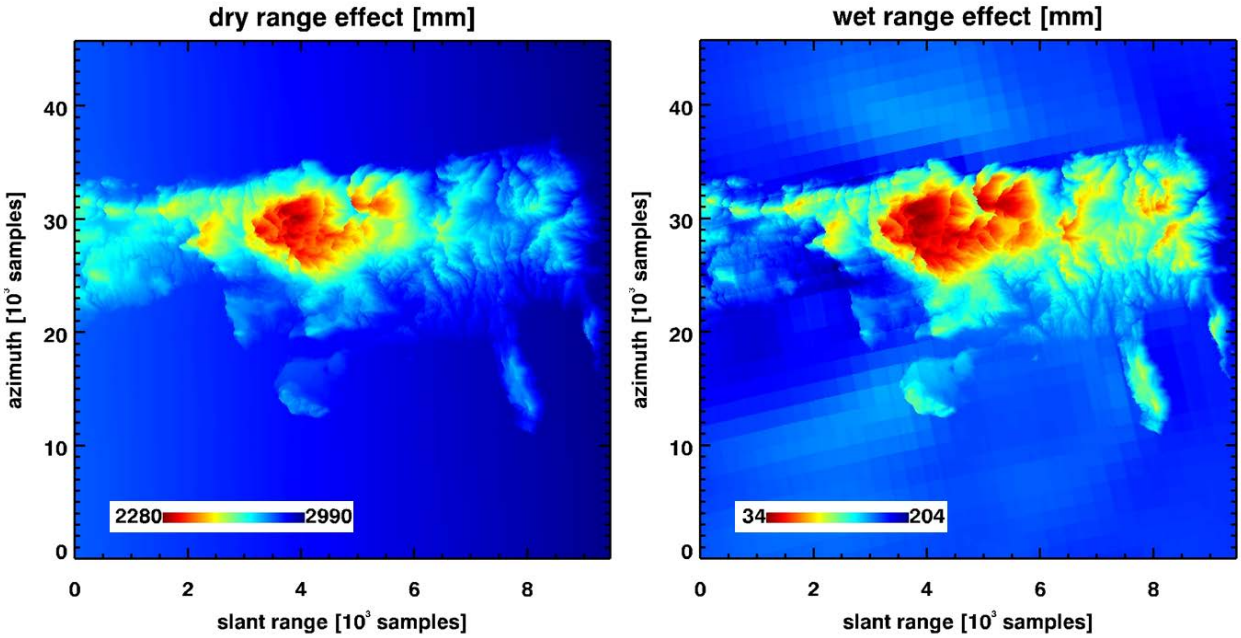

Figure 10: dry range effect (left) and wet range effect (right) which includes the topography effect. The topography is shown in Figure 3 and varies between sea level and 2500 m.

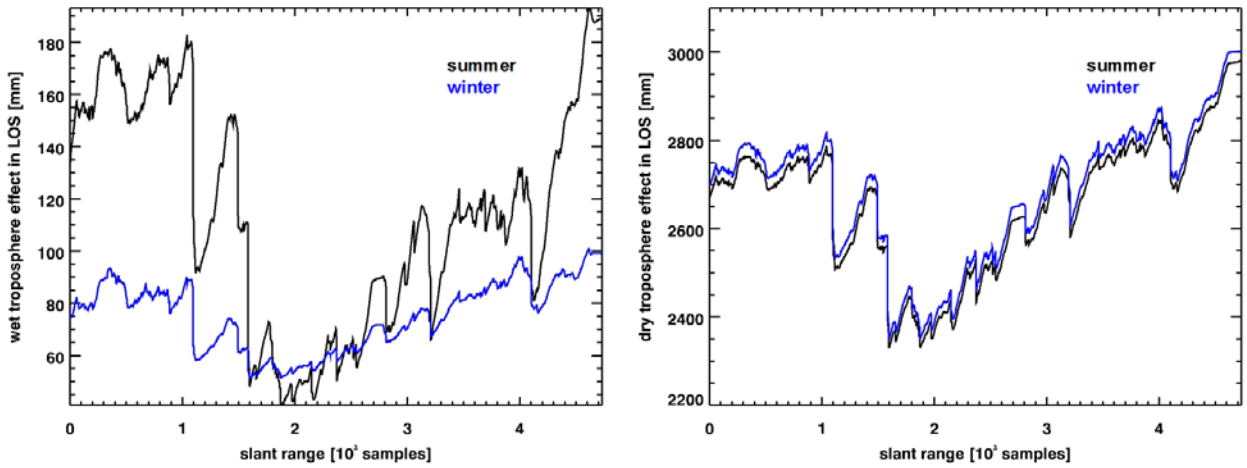

Figure 11: slice A with respect to Figure 3: single scene's troposphere ranging effect in LOS; left wet effect for a typical summer (black) and winter (blue) acquisition; right: dry effect for a typical summer (black) and winter (blue) acquisition

6 STRATIFICATION ESTIMATION FROM PSI DATA

With suitable data, the stratification effect can be directly observed in the interferometry data. Of course, this experience suggests a direct estimation of the effect from the data. In the following section, this straight forward estimation is demonstrated. Starting point is a stack of acquisitions from the Greece WAP (track 279, area around Larissa) which clearly includes the atmosphere stratification effect. The data set is visualized in Figure 12 to Figure 15 with its radar brightness, its topography and with differential interferograms which are compensated by a SRTM DEM. The second figure shows the DEM in the master scene's geometry. In this scene, the topography varies from sea level (blue) to 2000 m (white). The master scene (orbit 9652) has been acquired in winter season on 23. February 1997. In Figure 14, a summer scene's interferogram is visualized. It has an effective baseline of 25 m only. This is the reason, the residual phase could be caused by severe DEM errors or by an atmosphere effect. In order to clarify this characteristic, the interferogram in Figure 15 is needed. It is acquired in winter on the 19. January 1997 and has an effective baseline of 163 m. In case of DEM errors, it should show more residual phase because of the larger effective baseline. However, the interferogram is perfectly compensated for topography and it follows that the phase in the winter – summer interferogram is caused by an atmosphere effect. Especially, the strong relation to the topography allows the assumption that this is a suitable example for the vertical stratification effect. In the following section, the vertical stratification effect is estimated exemplarily for this interferogram and some randomly selected others.

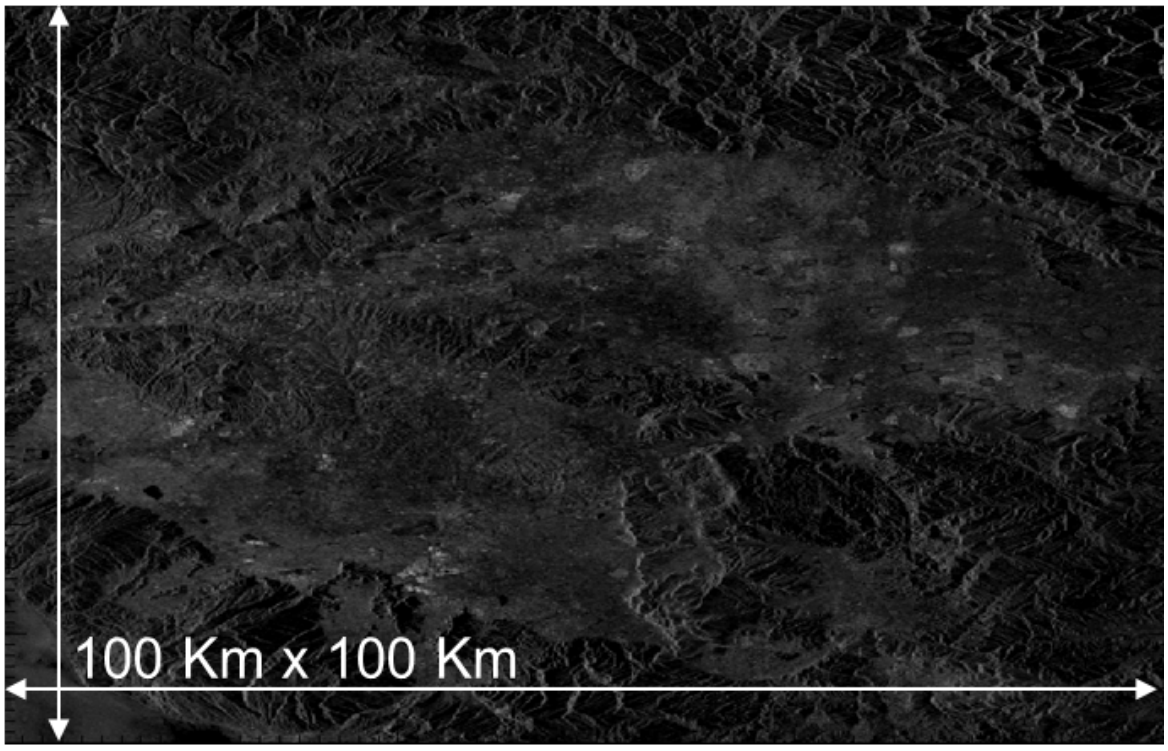

Figure 12: radar brightness of test data set for the demonstration of vertical stratification effect

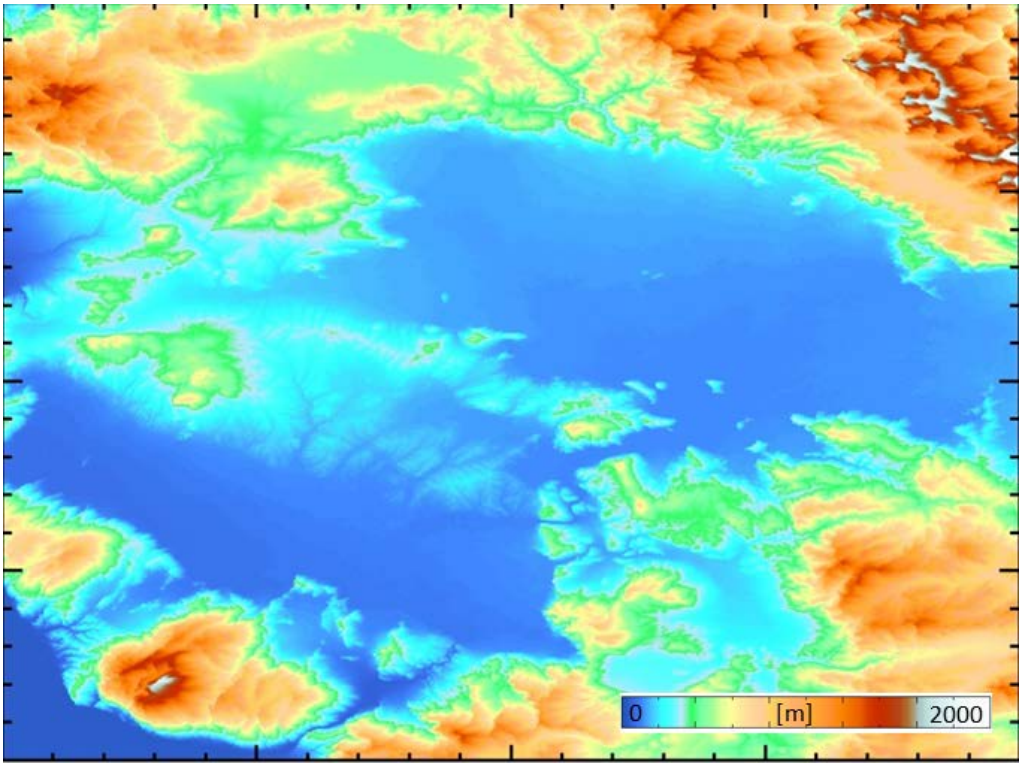

Figure 13: DEM in master scene's geometry of the example data set for the demonstration of vertical stratification effect

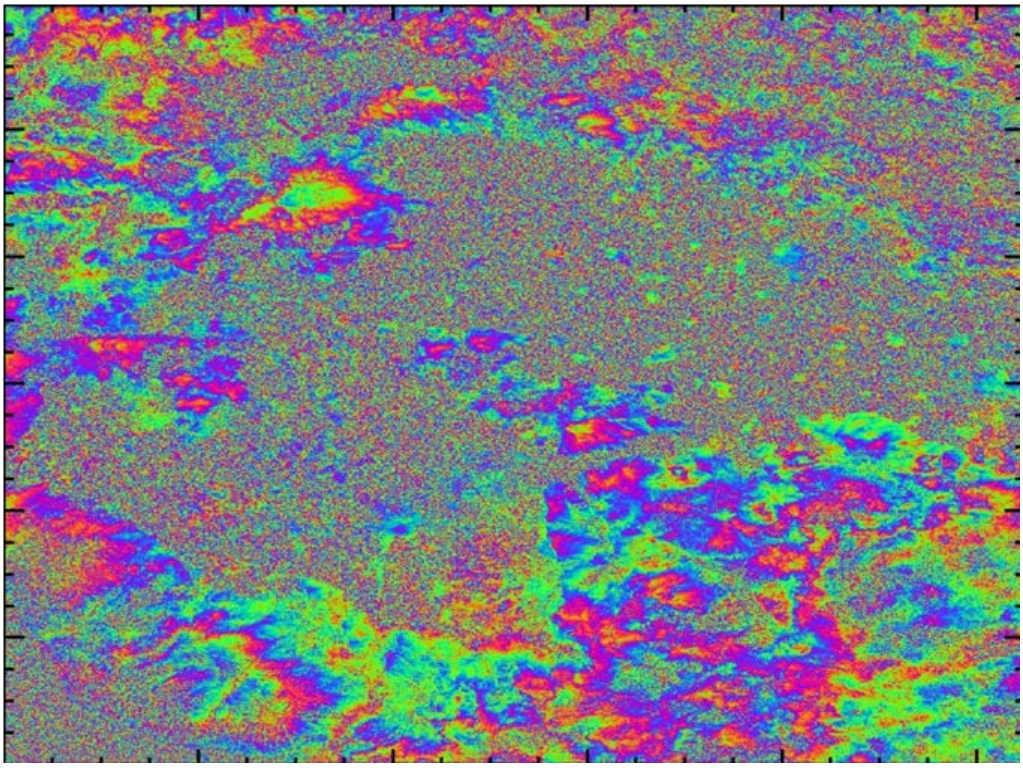

Figure 14: winter – summer and small baseline interferogram of the example data set for the demonstration of vertical stratification effect. The residual phase results from the vertical stratification effect.

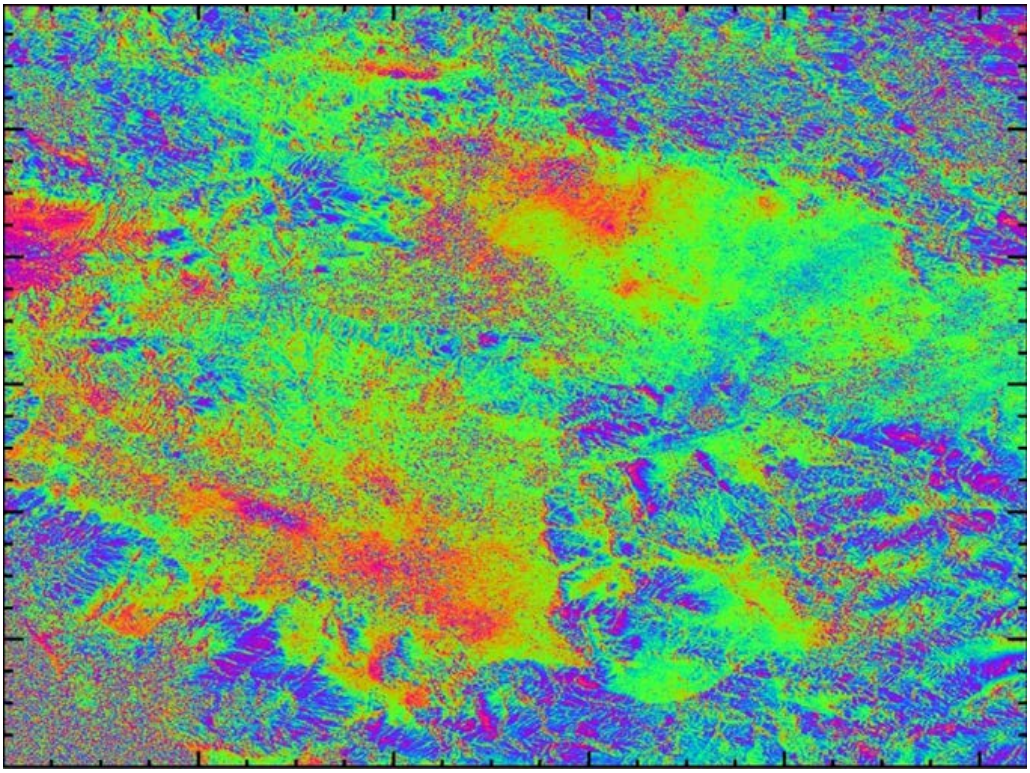

Figure 15: winter – winter interferogram of the example data set for the demonstration of vertical stratification effect

Different algorithms are possible for the estimation of the stratification effect compensation:

- Estimation from the full interferogram area using high coherence pixels only
- Estimation from a slice taken from a coherent mountain

Of course, a lot of variations are possible e.g. in averaging points and the selection of points for the processing to make the estimation more robust.

6.1 ESTIMATION FROM THE FULL INTERFEROGRAM AREA

The algorithm input is the interferogram, the coherence image and the DEM which is transformed into the master scenes geometry according to Figure 13. First, the most frequent height is determined using a histogram from the DEM as is shown in Figure 16. The estimation should be restricted to areas above this height. We are interested in a height variation and points below this height do not really support the estimation. In this example, the estimation is based on height values above 200 m.

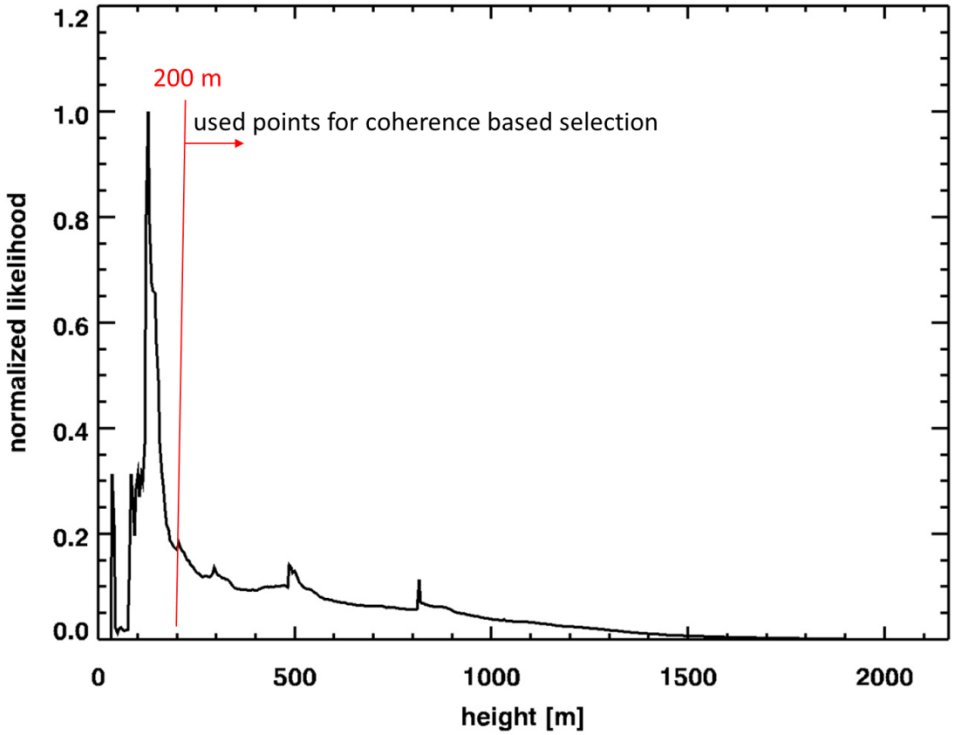

Figure 16: histogram of heights in the example

The next step is the selection of coherent pixels in the interferogram. For the regression, 1000 samples are a good basis. Finally, we want to fit a line with two parameters only and consequently a much smaller sample size could be sufficient. However, in order to get samples with a sufficient variation in height this sample size is supportive. Using a straight forward histogram from the coherence image, the cumulative distribution function (CDF) can be calculated. The respective plots are shown in Figure 17. From the CDF, the coherence threshold for the selection is found (in this example 0.78). Now, the phase values which fulfil the conditions of DEM height above 200 m and coherence above 0.78 can be extracted from the differential interferogram.

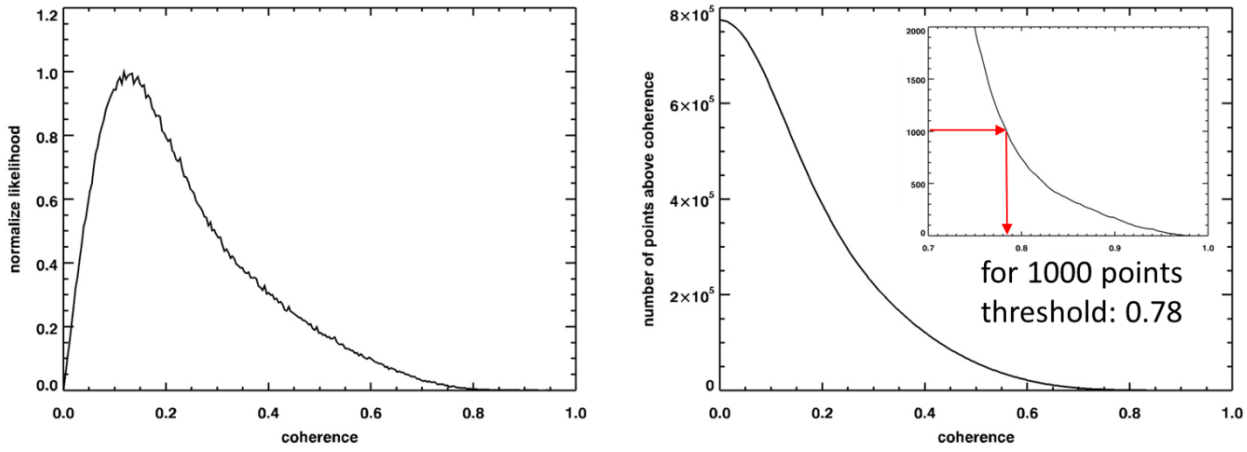

Figure 17: left: histogram from the coherence image for interferogram with slave 11155; right: the cumulative distribution function provides the coherence threshold above

The next estimation step is a robust regression of the DEM height with the respective absolute phase values. It is shown in Figure 18. For this reason, the relative interferogram values are unwrapped using an approximate line fit (green line in the figure). The relative interferogram phase values are compensated by an integer multiple of $2 \cdot \pi$ to be in the range of $[-\pi, +\pi[$ around the green line. As a result, the green absolute phase values shown in Figure 18 are available. These points are the input for a L1-norm based robust line fit. In this example, the atmosphere stratification phase φ_{tropo} [rad] depending on the height h [m] is fitted by:

$$\varphi_{tropo} = 5.84299 - h \cdot 0.00755264 \quad (14)$$

Finally, the PSI estimation needs to consider the height difference Δh [m] between two point scatterers only:

$$\Delta\varphi_{tropo} = -0.00755264 \cdot \Delta h \quad (15)$$

Practically, the estimation is based on points up to a height of 1200 m in this test case. However, the simple linear model allows to extrapolate and to compensate scatterers above this height. Finally, the compensation is quite effective. In this example a height difference of 800 m corresponds to an atmospheric effect of nearly $2 \cdot \pi$.

Using the DEM which is available in the master scene coordinates, the modelled atmosphere effect can be calculated by equation (15). The corresponding correction phase is shown in Figure 19. Due to the scene's topography, it spans a phase range of more than one cycle.

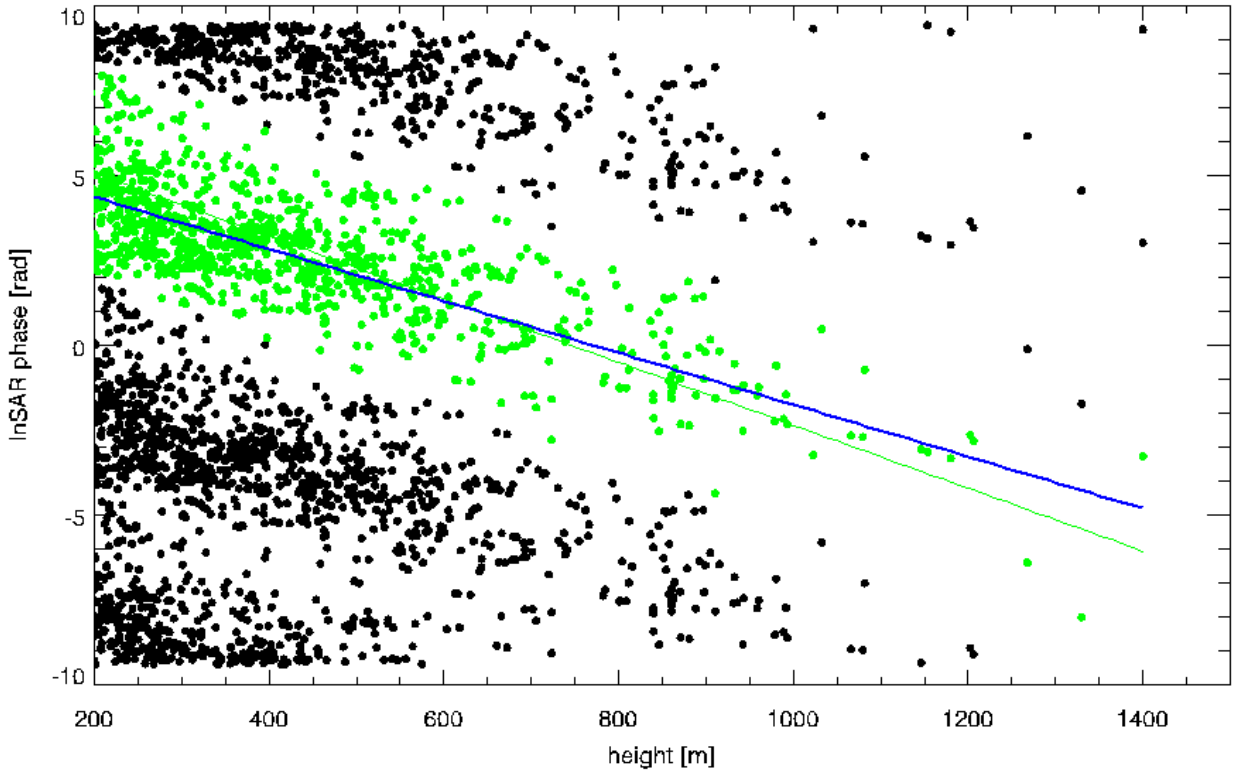

Figure 18: vertical stratification for interferogram with slave 11155 estimated from 1000 points with coherence above 0.78. The dependency is -0.75 rad per 100 m.

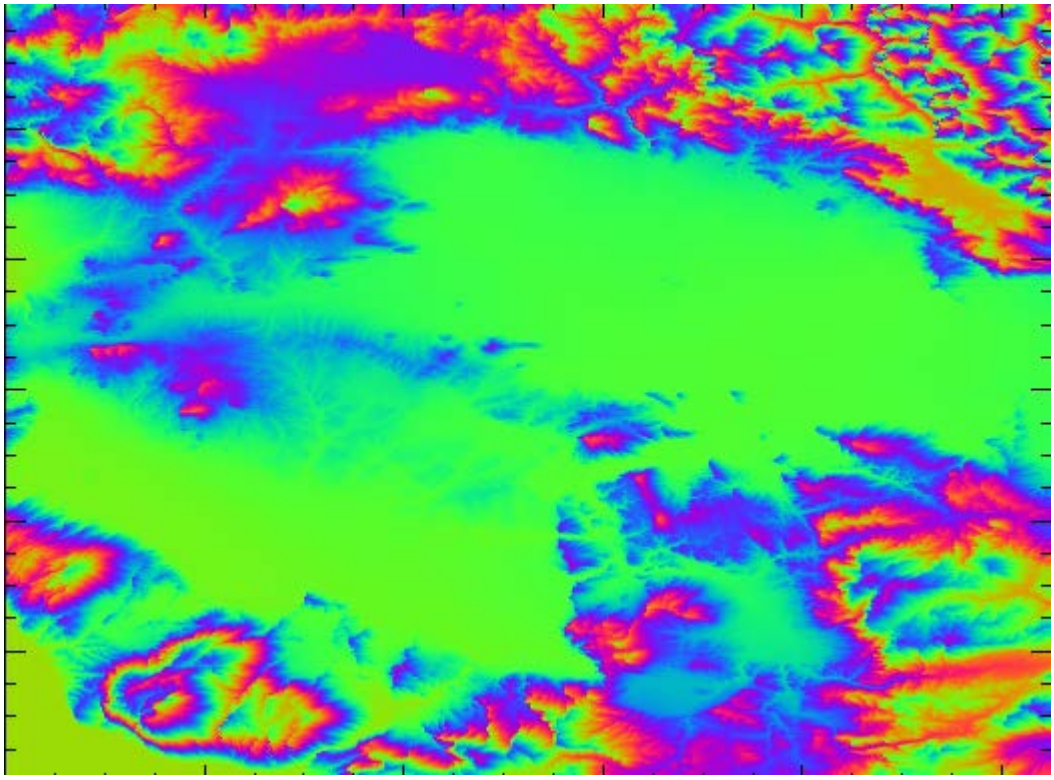

Figure 19: phase of the modelled atmosphere effect based on the estimation from Equation (15) for the interferogram with slave 11155

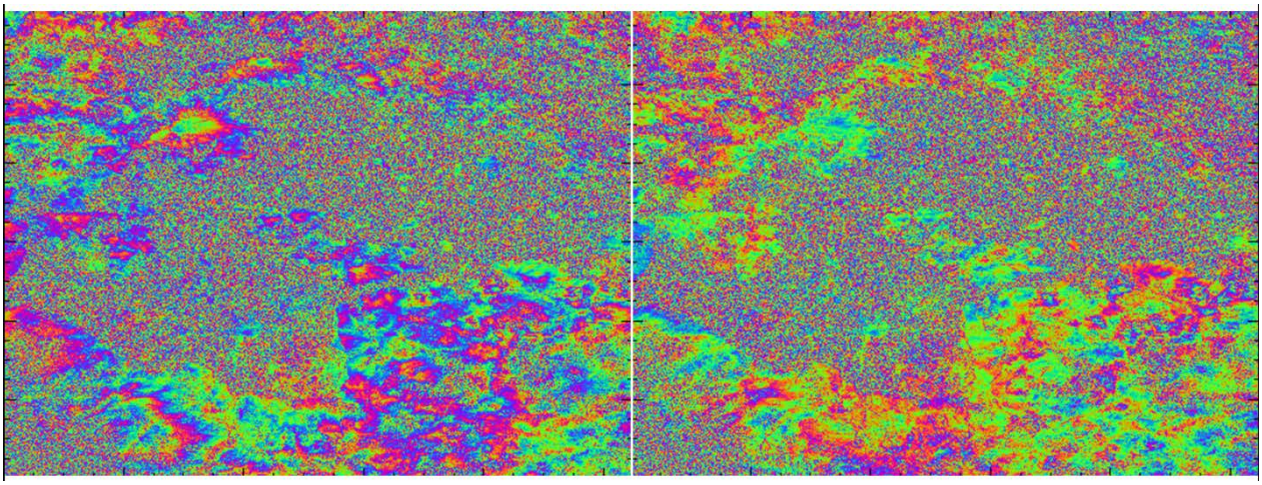

Figure 20: left: summer – winter interferogram with vertical stratification effect; right: stratification corrected interferogram using estimated atmosphere phase visualized in Figure 19 (for the interferogram with slave 11155).

A characteristic of this method is that the model is limited to be linear only. A quadratic model is not reliable any more as can be seen in the example data in Figure 18. Another characteristic is that the correct estimation is not guaranteed for each scene. Essentially, the estimation precision depends on the interferogram coherence in the mountainous areas. Three examples (two positive and one negative) are shown in Figure 21, Figure

22 and in Figure 23. In practice, coherence thresholds above 0.7 have been found sufficient for the estimation. Another typical drawback of this method is the small number of support points for high DEM values in the regression. This effect is clearly visible in Figure 22. Usable points above 700 m height are not available in this example. This makes the method sensitive to outliers which cannot always be compensated by the robust L1-norm estimation. However, the 700 m height difference is sufficient even for the estimation of the small stratification effect of winter – winter interferograms as demonstrated in Figure 22. Finally, the demonstrated measurements confirm, that the stratification effect is large for the winter – summer interferograms (-0.75 rad per 100 m in Figure 18, -0.93 rad per 100 m in Figure 21) and small for winter – winter interferograms (-0.31 rad per 100 m in Figure 22).

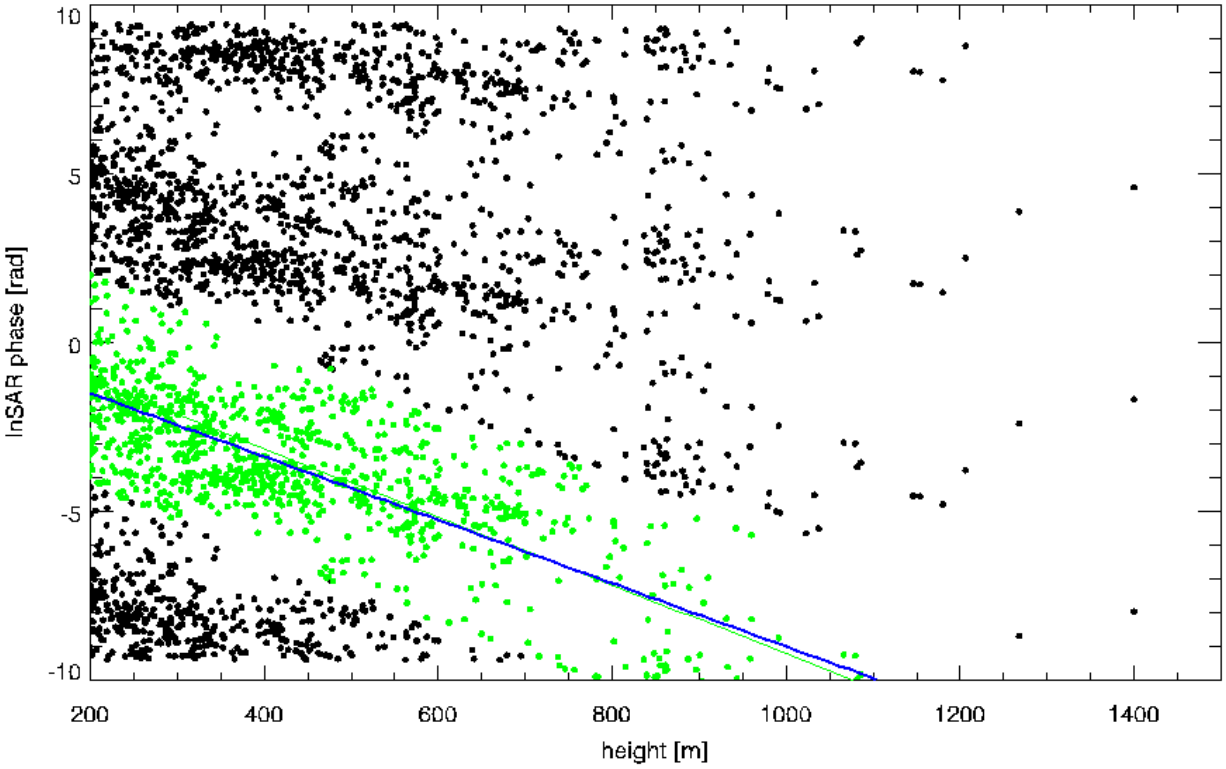

Figure 21: stratification estimation for an interferogram with the slave (with orbit 12658) taken on 21. September 1997. The coherence threshold for 1000 points is 0.72. The dependency is -0.94 rad per 100 m.

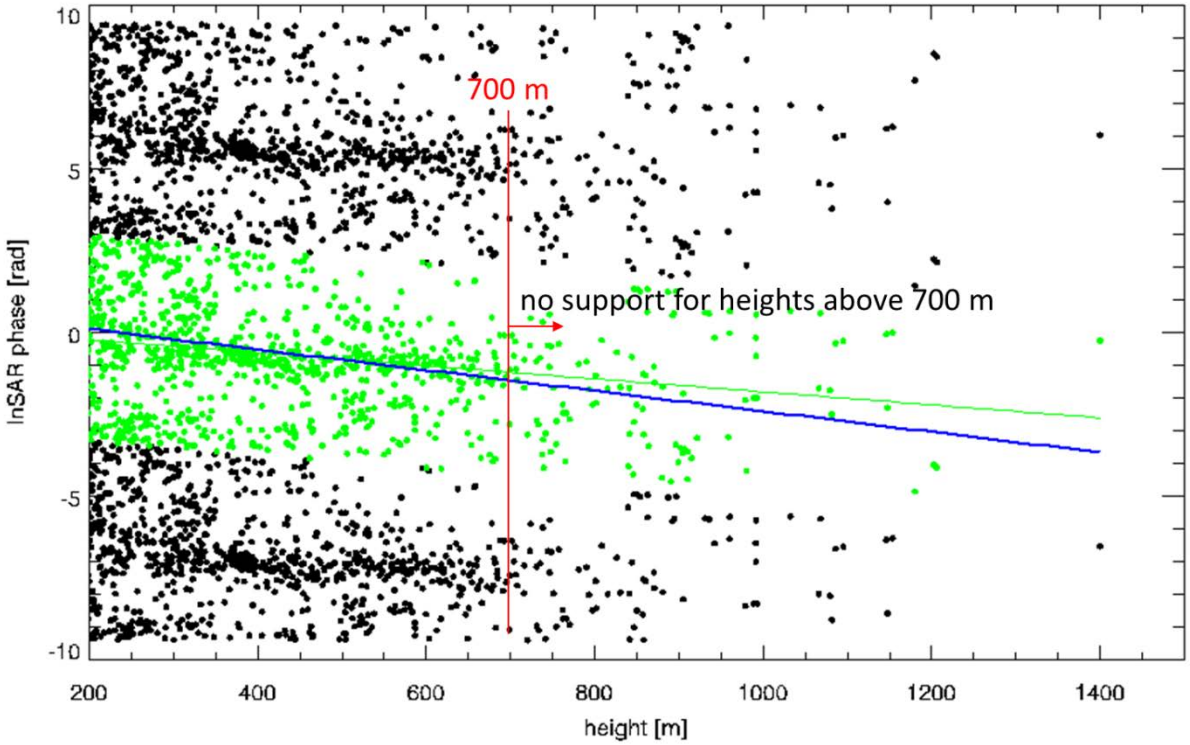

Figure 22: stratification estimation for an interferogram with the slave (with orbit 24682) taken on 9. January 2000. The coherence threshold for 1000 points is 0.67. The dependency is -0.3 rad per 100 m.

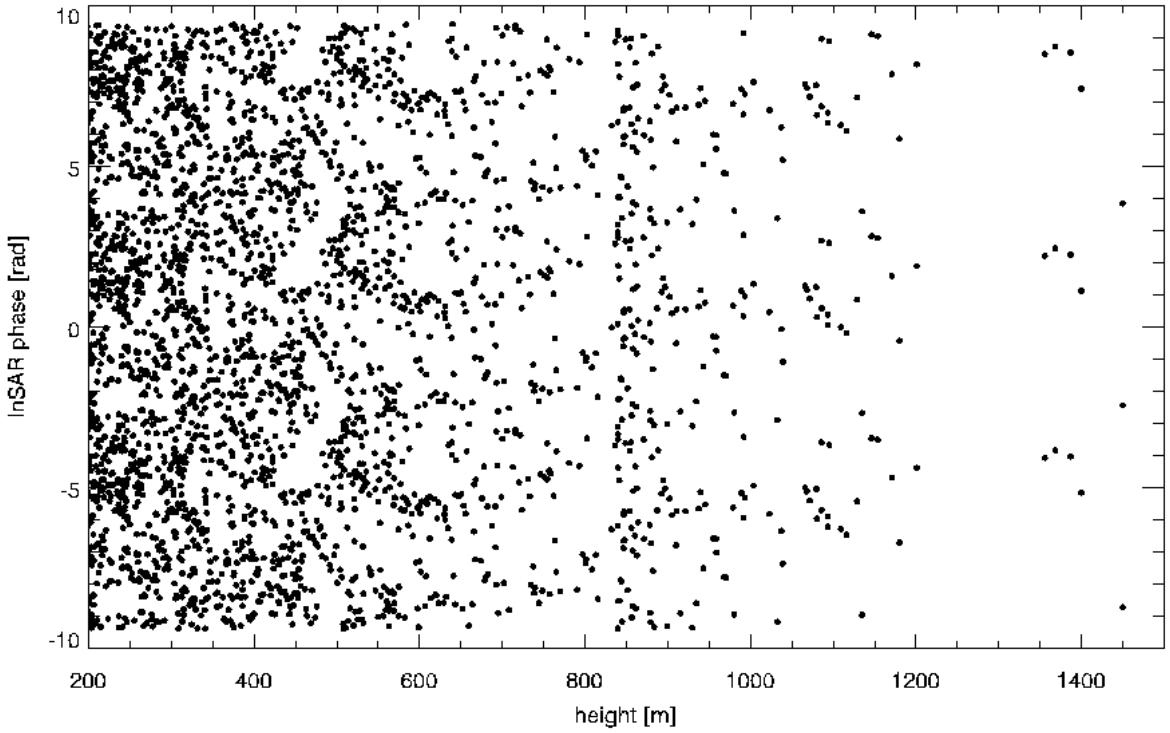

Figure 23: regression plot for an interferogram with the slave (with orbit 17668) taken on 6. September 1998. The coherence threshold for 1000 points is 0.56. These data are not usable for the estimation.

6.2 ESTIMATION FROM A SLICE OF DATA

In principle, this method is similar to the estimation of the stratification effect from the full scene which is described in the previous section 6.1. However, the location and the height of the interferogram points are not selected randomly based on a coherence threshold. Now, a slice of data is fitted directly. Such a slice could be selected manually. Practically, it should include a significant variation of topography. An example for an usable slice is shown in Figure 24 and is highlighted by the white circle. Of course, the DEM and the phase values along this cut are extracted. The next estimation step is a robust regression of the DEM height with the respective absolute phase values. It is shown in Figure 25. For this reason, the relative interferogram values are unwrapped using an approximate line fit (green line in the figure). The relative interferogram phase values are compensated by an integer multiple of $2 \cdot \pi$ to be in the range of $[-\pi, +\pi[$ around the green line. As a result, the green absolute phase values shown in Figure 25 are available. These points are the input for a L1-norm based robust line fit. In this example, the atmosphere stratification phase φ_{tropo} [rad] depending on the height h [m] is fitted by:

$$\varphi_{tropo} = 4.28007 - h \cdot 0.00515045 \quad (16)$$

Finally, the PSI estimation needs to consider the height difference Δh [m] between two point scatterers only:

$$\Delta\varphi_{tropo} = -0.00515045 \cdot \Delta h \quad (17)$$

Practically, the estimation is based on points between 300 m and 1000 m in this test case. However, the simple linear model allows to extrapolate and to compensate scatterers below and above this height range.

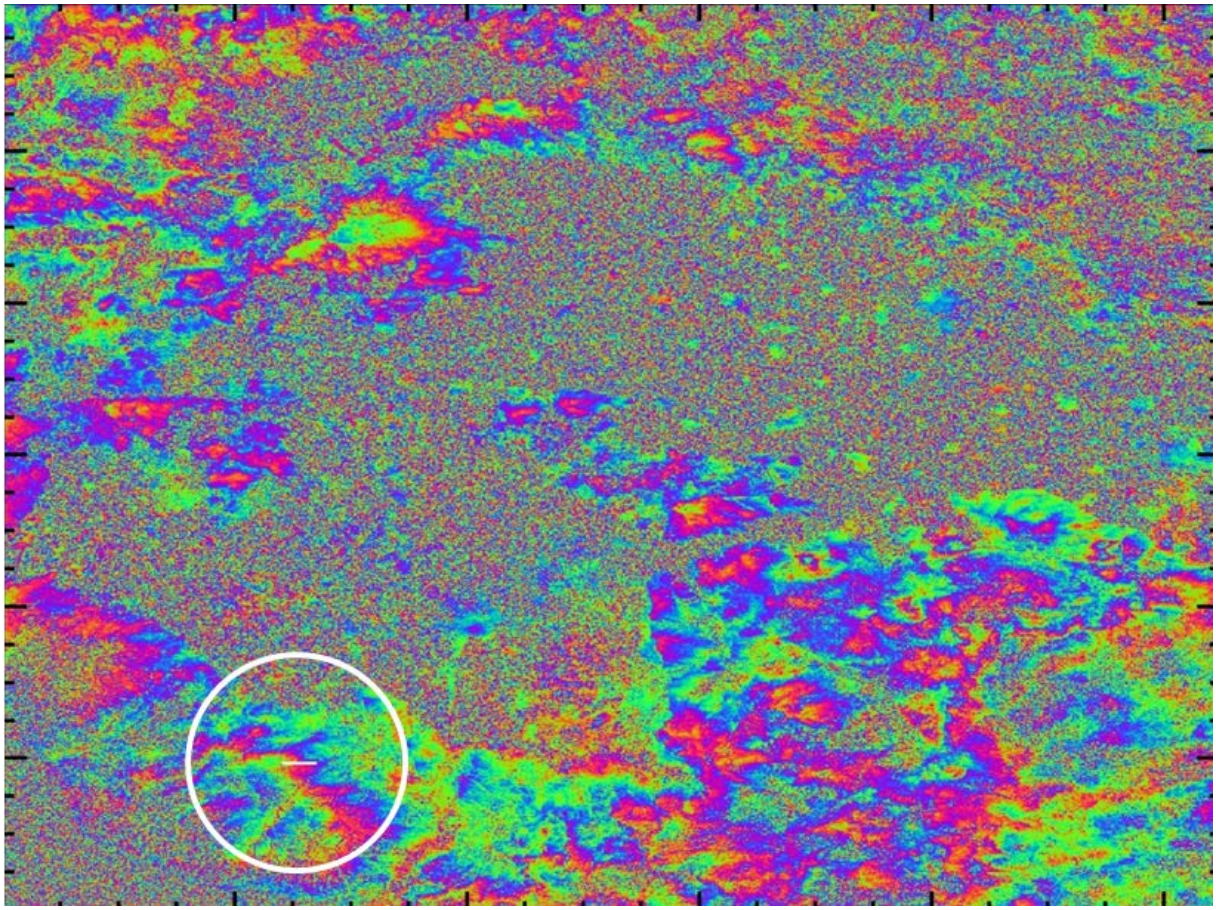

Figure 24: summer – winter interferogram (with slave 11155) with vertical stratification effect with a visualisation of the slice for the data extraction in this example

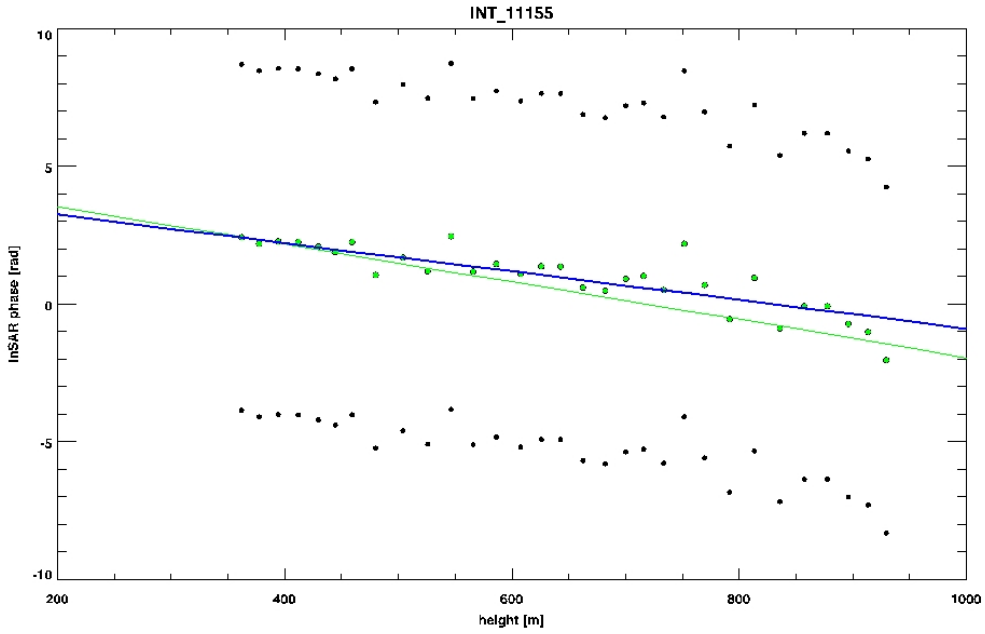

Figure 25: vertical stratification estimated from 31 points taken from the slice in Figure 24. The dependency is -0.51 rad per 100 m. Practically, many slices should be combined in the regression.

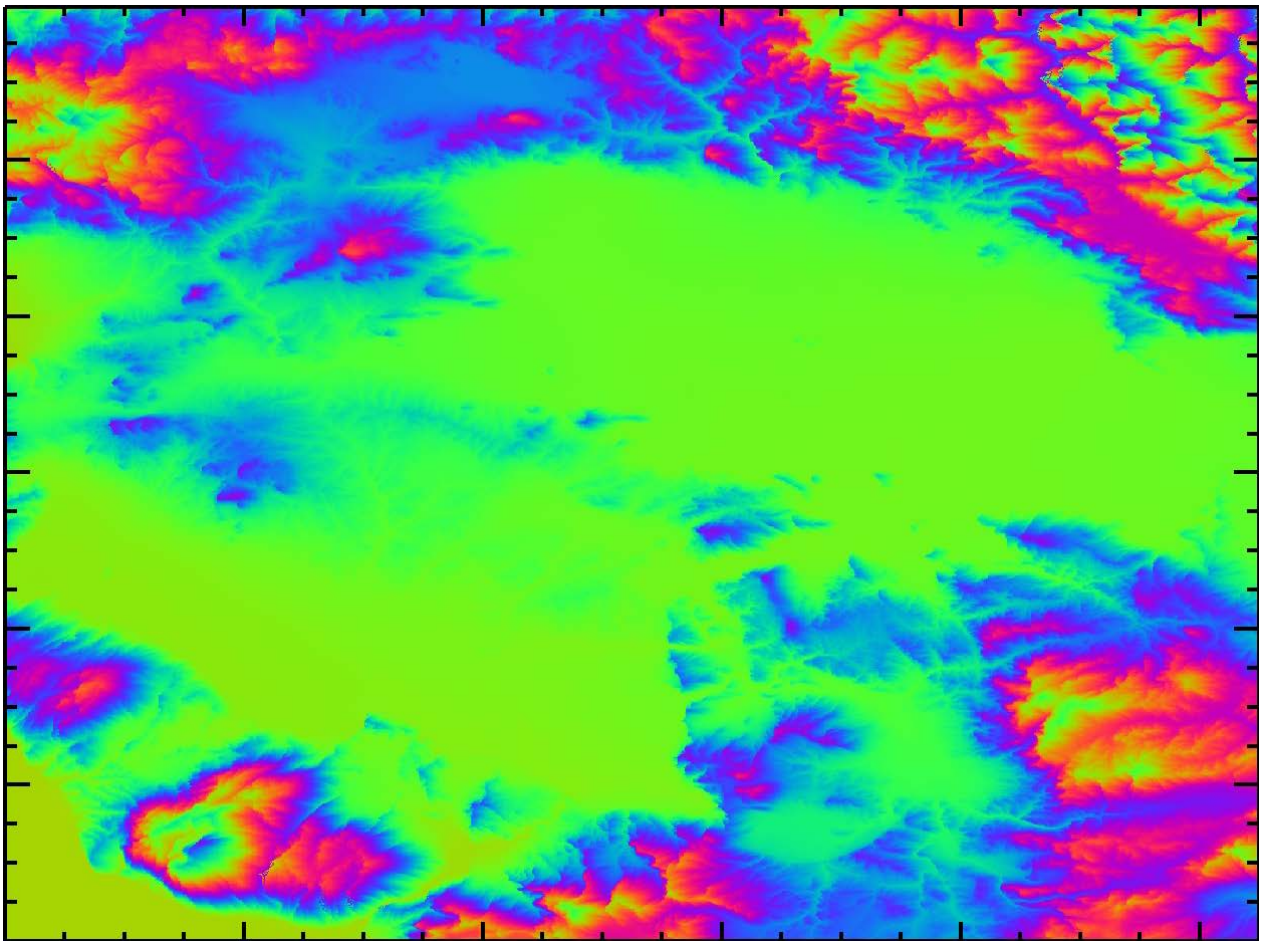

Figure 26: phase of the modelled atmosphere effect based on the estimation from Equation (17) for the interferogram with slave 11155.

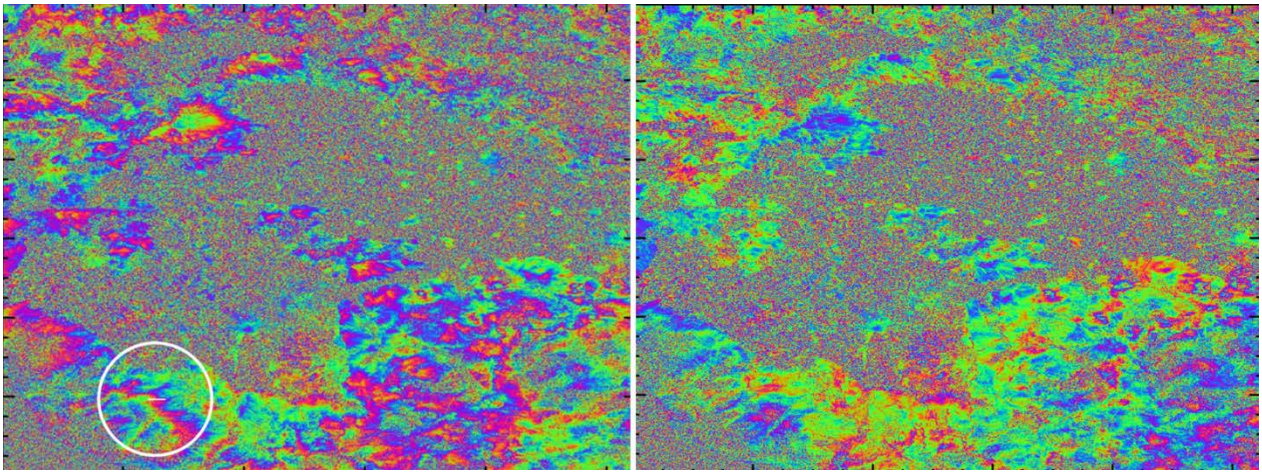

Figure 27: left: summer – winter interferogram (with slave 11155) with vertical stratification effect; right: stratification corrected interferogram using estimated atmosphere phase visualized in Figure 26.

6.3 DISCUSSION

The two methods described in sections 6.1 and 6.2 require coherent long time interferograms. However, especially in mountainous areas, this precondition is hardly to achieve in typical test sites. Advantageously, coherent interferograms distributed over one year only are in principle sufficient to apply finally both methods with success. In practice, the stratification is cyclic with the period of one year. I.e. the estimation over the year can be modelled and consequently fitted by a cosine function. This data fit requires only three parameters. As a consequence, only six to ten coherent interferograms are needed. Finally, this cosine model-fit allows the interpolation and especially the long-time extrapolation for long time interferograms in the PSI processing. Of course, the cosine fit over a time span of one to two years reduces the precision. Practically, the wet component which varies quickly over time is smoothed out. As a consequence, single scenes with untypical weather conditions are not optimally compensated. Another important error source in this compensation is the restriction to a simple linear model. In reality, the relation between height and atmospheric effect is non-linear as will be demonstrated in section 8.3. One more problem results in a limited applicability of both direct estimation methods. In case the mountain or parts of it are moving which is typical for volcanoes, the direct estimation is systematically biased. Respectively, the desired deformation signal will be systematically biased by the atmosphere compensation.

In the following section, the results of the two direct InSAR-data based estimation methods are compared to provide an impression on the reliability. For this reason, the differential interferograms of each test case and the respective stratification effect corrected differential interferograms are visualized in Figure 28 to Figure 31. Additionally, Table 1 provides the measurements in units of rad per 100 Meter (i.e. [rad/100m]). The results demonstrate (e.g. by the removed residual phase fringes in the compensated interferograms) that both methods can mitigate the stratification effect and cope with the wet and the dry component. However in practice, the estimation precision depends on the coherence of the input interferograms for both algorithms. On the one hand, it seems that the slice method is slightly more robust caused by the restriction to carefully selected support points. On the other, the full scene method provides a better global solution.

Table 1: estimated values for the stratification correction

slave orbit	slave acqu. time	combination m/s	full scene method	slice method
11155	23.Feb.1997	winter/summer	-0.75 [rad/100m]	-0.51 [rad/100m]
12658	21.Sep.1997	winter/summer	-0.93 [rad/100m]	-0.37 [rad/100m]
24682	09.Jan.2000	winter/winter	-0.31 [rad/100m]	+0.34 [rad/100m]
17668	06.Sep.1998	winter/summer	not estimable	-0.72 [rad/100m]

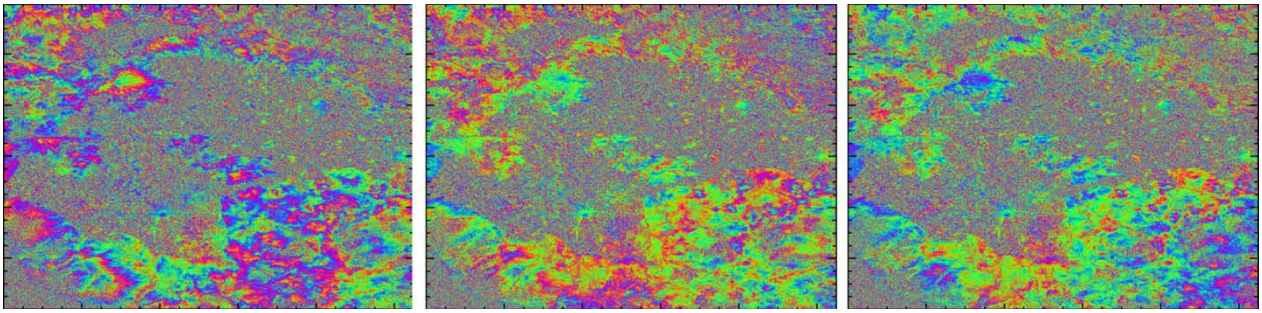

Figure 28: test case interferogram with slave interferogram with slave 11155; left: differential interferogram; middle: stratification compensated interferogram using the full scene method; right: stratification compensated interferogram using the slice method.

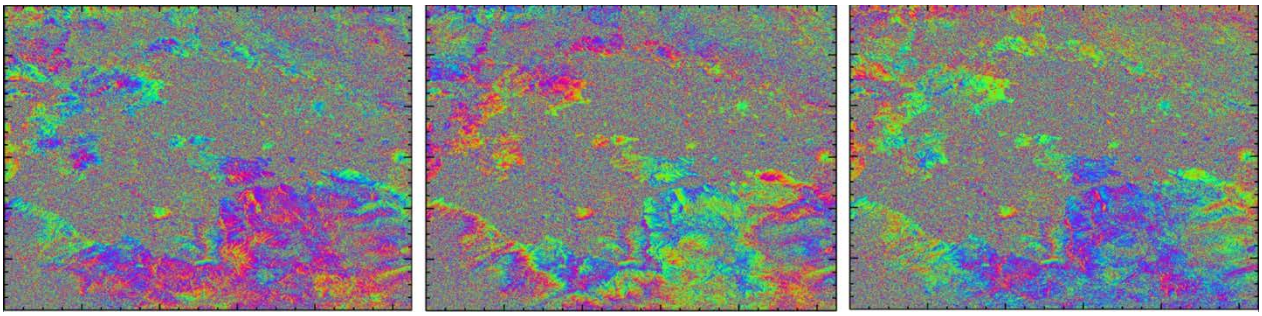

Figure 29: test case interferogram with slave 12658; left: differential interferogram; middle: stratification compensated interferogram using the full scene method; right: stratification compensated interferogram using the slice method.

Figure 30: test case interferogram with slave 17668; left: differential interferogram; middle: full scene method cannot estimate the stratification; right: stratification compensated interferogram using the slice method.

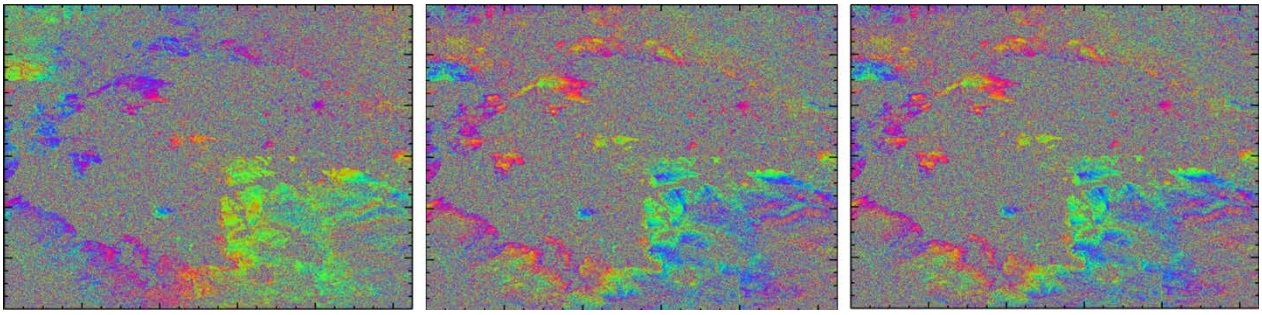

Figure 31: test case interferogram with slave 24682; left: differential interferogram; middle: stratification compensated interferogram using the full scene method; right: stratification compensated interferogram using the slice method.

7 STRATIFICATION ESTIMATION FROM GPS ZENITH DELAY DATA

The tropospheric delay is determined from ground based GNSS (global navigation satellite system) measurements [7]. Utilized are measurements from the EUREF Permanent Network (EPN) which is a science-driven network of continuously operating GNSS reference stations covering Europe. Operational EPN products are

- the ITRS/ETRS89 station positions and velocities and
- the tropospheric zenith path delays.

The tropospheric zenith path delays are made available in the SINEX_TRO format [8] at the data centre product download locations [9]. An example is visualized in Figure 32. This figure is manually adapted in order to show the atmosphere effects. In red colour, the seasonal variation of the dry component is visualized. It is in the order of 8 cm between summer and winter time. On top of this half yearly variation, an hourly variation caused by the wet component is added. It is visualized by the green band and its variation is in the order of ten centimetres.

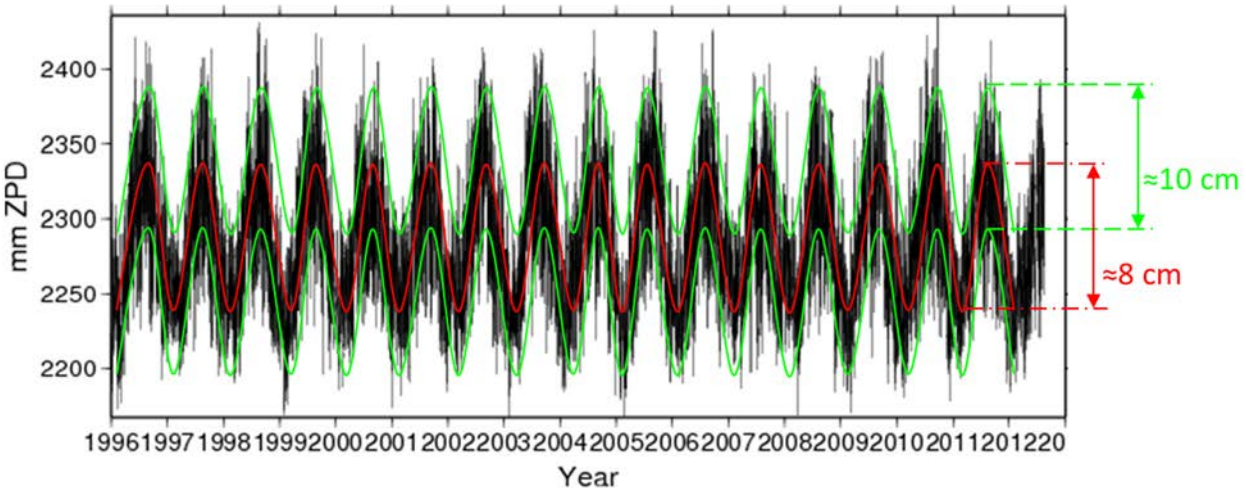

Figure 32: data recorded at the ASI (Agenzia Spaziale Italiana) Matera station

All dominant InSAR related effects (i.e. the dry and the wet component) are included in this GPS product. This fact is demonstrated in Figure 33. It shows the monthly mean of the zenith path delay at the ASI Matera station. The light green dotted line corresponds to the total mean dry effect which is in the order of 2.28 m. The averaged cyclic seasonal variation caused by the dry component is visualised with a red graph which has a peak to peak difference of about 8 cm. The fast temporal fluctuations (caused by weather effects) are in summer larger compared to winter. In this example, the variation is in the order of 6 cm in summer and 5 cm in winter and indicated in light green.

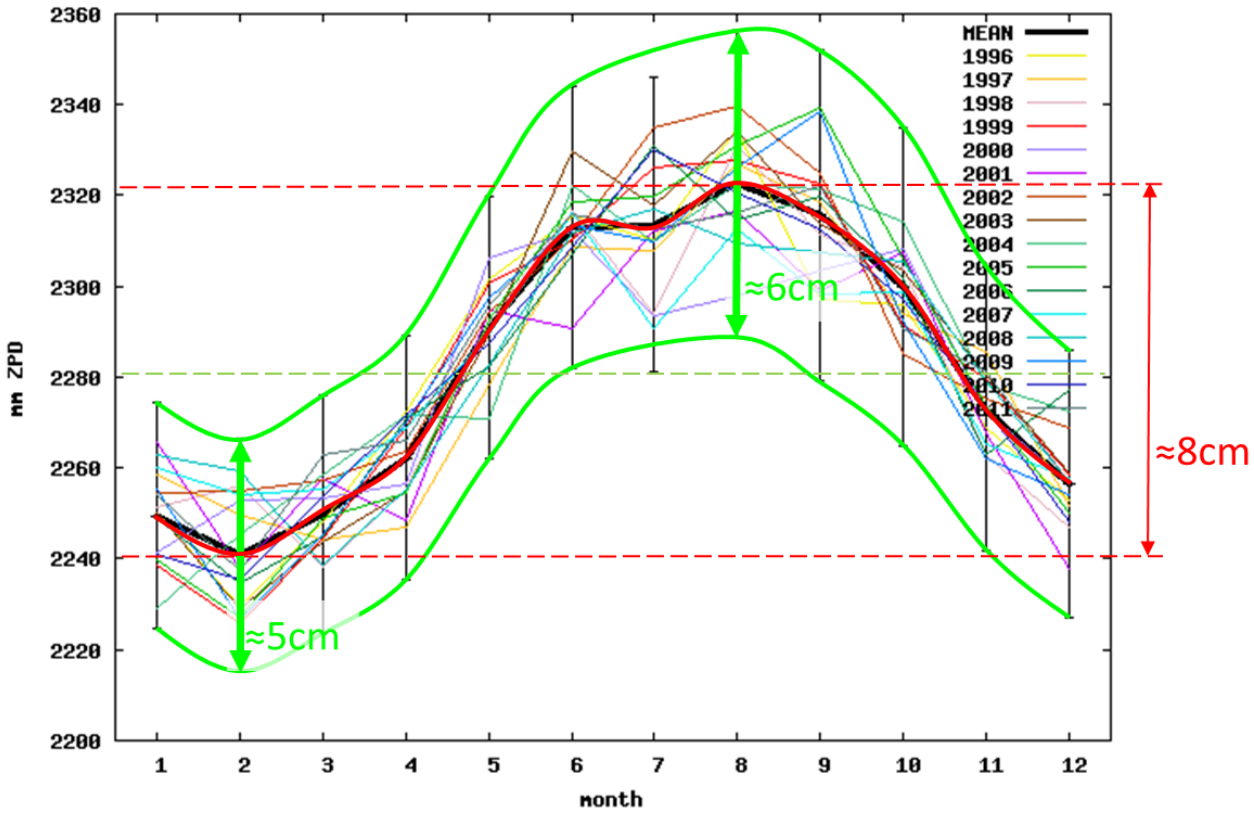

Figure 33: monthly mean of the data recorded at the ASI (Agenzia Spaziale Italiana) Matera station

The GPS based troposphere compensation method has been implemented and tested by Xiao Ying Cong in the course of her PhD as a predecessor module to compensate the atmosphere effects in PSI [10]. Now, NWP is the state of the art in the compensation of the atmosphere effect because of its wider applicability. Practically, the GPS zenith path delay method is limited by the temporal and spatial availability of the data. Figure 34 provides an overview on the EUREF permanent network stations. Basically, the density of the GPS stations in central Europe is good. However, the number of GPS stations is practically limited in case data for a particular test site are needed. As an example, Figure 35 shows the available GPS stations in Greece. The whole country is covered by only six permanent GPS stations. Actually more badly, the temporal availability shown in Table 2 makes clear that this technique is not relevant for the use with ERS data. These two facts (i.e. the spatial and temporal availability), drastically limit the applicability of the zenith path delay based method.

Table 2: temporal availability of the Greece permanent GPS stations

station town	station acronym	start date
Larissa	LARM	01. May 2012
Xanthi	DUTH	22. Feb 2009
Chania	TUC2	24 Oct 2004
Thessaloniki	AUT1	24 Apr 2005
Patras	PAT0	14 Jun 2009
Athens	NOA1	07 May 2006

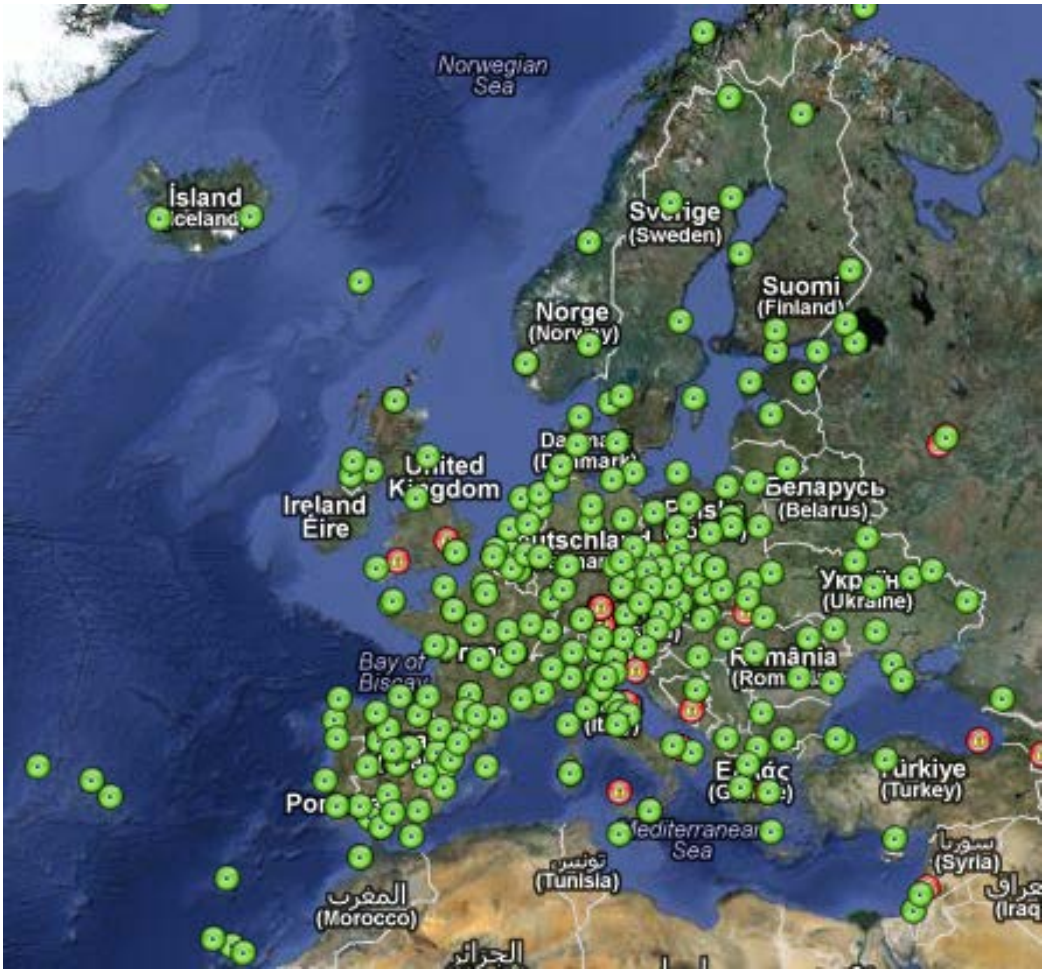

Figure 34: EUREF permanent network [11] (green dots are actual station, red dots are former stations)

Figure 35: Greece is covered by six stations in the EUREF permanent network [3] (green dots are actual station, red dots are former stations)

The zenith path delay is provided with respect to the actual GPS location (i.e. latitude, longitude), altitude and in zenith direction. Troposphere mapping functions are used in order to map zenith hydrostatic and wet delays to any other elevation angle [12]. Examples are the Niell Mapping Function (NMF), the Vienna Mapping Function (VMF1) and the Global Mapping Function (GMF) [12]. The straightest forward mapping function is the projection of the zenith path into the line of sight (LOS) with the incidence angle θ by the factor $1/\cos\theta$. For steep incidence angles (e.g. ERS with a range of 19°-27°) this simple transformation is sufficient. It neglects temporal and latitudinal (and longitudinal which are even more minor) dependencies of the mapping and transforms the wet and dry component equally (in contrast to the GMF).

A static model, similar to the pressure, is proposed in [10] to map the GPS zenith delay measurement Δ_{GPS} at the altitude h_{GPS} into the zenith delay at the altitude of the scatterer h_{PS}. Together with the LOS mapping the final transformation is

$$\Delta_{\mathrm{PS}} = \frac{\Delta_{GPS}}{\cos(\vartheta)} \cdot e^{-\left(\frac{h_{PS}-h_{GPS}}{h_0}\right)} \qquad (18)$$

The parameter h_0 corresponds to the thickness of the relevant troposphere layer. It can be assumed to be 6000 m making it consistent with a standard TerraSAR-X product calibration [13].

The applicability of this method has been practically demonstrated with TerraSAR-X data [10]. In two test cases, the troposphere effect was estimated from GPS. The first test case included two corner reflectors (CRs) on the Azores island São Miguel. The other experiment used a 3-meter CR in Oberpfaffenhofen (Germany). For the Azores the reference GPS station has a distance of 18 km to the CRs. The experiment can be described as follows. The radar measures the LOS distance (r_{LOS}) which is affected by ionosphere delay (d_{ID}), troposphere delay (d_{TD}) and the earth motion (d_{EM}) e.g. caused by solid earth tides:

$$\mathrm{r_{SAR}} = r_{LOS} + d_{ID} + d_{TD} + d_{EM} \qquad (19)$$

In the course of the experiment, the LOS distance r_{LOS}, the ionosphere delay d_{ID} and the earth motion d_{EM} was compensated. The residual distance corresponds to the troposphere delay (d_{TD}) and was correlated with the GPS based troposphere delay measurements. The estimated troposphere delays for several observations are reported in table II in [10]. It is included in Figure 36 to make the document self-contained. In the same publication, the correlation between the estimated troposphere delay and the measured residual atmosphere delay proves the general applicability of this method. Figure 37 provides a copy of the correlation plot from this paper.

Date	SAR range CR-1 [m]	SAR range CR-2 [m]	PDEL zenith delay [mm]	TD CR-1 [m]	TD CR-2 [m]	EM [m]	ID [m]	Residual CR-1 [m]	Residual CR-2 [m]
08.04.2009	2.050	2.018	2.429	2.905	2.811	0.046	0.036	-0.937	-0.875
19.04.2009	2.037	2.018	2.439	2.917	2.823	0.010	0.035	-0.926	-0.851
30.04.2009	2.116	2.128	2.470	2.954	2.860	0.067	0.041	-0.946	-0.839
11.05.2009	2.049	2.014	2.433	2.910	2.816	0.079	0.049	-0.988	-0.930
22.05.2009	1.937	1.991	2.398	2.868	2.776	-0.034	0.056	-0.953	-0.807
02.06.2009	1.945	2.013	2.425	2.901	2.807	-0.077	0.040	-0.918	-0.757
24.06.2009	2.149	2.083	2.442	2.921	2.827	0.111	0.052	-0.935	-0.907
05.07.2009	2.030	1.903	2.430	2.906	2.813	-0.008	0.037	-0.905	-0.939
16.07.2009	1.934	1.885	2.424	2.899	2.806	-0.110	0.047	-0.902	-0.857
27.07.2009	1.994	1.868	2.420	2.895	2.802	-0.027	0.036	-0.909	-0.943
07.08.2009	2.269	2.169	2.547	3.046	2.948	0.097	0.036	-0.911	-0.913
stdev	**0.101**	**0.096**	**0.039**	**0.047**	**0.045**	**0.073**	**0.007**	**0.026**	**0.059**
mean	**2.046**	**2.008**	**2.442**	**2.920**	**2.826**	**0.014**	**0.042**	**-0.930**	**-0.874**

Figure 36: absolute location residuals of the São Miguel (Azores) corner reflectors [10]. Annotated are the radar measured delays, the troposphere zenith and slant range delays at the GPS site PDEL, the earth motion, the ionosphere and the residuals.

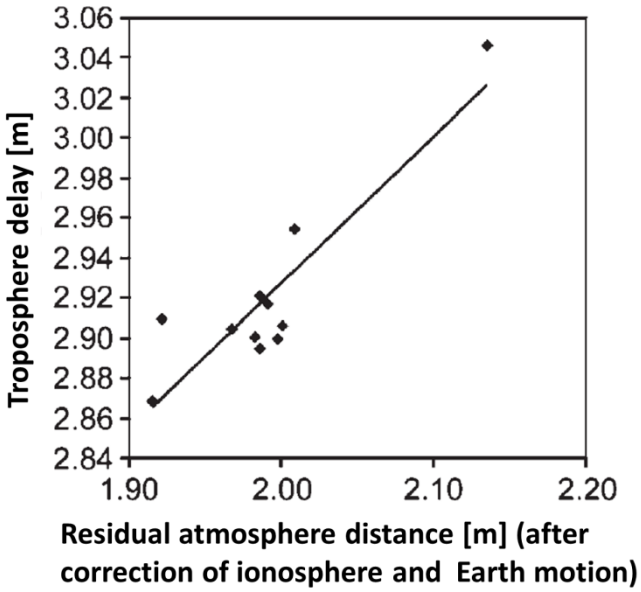

Figure 37: prove of the applicability of the GPS method by correlation between the GPS estimated troposphere and the measured distance residuals. This plot is taken from [10] (the plot labels are adapted).

8 STRATIFICATION ESTIMATION FROM NWP

In this assessment the Weather Research and Forecasting model (WRF) [14] is used to predict the atmosphere refractivity relevant parameters at the time of acquisition. Starting point are global atmosphere data which are given with a coarse spatial and temporal sampling. The WRF processing system solves systems of differential equations in space and time which describe the physical processes in the atmosphere. Such processes are exemplarily heating by sun illumination, evaporation, snowfall, rain and the transport of humidity by wind. The solutions are the atmosphere state at a finer spatial and temporal resolution [15]. This data flow principle is visualized in Figure 38.

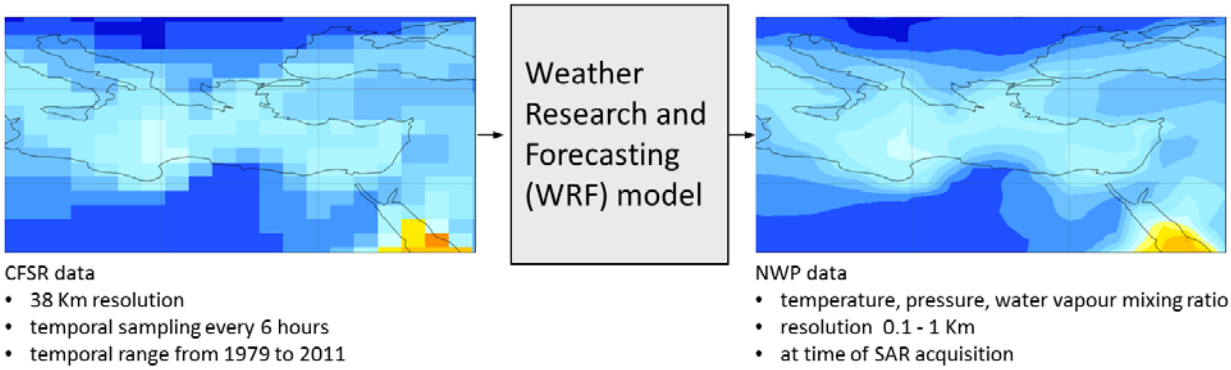

Figure 38: The WRF system models physical processes in the atmosphere to hindcast the atmosphere state with a finer temporal and spatial resolution with respect to the input data.

The WRF has been developed by the National Center for Atmospheric Research (NCAR) and its partners. And the input dataset is based on the original data from the NCEP CFSRR project. Initially, it was prepared and processed for driving regional climate models. The CFSR data for driving regional model simulations are provided by Dr. Lifeng Luo at Michigan State University [16].

8.1 THEORETICAL BASIS

The troposphere induced phase screen in a single radar acquisition is a result of wave propagation effects along the line of sight (LOS). Neglecting the frequency dependence of the refractivity $N(\vec{r})$, it can be parameterized by the Smith-Weintraub equation [6]:

$$N(\vec{r}) = k_1 \cdot \frac{P_d(\vec{r})}{T(\vec{r})} + k_4 \cdot \frac{P_c(\vec{r})}{T(\vec{r})} + k_2 \cdot \frac{e_w(\vec{r})}{T(\vec{r})} + k_3 \cdot \frac{e_w(\vec{r})}{T^2(\vec{r})} \quad (20)$$

In this equation, the dry air components $N_{dry}(\vec{r})$ are described by the partial pressures of dry air (i.e. nitrogen and oxygen but without carbon-dioxide) P_d and of carbon-dioxide P_c. In contrast, the wet component $N_{wet}(\vec{r})$ is described by the water vapour partial pressure e_w.

All refractivity components depend on the actual absolute temperature T. The approximation of Eq.(20) is generally accepted. However, the scaling constants k_1, k_2, k_3 and k_4 are often discussed because of their limited experimental accuracy [17], [18]. The parameter $k_4 = 5/3$ is typically ignored or included into the value k_1. Within this work, the following coefficients are used:

$k_1 = 77.6890$ [K/hPa], $k_2 = 71.2952$ [K/hPa] and $k_3 = 375463$ [K²/hPa].

The WRF processor provides three dimensional fields of total pressure $P_{tot} = (P + PB)/100$ in [hPa], the temperature $T_K = (T + 300)$ in [°K] and the water vapour mixing ratio $Q_{Kg/Kg} =$ QVAPOR in [Kg/Kg]. These parameters are converted into water vapour partial pressure e_w and partial pressures of dry air P_d of Eq.(20) by

$$e_w = \frac{Q_{Kg/Kg} \cdot P_{tot}}{0.622 + Q_{Kg/Kg}} \qquad (21)$$

and

$$P_d = P_{tot} - e_w . \qquad (22)$$

Consequently, Eq.(20) transforms into

$$\begin{aligned} N &= f(P_{tot}, T_K, Q_{Kg/Kg}) \\ &= k_1 \cdot \frac{0.622 \cdot P_{tot}}{(0.622 + Q_{Kg/Kg}) \cdot T_K} + k_2 \cdot \frac{P_{tot} \cdot Q_{Kg/Kg}}{(0.622 + Q_{Kg/Kg}) \cdot T_K} + k_3 \cdot \frac{0.622 \cdot P_{tot} \cdot Q_{Kg/Kg}}{(0.622 + Q_{Kg/Kg}) \cdot T_K^2} \end{aligned} \qquad (23)$$

and is accordingly used in the processor and the following error propagation assessment. The equation above is useful because it separates the dry and the wet component. However, it can be further simplified into

$$\begin{aligned} N &= f(P_{tot}, T_K, Q_{Kg/Kg}) \\ &= \frac{P_{tot} \cdot (k_3 \cdot Q_{Kg/Kg} + 0.622 \cdot k_1 \cdot T_K + k_2 \cdot Q_{Kg/Kg} \cdot T_K)}{(0.622 + Q_{Kg/Kg}) \cdot T_K^2} \end{aligned} \qquad (24)$$

Together with this fundamental estimation equation, the error propagation basis can be introduced. With the assumption of uncorrelated input parameters i.e. the total pressure P_{tot}, the temperature T_K and the water vapour mixing ratio $Q_{Kg/Kg}$, the propagation of uncertainty is described by the straight forward equation

$$\begin{aligned} \sigma_N^2 = & \left(\frac{\delta f(P_{tot}, T_K, Q_{Kg/Kg})}{\delta P_{tot}} \right)^2 \cdot \sigma_{P_{tot}}^2 + \\ & \left(\frac{\delta f(P_{tot}, T_K, Q_{Kg/Kg})}{\delta T_K} \right)^2 \cdot \sigma_{T_K}^2 + \\ & \left(\frac{\delta f(P_{tot}, T_K, Q_{Kg/Kg})}{\delta Q_{Kg/Kg}} \right)^2 \cdot \sigma_{Q_{Kg/Kg}}^2 \end{aligned} \qquad (25)$$

The factors which characterise the amplification of the input variances evaluate to

$$\left(\frac{\delta f\left(P_{tot},T_K,Q_{Kg/Kg}\right)}{\delta P_{tot}}\right)^2 = \frac{k_3\cdot Q_{Kg/Kg}+0.622\cdot k_1\cdot T_K+k_2\cdot Q_{Kg/Kg}\cdot T_K}{\left(0.622+Q_{Kg/Kg}\right)^2\cdot T_K^4} \quad (26)$$

and to

$$\left(\frac{\delta f\left(P_{tot},T_K,Q_{Kg/Kg}\right)}{\delta T_K}\right)^2 = \frac{4\cdot P_{tot}^2\cdot\left(k_3\cdot Q_{Kg/Kg}+0.311\cdot k_1\cdot T_K+0.5\cdot k_2\cdot Q_{Kg/Kg}\cdot T_K\right)^2}{\left(0.622+Q_{Kg/Kg}\right)^2\cdot T_K^6} \quad (27)$$

and to

$$\left(\frac{\delta f\left(P_{tot},T_K,Q_{Kg/Kg}\right)}{\delta Q_{Kg/Kg}}\right)^2 = \frac{0.386884\cdot P_{tot}^2\cdot\left(k_3-k_1\cdot T_K+k_2\cdot T_K\right)^2}{\left(0.622+Q_{Kg/Kg}\right)^4\cdot T_K^4} \quad (28)$$

Practically, the error propagation described so far provides the variance of the estimated refractivity at the location of the WRF output grid visualized in Figure 39. However, the integration along the wave propagation path requires interpolation resulting in statistically dependent intermediate values and affecting the error propagation.

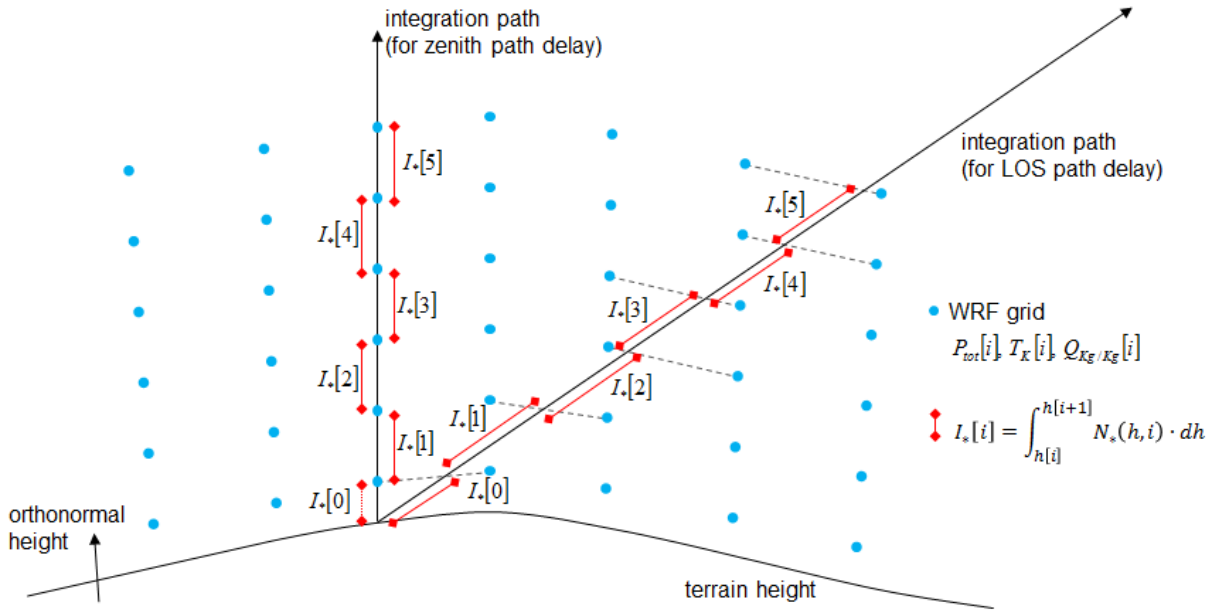

Figure 39: refractivity estimations are located on the WRF output grid

Essentially, four different algorithms can be implemented which result in different computational effort and error propagation.

alg. 1 Zenith path delay with physics parameter interpolation

a) Pure vertical sampling of WRF output i.e. of temperature, pressure and water vapour mixing ratio,

b) Piecewise integration based on the given grid points along the zenith path and

c) Application of a mapping function on the zenith path delay.

alg. 2 LOS path delay with horizontal physics parameter interpolation and piecewise integration

a) Two dimensional horizontal interpolation on pressure levels of WRF output i.e. of temperature, pressure and water vapour mixing ratio along the LOS,

b) Piecewise integration based on the horizontally interpolated grid points along the LOS path.

alg. 3 LOS path delay with three dimensional physics parameter interpolation and numeric integration

a) Three dimensional interpolation of WRF output i.e. of temperature, pressure and water vapour mixing ratio along the LOS,

b) Numeric integration of the evaluated refractivity along the LOS path.

alg. 4 LOS path delay with horizontal refractivity interpolation and piecewise integration

a) Evaluation of refractivity at the WRF grid points,

b) Horizontal interpolation of these refractivity values and

c) Piecewise integration based on the horizontally interpolated grid points along the LOS path.

Practically, the first two algorithms should be implemented and are presented in detail. The third algorithm corresponds to the actual implementation and the examples presented in section 8.3 are generated with this approach. Unfortunately, this implementation has two drawbacks. Firstly, it is not able to provide the complete error propagation. Actually, it ignores the statistically dependence introduced by the linear and log-linear interpolation. And secondly, it is not of adequate performance and as a consequence not suitable for large areas. The fourth algorithm results in significant error propagation as a consequence of its simplicity. It ignores the non-linear characteristic of the refractivity along the LOS. The suitable algorithms are presented in the following two sections.

8.1.1 ALGORITHM 1: ZENITH PATH DELAY WITH PHYSICS PARAMETER INTERPOLATION

For the zenith path delay, the integration path is along the orthonormal height. This is the reason, the interpolation is straight forward: firstly, a single parameter is enough to be considered and secondly, the physics is directly related to this parameter (i.e. the height) and allows linear or log-linear interpolation. For temperature and water vapour ratio, the conventional linear interpolation

$$LinearInterpolation(h,h_1,h_2,v_1,v_2) = \frac{h\cdot v_1 - h_2\cdot v_1 - h\cdot v_2 + h_1\cdot v_2}{h_1 - h_2} \quad (29)$$

and for total pressure, the log-linear interpolation

$$LogLinearInterpolation(h,h_1,h_2,v_1,v_2) = Exp(\,LinearInterpolation(\,h,h_1,h_2,\,Log(v_1),Log(v_2)\,)\,) \quad (30)$$

between two neighboured grid-point-value-pairs (h_1,v_1) and respectively (h_2, v_2) can be implemented. As a consequence, the interpolated values depend finally only on the NWP-grid-values at index *i* and *i+1* of the actual segment with index *i*. The dry $N_{Dry}(h,i) = f(h,P_{tot}[i],P_{tot}[i+1],T_K[i],T_K[i+1],Q_{Kg/Kg}[i],Q_{Kg/Kg}[i+1])$,

the wet

$$N_{Wet}(h,i) = f(h,P_{tot}[i],P_{tot}[i+1],T_K[i],T_K[i+1],Q_{Kg/Kg}[i],Q_{Kg/Kg}[i+1])$$

and total

$$N(h,i) = f(h,P_{tot}[i],P_{tot}[i+1],T_K[i],T_K[i+1],Q_{Kg/Kg}[i],Q_{Kg/Kg}[i+1])$$

refractivity can now be evaluated directly along the vertical line segment. These values can be used in a numerical integration along the zenith path. This is the reason, these expressions are provided. However instead writing the full equations, all are decomposed into common sub-expressions supporting implementation and printing. First of all, the common sub-expressions are

$$\mathrm{A1} = T_K[i] - T_K[i+1] \quad (31)$$
$$\mathrm{A2} = h[i] - h[i+1]$$
$$\mathrm{A3} = h - h[i+1]$$
$$\mathrm{A4} = h - h[i]$$
$$\mathrm{A5} = 1.244 + Q_{\mathrm{Kg/Kg}}[i] + Q_{Kg/Kg}[i+1]$$
$$\mathrm{A6} = T_K[i] + T_K[i+1]$$
$$\mathrm{A7} = Q_{\mathrm{Kg/Kg}}[i] - Q_{\mathrm{Kg/Kg}}[i+1]$$

Using these expressions, the refractivity along each segment *i* for the dry component is

$$\mathrm{B1}=\frac{1}{0.622+\dfrac{\mathrm{A3}\cdot Q_{\mathrm{Kg/Kg}}[i]-\mathrm{A4}\cdot Q_{\mathrm{Kg/Kg}}[i+1]}{\mathrm{A2}}} \quad (32)$$

$$\mathrm{N}_{Dry}(h,i)=\frac{0.622\cdot \mathrm{A2}\cdot \mathrm{B1}\cdot k_1\cdot P_{\mathrm{tot}}[i]^{\frac{\mathrm{A3}}{\mathrm{A2}}}\cdot P_{\mathrm{tot}}[i+1]^{-\frac{\mathrm{A4}}{\mathrm{A2}}}}{\mathrm{A3}\cdot T_K[i]-\mathrm{A4}\cdot T_K[i+1]}$$

and for the wet component, the refractivity is

$$\mathrm{B2}=\frac{1}{\mathrm{A7}\cdot h+h[1+i]\cdot(-0.622-Q_{\mathrm{Kg/Kg}}[i])+h[i]\cdot(0.622+Q_{\mathrm{Kg/Kg}}[1+i])} \quad (33)$$

$$\mathrm{B3}=h[i]\cdot k_3+h[1+i]\cdot(-k_3-k_2\cdot T_K[i])+k_2\cdot(h\cdot T_K[i]-\mathrm{A4}\cdot T_K[1+i])$$

$$\mathrm{N}_{Wet}(h,i)=$$

$$\frac{\mathrm{A2}\cdot \mathrm{B2}\cdot \mathrm{B3}\cdot P_{\mathrm{tot}}[i]^{\frac{\mathrm{A3}}{\mathrm{A2}}}\cdot P_{\mathrm{tot}}[1+i]^{-\frac{\mathrm{A4}}{\mathrm{A2}}}\cdot\left(\mathrm{A3}\cdot Q_{\mathrm{Kg/Kg}}[i]-\mathrm{A4}\cdot Q_{\mathrm{Kg/Kg}}[1+i]\right)}{(\mathrm{A3}\cdot T_K[i]-\mathrm{A4}\cdot T_K[1+i])^2}$$

and the total refractivity is

$$\mathrm{B4}=\frac{1}{0.622+\dfrac{\mathrm{A3}\cdot Q_{\mathrm{Kg}}[i]-\mathrm{A4}\cdot Q_{\mathrm{Kg/Kg}}[1+i]}{\mathrm{A2}}} \quad (34)$$

$$\mathrm{B5}=\frac{1}{(\mathrm{A3}\cdot T_K[i]-\mathrm{A4}\cdot T_K[1+i])^2}$$

$$\mathrm{B6}=k_2\cdot(\mathrm{A3}\cdot Q_{\mathrm{Kg}}[i]-\mathrm{A4}\cdot Q_{\mathrm{Kg}}[1+i])\cdot(\mathrm{A3}\cdot T_K[i]-\mathrm{A4}\cdot T_K[1+i])$$

$$\mathrm{B7}=\mathrm{B6}+\mathrm{A2}\cdot k_3\left(\mathrm{A3}\cdot Q_{\frac{\mathrm{Kg}}{\mathrm{Kg}}}[i]-\mathrm{A4}\cdot Q_{\frac{\mathrm{Kg}}{\mathrm{Kg}}}[1+i]\right)+$$

$$0.622\cdot \mathrm{A2}\cdot k_1(\mathrm{A3}\cdot T_K[i]-\mathrm{A4}\cdot T_K[1+i])$$

$$\mathrm{N}(h,i)=\mathrm{B4}\cdot \mathrm{B5}\cdot \mathrm{B7}\cdot P_{\mathrm{tot}}[i]^{\frac{\mathrm{A3}}{\mathrm{A2}}}\cdot P_{\mathrm{tot}}[1+i]^{-\frac{\mathrm{A4}}{\mathrm{A2}}}$$

In the next step, the estimation of the total zenith path delay requires the integration along each interpolated section and finally the summation of all segment integrals. Unfortunately, the nonlinear equations above cannot be integrated analytically. Of course, numeric integration is one solution. However, this implementation is of poor computational performance. This is the reason, these functions are expanded into Taylor series around the center point of the respective interval. With an expansion order of one, the relative error of the dry effect refractivity is for a typical vertical profile less than 0.5 percent and with the order of two, the maximum relative error reduces to insignificant 0.02 percent An example is visualised in Figure 40. Figure 41 provides an example for the introduced relative and absolute error for the wet component using the Taylor approximation. Practically, both i.e. first and second order approximations are implemented in the currently updated troposphere effect mitigation processor and can be selected at run time depending on the actual precision requirements.

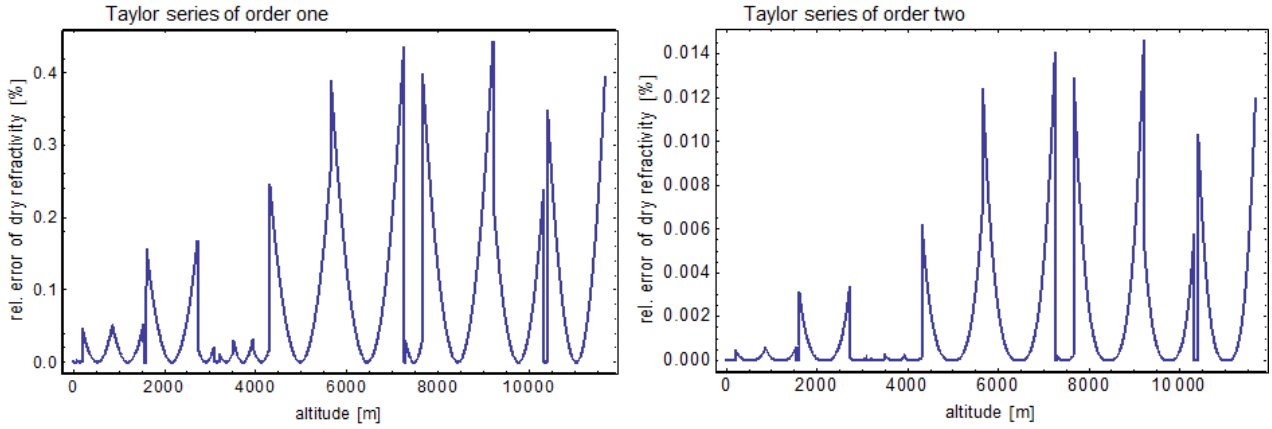

Figure 40: relative error for linear (left) and quadratic (right) Taylor series approximation of the segments dry effect refractivity

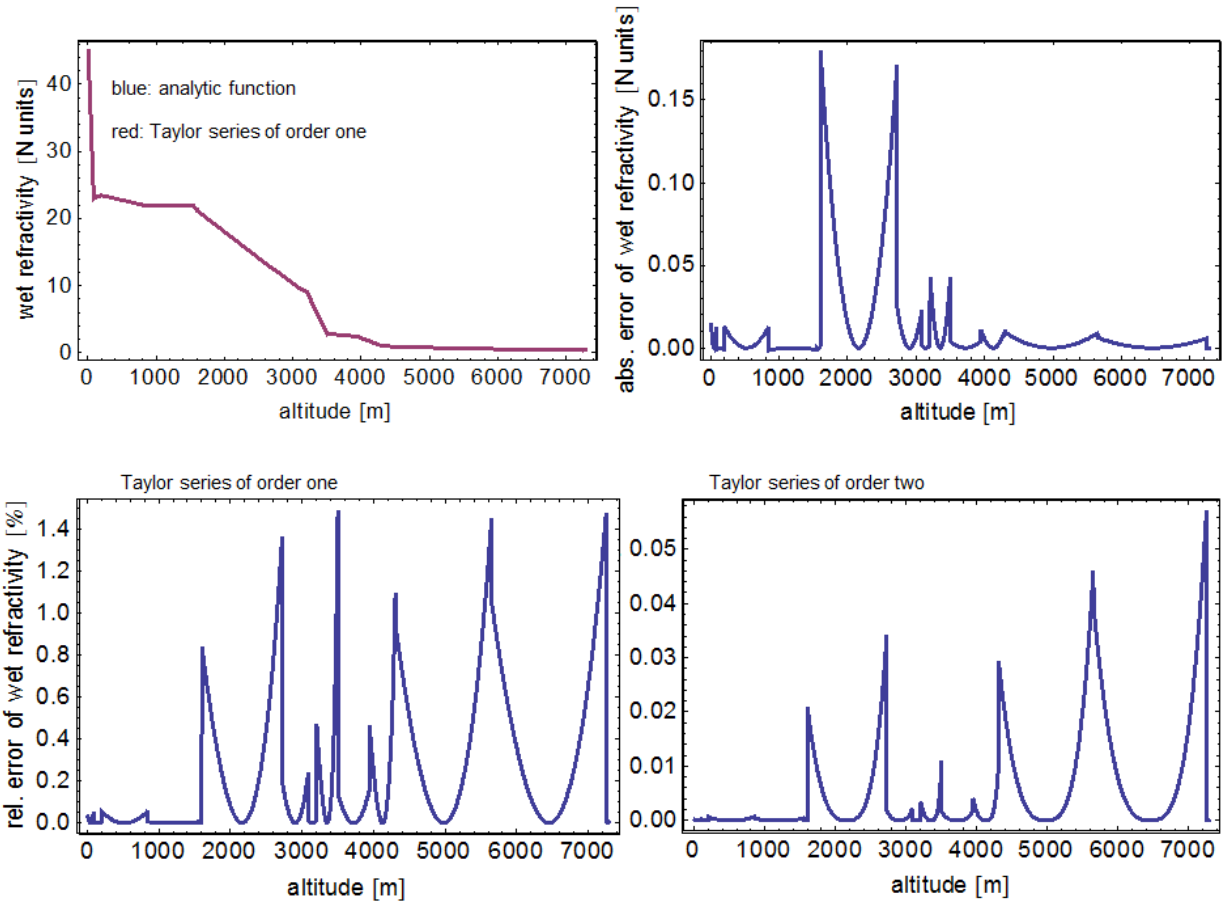

Figure 41: top left: example wet refractivity function, top right: absolute deviation between analytic function and Taylor series of order one, bottom: relative error for linear (left) and quadratic (right) Taylor series approximation of the segments wet effect refractivity

For the linear approximation, the segment integrals can now be evaluated directly (i.e. much faster compared to numerical integration) using

$$I_{Dry}[i] = \int_{h[i]}^{h[i+1]} N_{Dry}(h,i)\cdot dh = -\frac{2.488\cdot \mathrm{A2}\cdot k_1\cdot\sqrt{P_{\mathrm{tot}}[i]\cdot P_{\mathrm{tot}}[1+i]}}{\mathrm{A5}\cdot \mathrm{A6}} \qquad (35)$$

and

$$\mathrm{B8} = h[i](\mathrm{A6}\cdot k_2 + 2\cdot k_3) + h[1+i](-2\cdot k_3 - k_2\cdot T_K[i] - k_2\cdot T_K[1+i]) \qquad (36)$$

$$I_{Wet}[i] = \int_{h[i]}^{h[i+1]} N_{Wet}(h,i)\cdot dh =$$

$$-\frac{2\cdot \mathrm{A2}\cdot \mathrm{B8}\cdot\sqrt{P_{\mathrm{tot}}[i]\cdot P_{\mathrm{tot}}[1+i]}(Q_{\mathrm{Kg/Kg}}[i] + Q_{\mathrm{Kg/Kg}}[1+i])}{\mathrm{A5}\cdot \mathrm{A6}^2\cdot A2}$$

and

$$\mathrm{B9} = 1.244\cdot \mathrm{A6}\cdot k_1 + (\mathrm{A6}\cdot k_2 + 2\cdot k_3)\cdot(Q_{\mathrm{Kg/Kg}}[i] + Q_{\mathrm{Kg/Kg}}[1+i]) \qquad (37)$$

$$I_{total}[i] = \int_{h[i]}^{h[i+1]} N(h,i)\cdot dh = -\frac{2\cdot \mathrm{A2}\cdot \mathrm{B9}\cdot\sqrt{P_{\mathrm{tot}}[i]\cdot P_{\mathrm{tot}}[1+i]}}{\mathrm{A5}\cdot \mathrm{A6}^2}$$

respectively. This segment-wise operation and the respective error propagation are visualized in Figure 42 representing a building block in the total algorithm which is sketched in Figure 43. Finally, the range error components d_{Dry}, d_{Wet} and the total range error d_{total} are computed by the sum of the respective individual segment integrals.

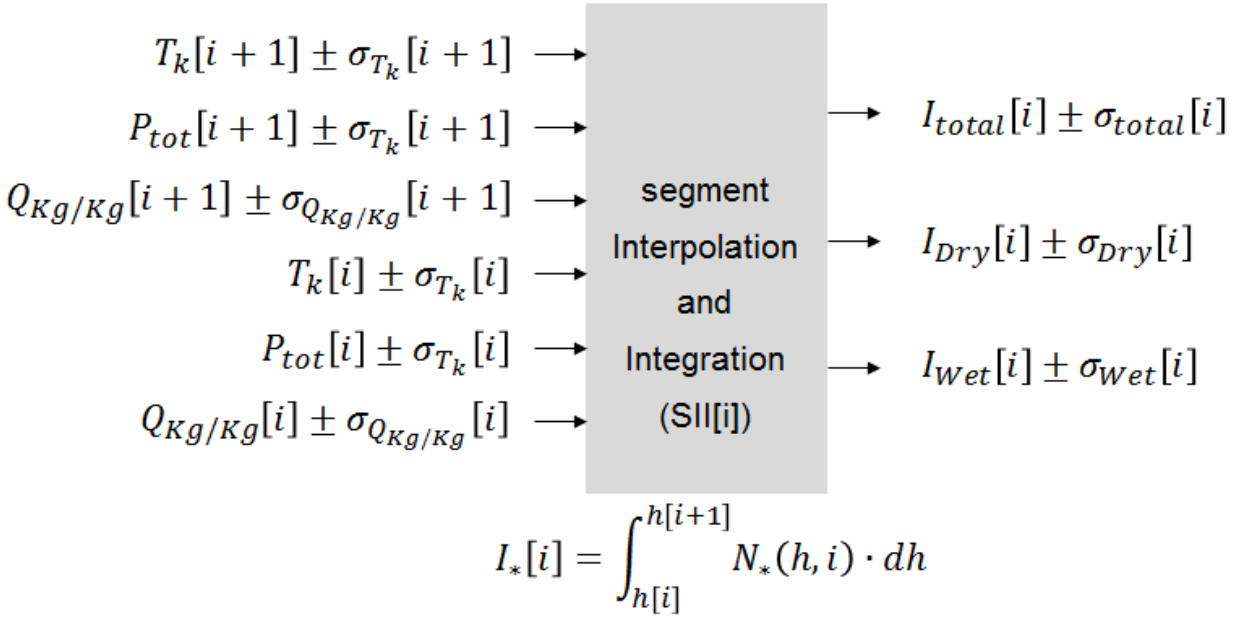

Figure 42: Error propagation into the segment integrals (equations 35 – 37)

$$d_{Dry} = I_{Dry} = \sum_{i=1}^{n} I_{Dry}[i] \quad (38)$$

$$d_{Wet} = I_{Wet} = \sum_{i=1}^{n} I_{Wet}[i]$$

$$d_{total} = I_{total} = \sum_{i=1}^{n} I_{total}[i]$$

In order to characterize and quantify the error propagation of these operations, we need the covariance matrix of the input data C_{TPQ} (i.e. temperature, total pressure, water vapour mixing ratio) and of the intermediate data C_{SII} (i.e. the segment integrals) as well as the Jacobian matrices of the respective operations F_{SII} and F_{Sum}. Finally, the error propagation is approximated for the segment interpolation and integration operation by

$$C_{SII} = F_{SII} C_{TPQ} (F_{SII})^T \quad (39)$$

and for the subsequent sum of segment integrals operation step by

$$C_I = F_{Sum} C_{SII} (F_{Sum})^T \quad (40)$$

Some comments to support an independent implementation follow: It is clear that the Jacobian matrices F_{SII} need to be constructed individually for the respective wet and dry components as well as for the total effect. Furthermore, the final covariance matrix C_I of the overall integral consists of a single value providing the variance of the respective total path error. The current implementation of the troposphere effect mitigation processor converts the individual segment integrals into units of Millimetre. For this reason, $I_{Dry}[i]$, $I_{Wet}[i]$ and $I_{total}[i]$ (i.e. eq. 35, 36 and 37) are multiplied with the factor 0.001. As a result, the variance is estimated in mm^2.

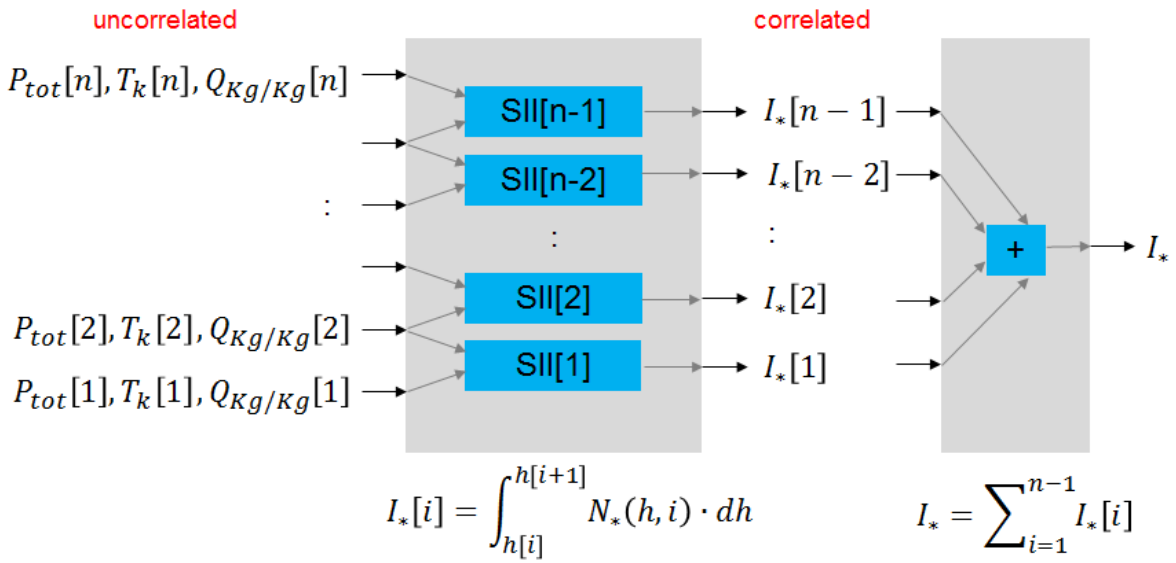

Figure 43: Total error propagation: the NWP-grid-input variables are considered uncorrelated. However, the segment integrals are correlated because of sharing the neighbour's input data.

Now, the covariance matrix for the input data and the Jacobian matrix for the segment wise interpolation and integration can be generated. In the following, the number of vertical WRF grid levels is *n*. Consequently, starting point are *n* vertical WRF-grid triples of temperature $\mathrm{T}_K[i]$, total pressure $\mathrm{P}_{tot}[i]$ and water vapour ratio $\mathrm{Q}_{Kg/Kg}[i]$ with the respective variances $\sigma^2_{T_K}[i]$, $\sigma^2_{P_{tot}}[i]$ and $\sigma^2_{Q_{Kg/Kg}}[i]$ with indices $i = 1..n$. Assuming the WRF hindcast errors (inside a triple and neighboured grid points) are uncorrelated, the input data covariance matrix C_{TPQ} can be constructed by a $(3 \cdot n) \times (3 \cdot n)$ diagonal matrix

$$C_{TPQ} = \begin{bmatrix} C_{TPQ}[1] & \cdots & 0 \\ \vdots & \ddots & \vdots \\ 0 & \cdots & C_{TPQ}[n] \end{bmatrix} \quad (41)$$

which is composed of blocks of

$$C_{TPQ}[i] = \begin{bmatrix} \sigma^2_{T_K}[i], & 0 & 0 \\ 0 & \sigma^2_{P_{tot}}[i] & 0 \\ 0 & 0 & \sigma^2_{Q_{Kg/Kg}}[i] \end{bmatrix} \quad (42)$$

The Jacobian F_{SII} matrix with dimension $(n-1) \times (3 \cdot n)$ is constructed by the outer product

$$F_{SII} = \begin{bmatrix} I_*[1] \\ \vdots \\ I_*[n-1] \end{bmatrix} \cdot \begin{bmatrix} \delta/(\delta \cdot T_K[1]) \\ \delta/(\delta \cdot P_{tot}[1]) \\ \delta/(\delta \cdot Q_{Kg/Kg}[1]) \\ \vdots \\ \delta/(\delta \cdot T_K[n]) \\ \delta/(\delta \cdot P_{tot}[n]) \\ \delta/(\delta \cdot Q_{Kg/Kg}[n]) \end{bmatrix}^T \quad (43)$$

In this equation, the left vector is filled with the respective equation 35, 36 or 37 and is valid (i.e. practically the same) for the first order and second Taylor approximation. Basically, six entries per row need to be computed. These are for the dry effect

$$\frac{\delta \cdot I_{Dry}[i]}{\delta \cdot T_K[i]} = \frac{\delta \cdot I_{Dry}[i]}{\delta \cdot T_K[i+1]} = \frac{2.488 \cdot \mathrm{A2} \cdot k_1 \cdot \sqrt{P_{\mathrm{tot}}[i] \cdot P_{\mathrm{tot}}[1+i]}}{\mathrm{A5} \cdot \mathrm{A6}^2} \quad (44)$$

and

$$\frac{\delta \cdot I_{Dry}[i]}{\delta \cdot P_{tot}[i]} = -\frac{1.244 \cdot \mathrm{A2} \cdot k_1 \cdot P_{\mathrm{tot}}[1+i]}{\mathrm{A5} \cdot \mathrm{A6} \cdot \sqrt{P_{\mathrm{tot}}[i] \cdot P_{\mathrm{tot}}[1+i]}} \quad (45)$$

and

$$\frac{\delta \cdot I_{Dry}[i]}{\delta \cdot Q_{\mathrm{Kg/Kg}}[i]} = \frac{\delta \cdot I_{Dry}[i]}{\delta \cdot Q_{\mathrm{Kg/Kg}}[i+1]} = \frac{2.488 \cdot \mathrm{A2} \cdot k_1 \cdot \sqrt{P_{\mathrm{tot}}[i] \cdot P_{\mathrm{tot}}[1+i]}}{\mathrm{A5}^2 \cdot \mathrm{A6}} \quad (46)$$

and

$$\frac{\delta \cdot I_{Dry}[i]}{\delta \cdot P_{tot}[i+1]} = -\frac{1.244 \cdot \mathrm{A2} \cdot k_1 \cdot P_{\mathrm{tot}}[i]}{\mathrm{A5} \cdot \mathrm{A6} \cdot \sqrt{P_{\mathrm{tot}}[i] \cdot P_{\mathrm{tot}}[1+i]}} \quad (47)$$

The respective six entries for the wet effect are

$$\mathrm{B10} = (h[i]^2 + h[1+i]^2) \cdot (\mathrm{A6} \cdot k_2 + 4 \cdot k_3) - h[i] \cdot h[1+i] \cdot \left(8 \cdot k_3 + 2 \cdot k_2 \cdot (T_K[i] + T_K[1+i])\right) \quad (48)$$

$$\frac{\delta \cdot I_{Wet}[i]}{\delta \cdot T_K[i]} = \frac{\delta \cdot I_{Wet}[i]}{\delta \cdot T_K[i+1]} =$$

$$\frac{2 \cdot \mathrm{B10} \cdot \sqrt{P_{\mathrm{tot}}[i] \cdot P_{\mathrm{tot}}[1+i]} \cdot (Q_{Kg/Kg}[i] + Q_{Kg/Kg}[1+i])}{\mathrm{A5} \cdot \mathrm{A6}^3 \cdot A2}$$

and

$$\mathrm{B11} = h[i] \cdot (\mathrm{A6} \cdot k_2 + 2 \cdot k_3) - h[1+i] \cdot (2 \cdot k_3 + k_2 \cdot (T_K[i] + T_K[1+i])) \quad (49)$$

$$\frac{\delta \cdot I_{Wet}[i]}{\delta \cdot P_{tot}[i]} = -\frac{\mathrm{A2} \cdot \mathrm{B11} \cdot P_{\mathrm{tot}}[1+i] \cdot (Q_{Kg/Kg}[i] + Q_{Kg/Kg}[1+i])}{\mathrm{A5} \cdot \mathrm{A6}^2 \cdot A2 \cdot \sqrt{P_{\mathrm{tot}}[i] \cdot P_{\mathrm{tot}}[1+i]}}$$

$$\frac{\delta \cdot I_{Wet}[i]}{\delta \cdot P_{tot}[i+1]} = -\frac{\mathrm{A2} \cdot \mathrm{B11} \cdot P_{\mathrm{tot}}[i] \cdot (Q_{Kg/Kg}[i] + Q_{Kg/Kg}[1+i])}{\mathrm{A5} \cdot \mathrm{A6}^2 \cdot A2 \cdot \sqrt{P_{\mathrm{tot}}[i] \cdot P_{\mathrm{tot}}[1+i]}}$$

and

$$\mathrm{B12} = -20 \cdot h[i]^3 \cdot h[1+i]^2 \cdot (k_3 + 0.5 \cdot k_2 \cdot (T_K[i] + T_K[1+i])) \quad (50)$$

$$\mathrm{B13} = 20 \cdot h[i]^2 h[1+i]^3 \cdot (k_3 + 0.5 \cdot k_2 \cdot (T_K[i] + T_K[1+i]))$$

$$\mathrm{B14} = h[i] \cdot h[1+i]^4 \cdot (-10 \cdot k_3 - 5 \cdot k_2 \cdot T_K[i] - 5 \cdot k_2 T_K[1+i])$$

$$\mathrm{B15} = h[i]^5 \cdot (-2 \cdot k_3 - k_2 \cdot T_K[i] - k_2 \cdot T_K[1+i])$$

$$\mathrm{B16} = h[i]^4 \cdot h[1+i] \cdot (10 \cdot k_3 + 5 \cdot k_2 \cdot (T_K[i] + T_K[1+i]))$$

$$\mathrm{B17} = \mathrm{B12} + \mathrm{B13} + \mathrm{B14} + \mathrm{B15} + \mathrm{B16} + h[1+i]^5 \cdot (\mathrm{A6} \cdot k_2 + 2 \cdot k_3)$$

$$\frac{\delta \cdot I_{Wet}[i]}{\delta \cdot Q_{Kg/Kg}[i]} = \frac{\delta \cdot I_{Wet}[i]}{\delta \cdot Q_{Kg/Kg}[i+1]} = \frac{2.488 \cdot \mathrm{B17} \cdot \sqrt{P_{\mathrm{tot}}[i] \cdot P_{\mathrm{tot}}[1+i]}}{A2^4 \cdot A5^2 \cdot A6^2}$$

The respective six entries for the total effect are given by

$$\mathrm{B10} = (h[i]^2 + h[1+i]^2) \cdot (\mathrm{A6} \cdot k_2 + 4 \cdot k_3) + h[i] \cdot h[1+i] \cdot (-8 \cdot k_3 - 2 \cdot k_2 \cdot T_K[i] - 2 \cdot k_2 \cdot T_K[1+i]) \quad (51)$$

$$\frac{\delta \cdot I_{Wet}[i]}{\delta \cdot T_K[i]} = \frac{\delta \cdot I_{Wet}[i]}{\delta \cdot T_K[i+1]} =$$

$$\frac{2 \cdot \mathrm{B10} \cdot \sqrt{P_{\mathrm{tot}}[i] \cdot P_{\mathrm{tot}}[1+i]} \cdot (Q_{Kg/Kg}[i] + Q_{Kg/Kg}[1+i])}{\mathrm{A5} \cdot \mathrm{A6}^3 \cdot A2}$$

and

$$\mathrm{B11} = h[i] \cdot (\mathrm{A6} \cdot k_2 + 2 \cdot k_3) + h[1+i] \cdot (-2 \cdot k_3 - k_2 \cdot (T_K[i] + T_K[1+i])) \quad (52)$$

$$\frac{\delta \cdot I_{Wet}[i]}{\delta \cdot P_{tot}[i]} = -\frac{\mathrm{A2} \cdot \mathrm{B11} \cdot P_{\mathrm{tot}}[1+i] \cdot (Q_{Kg/Kg}[i] + Q_{Kg/Kg}[1+i])}{\mathrm{A5} \cdot \mathrm{A6}^2 \cdot A2 \cdot \sqrt{P_{\mathrm{tot}}[i] \cdot P_{\mathrm{tot}}[1+i]}}$$

$$\frac{\delta \cdot I_{Wet}[i]}{\delta \cdot P_{tot}[i+1]} = -\frac{\mathrm{A2} \cdot \mathrm{B11} \cdot P_{\mathrm{tot}}[i] \cdot (Q_{Kg/Kg}[i] + Q_{Kg/Kg}[1+i])}{\mathrm{A5} \cdot \mathrm{A6}^2 \cdot A2 \cdot \sqrt{P_{\mathrm{tot}}[i] \cdot P_{\mathrm{tot}}[1+i]}}$$

and

$$\mathrm{B12} = -20 \cdot h[i]^3 \cdot h[1+i]^2 \cdot (k_3 + 0.5 \cdot k_2 \cdot (T_K[i] + T_K[1+i])) \quad (53)$$

$$\mathrm{B13} = 20 \cdot h[i]^2 h[1+i]^3 \cdot (k_3 + 0.5 \cdot k_2 \cdot (T_K[i] + T_K[1+i]))$$

$$\mathrm{B14} = h[i] \cdot h[1+i]^4 \cdot (-10 \cdot k_3 - 5 \cdot k_2 \cdot T_K[i] - 5 \cdot k_2 T_K[1+i])$$

$$\mathrm{B15} = h[i]^5 \cdot (-2 \cdot k_3 - k_2 \cdot T_K[i] - k_2 \cdot T_K[1+i])$$

$$\mathrm{B16} = h[i]^4 \cdot h[1+i] \cdot (10 \cdot k_3 + 5 \cdot k_2 \cdot (T_K[i] + T_K[1+i]))$$

$$\mathrm{B17} = \mathrm{B12} + \mathrm{B13} + \mathrm{B14} + \mathrm{B15} + \mathrm{B16} + h[1+i]^5 \cdot (\mathrm{A6} \cdot k_2 + 2 \cdot k_3)$$

$$\frac{\delta \cdot I_{Wet}[i]}{\delta \cdot Q_{Kg/Kg}[i]} = \frac{\delta \cdot I_{Wet}[i]}{\delta \cdot Q_{Kg/Kg}[i+1]} = \frac{2.488 \cdot \mathrm{B17} \cdot \sqrt{P_{\mathrm{tot}}[i] \cdot P_{\mathrm{tot}}[1+i]}}{A2^4 \cdot A5^2 \cdot A6^2}$$

Again, in order to support an independent implementation, the construction principle for the Jacobian matrix for the dry effect is provided. The entries in this matrix correspond to the equations with the respective enumeration. Practically, the six equations are arranged row wise:

$$F_{SII} = \begin{bmatrix} eq44 & eq45 & eq46 & eq44 & eq47 & eq46 & 0 & \cdots & 0 & 0 \\ 0 & 0 & 0 & eq44 & eq45 & eq46 & eq44 & eq47 & eq46 & 0 \\ 0 & 0 & 0 & 0 & 0 & 0 & eq44 & eq45 & eq46 & \cdots \end{bmatrix} \begin{matrix} i=1 \\ i=2 \\ \vdots \end{matrix} \quad (54)$$

The current implementation of the troposphere effect mitigation processor converts the individual segment integrals into units of Millimetre. For this reason, $I_{Dry}[i]$, $I_{Wet}[i]$ and $I_{total}[i]$ (i.e. eq. 35, 36 and 37) are multiplied with the factor 0.001. As a result, the variance is estimated in mm^2. Consequently, the above matrix needs to be multiplied with the factor 0.001 too.

The final summation of the segment integrals according to equation 38 has a straight forward Jacobian matrix F_{Sum} with dimension *1 x (n-1)*. The reason is the un-weighted sum of *(n-1)* segments.

$$F_{Sum} = \left[I_*[1] + I_*[2] + \cdots + I_*[n-1]\right] \cdot \begin{bmatrix} \delta/(\delta \cdot I_*[1]) \\ \vdots \\ \delta/(\delta \cdot I_*[n-1]) \end{bmatrix}^T = [1 \quad \cdots \quad 1] \quad (55)$$

With equation 40, the standard deviation of the zenith path delay is finally computed by $\sigma_{\mathrm{ZPD}} = \sqrt{\mathrm{C_I}}$ which can be converted into an approximation of the LOS path delay with the local incidence angle ϑ using a straight forward mapping function e.g.

$$\sigma_{LOS} = \sqrt{\left(\frac{\sigma_{ZPD}}{cos(\vartheta)}\right)^2} \qquad (56)$$

Some typical examples for the error propagation are provided in order to illustrate the sensitivity with respect to the WRF hindcast parameters. Seven uncertainty scenarios for the sounding data from the 23th January 1997 in Thessaloniki are assumed and the resulting standard deviations for the wet, dry and total range error are calculated. Figure 44 visualizes the vertical profile of pressure, temperature and water vapour mixing ratio and the corresponding refractivity components. Table 3 collects all results for the test cases, where scenario 1 has a constant standard deviation of pressure and temperature from 0 to 23 km altitude. Scenario 2 and 3 have a constant standard deviation of the water vapour mixing ratio from 0 to 4 km altitude (above it is zero). In scenario 4 and 5, the standard deviation of the water vapour mixing ratio is constant from 0 to 2 km altitude and zero above. In the previous examples, the integration over the refractivity is performed in the complete altitude range from ground to 23 km in order to provide the total error propagation values. The last two scenarios (i.e. 6 and 7) demonstrate the main error source in the estimation of the path delay. Scenario 6 and 7 assume a constant standard deviation of the water vapour mixing ratio from 0 – 1 km altitude and a constant standard deviation for the total pressure and temperature over the range from 0 to 23 km altitude. In scenario 6, the integration over the refractivity is performed over the full 23 km altitude range and in scenario 7 only the range from ground to 1.5 km altitude is integrated. Interestingly, the standard deviations of the estimated path delay components are very similar. It is a consequence of the water vapour mixing ratio uncertainty close to the surface up to 1.5 km altitude being the main error source in the estimation of the path delay. The configuration of the test scenarios is visualized in Figure 45.

Table 3: example test cases for the sensitivity of the precision WRF parameters

	input: assumption			**output: precision**		
	σ_{T_K}	$\sigma_{P_{tot}}$	$\sigma_{Q_{g/Kg}}$	$\sigma_{ZPD_{Dry}}$	$\sigma_{ZPD_{Wet}}$	$\sigma_{ZPD_{total}}$
scenario 1	$1.0\ K$	$1.0\ hPa$	$0.0\ g/Kg$	$2.5\ mm$	$0.2\ mm$	$2.6\ mm$
scenario 2	$0.0\ K$	$0.0\ hPa$	$1.0\ g/Kg$	$16.6\ mm$	$306.2\ mm$	$289.7\ mm$
scenario 3	$0.0\ K$	$0.0\ hPa$	$0.1\ g/Kg$	$5.2\ mm$	$96.8\ mm$	$91.6\ mm$
scenario 4	$0.0\ K$	$0.0\ hPa$	$1.0\ g/Kg$	$13.0\ mm$	$235.9\ mm$	222.9
scenario 5	$0.0\ K$	$0.0\ hPa$	$0.1\ g/Kg$	$4.1\ mm$	$74.6\ mm$	$70.5\ mm$
scenario 6	$1.0\ K$	$1.0\ hPa$	$0.1\ g/Kg$	$4.0\ mm$	$57.2\ mm$	$54.1\ mm$
scenario 7	$1.0\ K$	$1.0\ hPa$	$0.1\ g/Kg$	$3.3\ mm$	$57.2\ mm$	$54.1\ mm$

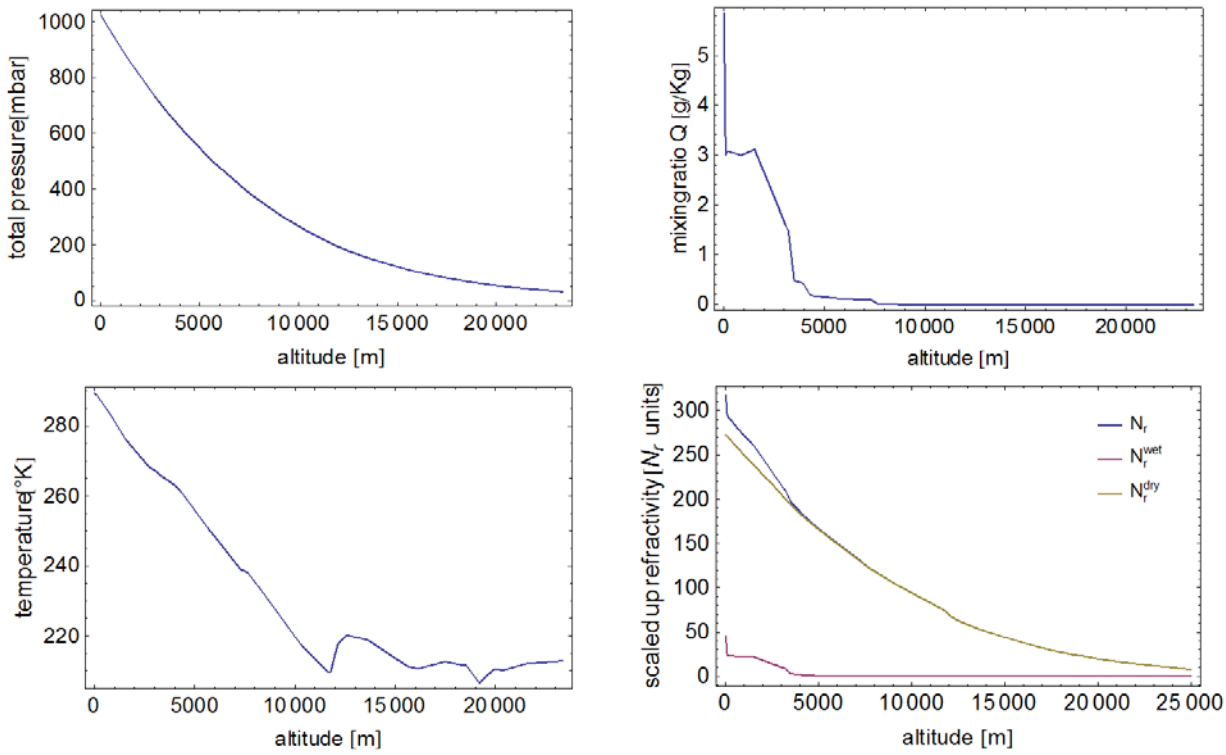

Figure 44: example profile from sounding at 23. February 1997 at 12:00 Thessaloniki.

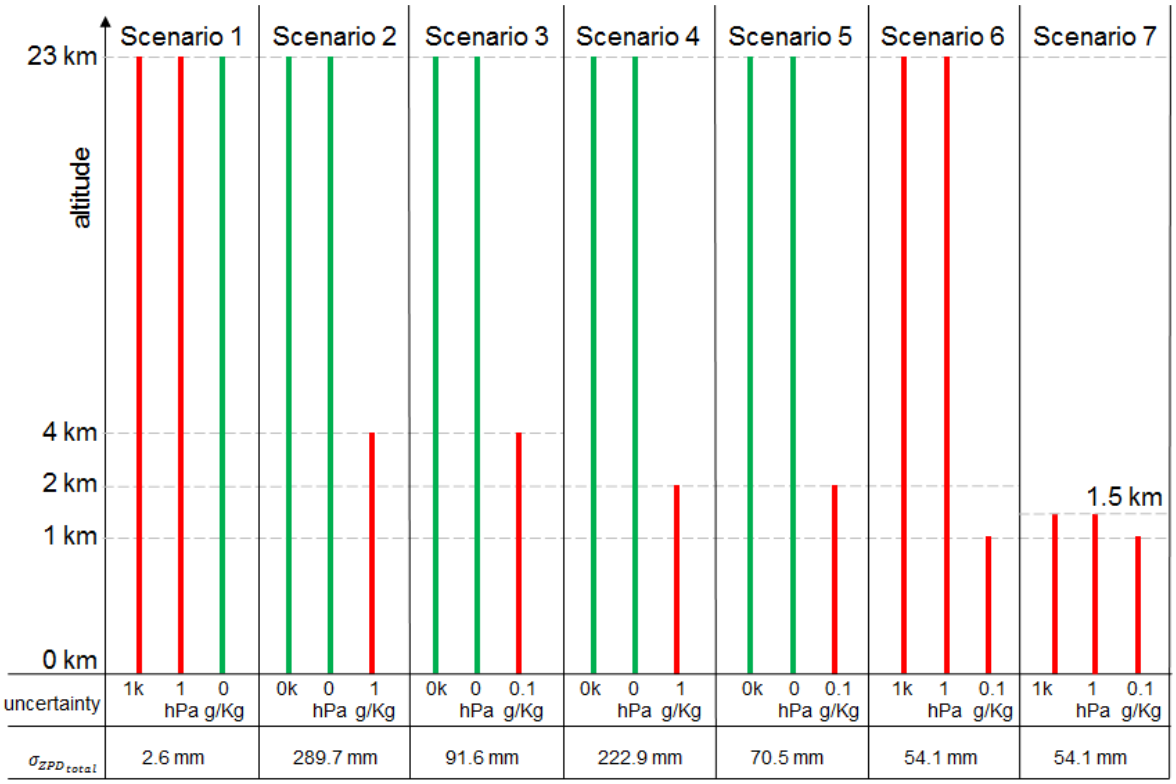

Figure 45: visualisation of the configurations of test scenarios of Table 3

8.1.2 ALGORITHM 2: LOS PATH DELAY WITH PHYSICS PARAMETER INTERPOLATION

The zenith path delay algorithm can be extended into the LOS estimation. The assumption is that the variation of the atmosphere parameters and their non-linear characteristic is dominant in vertical direction and the parameters vary smoothly in horizontal direction. Figure 46 provides a vertical atmosphere profile from a WRF hindcast of the total pressure to illustrate this assumption. Obviously, the pressure changes vertically quickly (indicated by the colour changes from blue to green and finally red) and is in horizontal direction smooth (indicated by the similar colour).

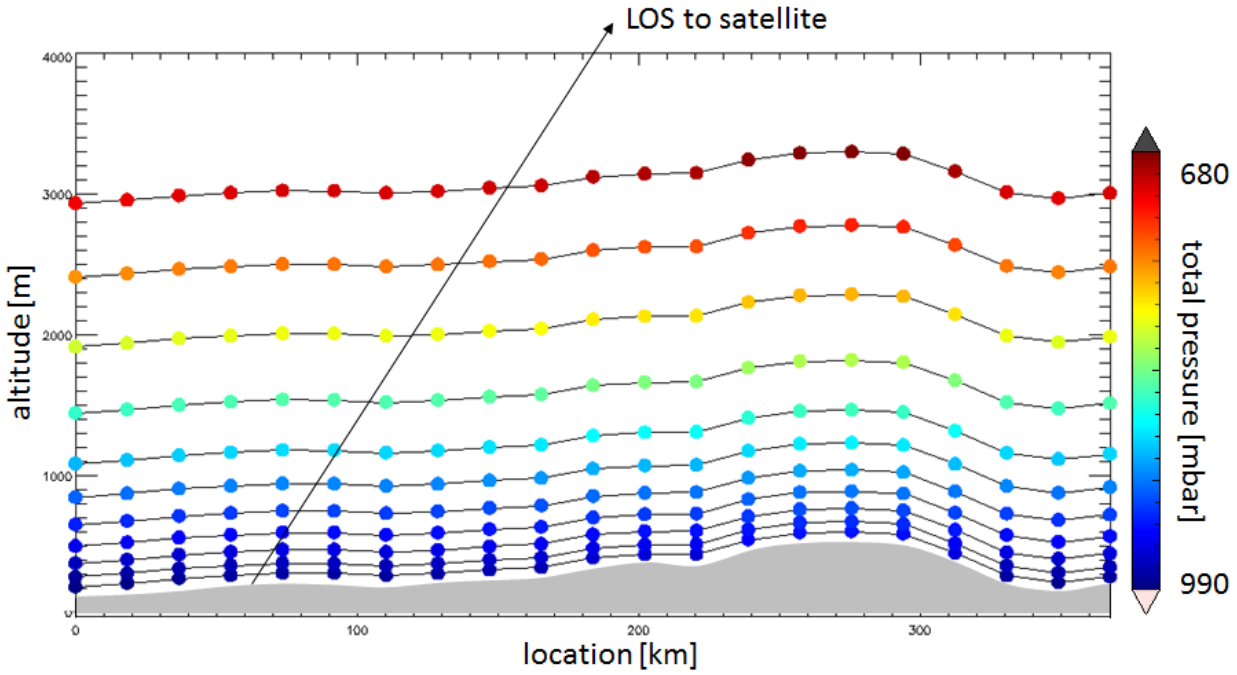

Figure 46: vertical atmosphere profile from a WRF hindcast of the total pressure

Evidently, the interpolation in horizontal direction can be performed by straight forward algorithms given a smooth physical parameter field. Actually, a linear interpolation is sufficient in this direction. As a consequence, the direct LOS integration can be implemented by the sequence of the following steps. Firstly, the intersections of the LOS with the horizontal WRF grid are calculated (orange dots in Figure 47). Secondly for this location, the atmosphere parameters $P_{tot}^{LOS}[i]$, $T_K^{LOS}[i]$ and $P_{Kg/Kg}^{LOS}[i]$ but also the orthonormal height $h^{LOS}[i]$ can be linearly interpolated from the four horizontal neighbours from the WRF grid (blue dots in Figure 47). Following modest assumptions (i.e. linear interpolation of temperature, water vapour and log-linear interpolation of pressure with respect to the orthonormal height), the integrals of the refractivity components along the LOS and the respective error propagation can directly by computed using the equations from the previous section. The third step is consequently evaluation of equations 35, 36, 37 for the segment integrals of the respective refractivity components and the evaluation of equation 40 using equations 39, 54 and 55 with $P_{tot}^{LOS}[i]$, $T_K^{LOS}[i]$, $P_{Kg/Kg}^{LOS}[i]$ and $h^{LOS}[i]$ as input. Of course, the longer integration path

needs to be considered. The most simple implementation is the correction according the incidence angle ϑ, i.e. by multiplication with the factor $1/cos(\vartheta)$.

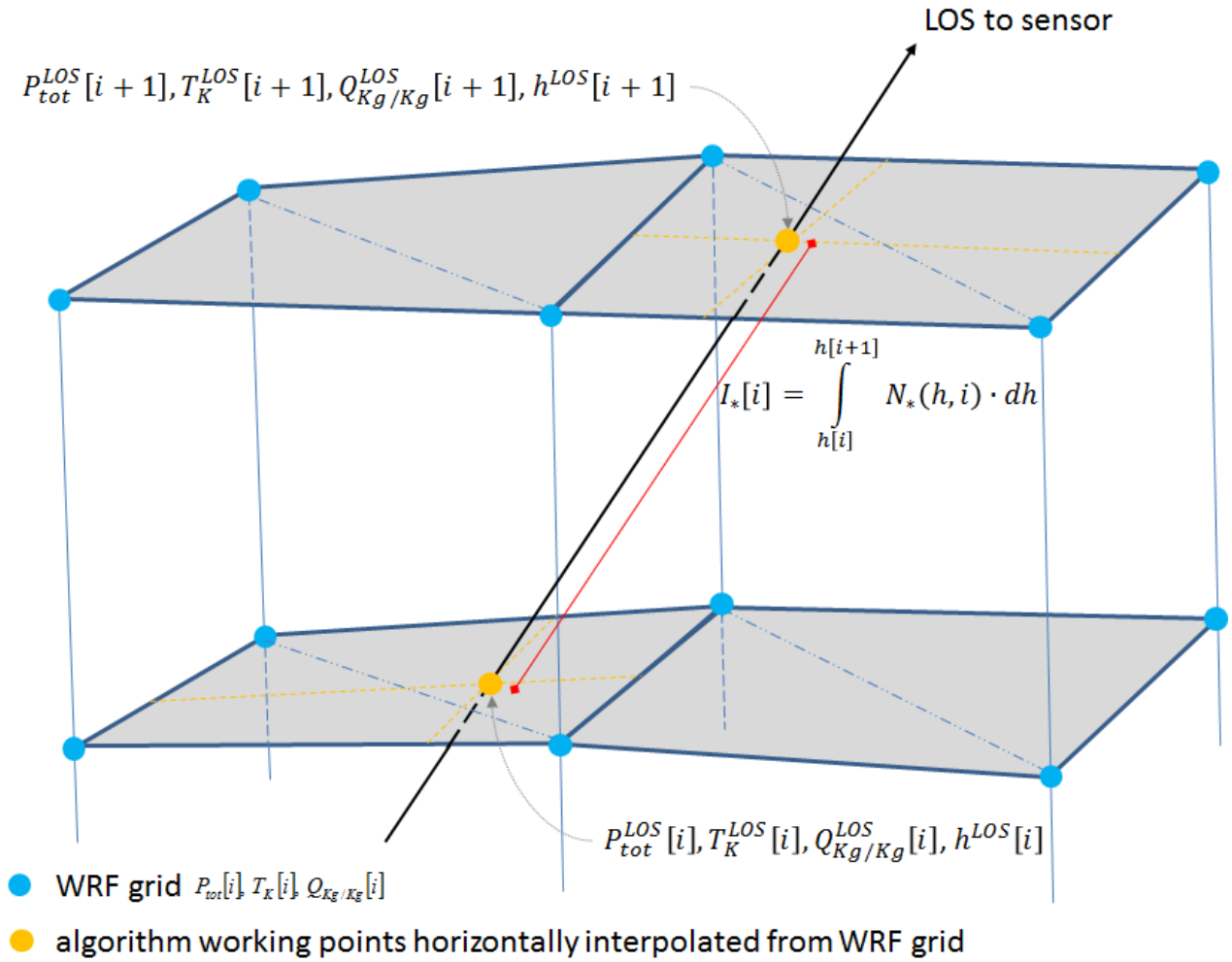

Figure 47: Geometry and principle of the direct LOS integration

8.2 VARIANCES OF WRF HINDCASTS

Now, the variances of the input parameters $\sigma^2_{P_{tot}}$, $\sigma^2_{T_K}$ and $\sigma^2_{Q_{Kg/Kg}}$ are missing for the error propagation assessment. In order to characterize and quantify different effects, the WRF-hindcast uncertainty is estimated by experiments.

8.2.1 EXPERIMENTAL SETUP

Subject is to estimate the precision of the hindcast parameters total pressure P_{tot}, temperature T_K and water vapour mixing ratio $Q_{Kg/Kg}$. However, the systematic effects need to be separated from the random uncertainties. As a consequence, a complicated

experiment setup is needed. In the WRF system, many processing parameters can be tuned in order to optimize the prediction with respect to the actual physical processes i.e. regarding the concrete weather situation, topography and season (e.g. clouds, graupel and ice). This is the reason, suitable physics parameter settings for the weather model need to be determined in a first step. In a second step, the required vertical sampling of the NWP has been verified.

Different physics parameterisations are implemented in the WRF software. The use of unsuitable physics parameterisations results in systematic errors which can exceed the typical error figures. In the course of this assessment, the micro physics, the turbulence in the boundary layer and the cloud physics are tuned. Table 4 provides the respective physics parameter settings for different test cases. For each of these test cases, several WRF hindcasts are simulated and compared with independent sounding data. Seasonal effects are considered by assessing summer and winter test cases independently. Figure 48 provides a winter example for different hindcasts resulting from changed physics settings. The plot is restricted to the layer between the surface and two kilometres height. For every numerical weather prediction, this region is very difficult to simulate due to complex physical processes and the limited data basis (e.g. local ground cover, soil humidity, temperature variations from shadow and turbulence) to model these. The winter assessment shows a temperature difference between the WRF simulations up to three degree and a water vapour mixing ratio deviation of about one g/Kg close to the ground. For temperature, the physics option sets two, three and four are not suitable to model the actual test site effects. Obviously, the simulations with the first and fifth option sets (green dash-dot-dot-dotted and blue) are more close to the sounding temperature profile. The summer assessment is visualized in Figure 49. In this test case, all physics option settings perform equally well. This suggests that all physics models can cope with typical summer processes. This figure also shows that the deviation from the independent sounding temperature profile is in the range of one to four degree Celsius. Unfortunately, this error cannot be removed (as a systematic effect) by changing the physics parameters and as a consequence, it needs to be considered as an uncertainty of the hindcast. As a result of the assessment, the physics options set one is selected to be the default in all WRF simulations for this test site and kept constant in all following experiments.

Besides the above physics comparison, Figure 48 and Figure 49 visualize another effect. Obviously, the WRF simulation is very smooth compared to the independent sounding data. The sounding data in this example show that abrupt changes in temperature and water vapour mixing ratio are physically realistic in vertical direction. Of course, the vertical sampling in the WRF model should allow the representation of these abrupt effects. In particular, an under-sampling would introduce systematic errors. The WRF manual recommends 28 vertical levels for the simulation. Figure 50 demonstrates that only small variations finally result by changing the number of vertical levels in the WRF hindcast. Practically, 50 (red dashed), 70 (green dash-dotted), 150 (blue) vertical levels provide a similar result. This is the reason, the smallest of these numbers i.e. fifty vertical levels are selected to be the default in all WRF simulations for this test site and kept constant in all following experiments.

Table 4: checked physics settings in WRF

	physics 1 (default)	physics 2	physics 3	physics 4	physics 5
mp_physics	3	5	5	5	8
bl_pbl_physics	1	99	1	99	1
cu_physics	1	3	3	1	1
diff_opt	1	2	2	1	1
km_opt	4	4	4	4	1

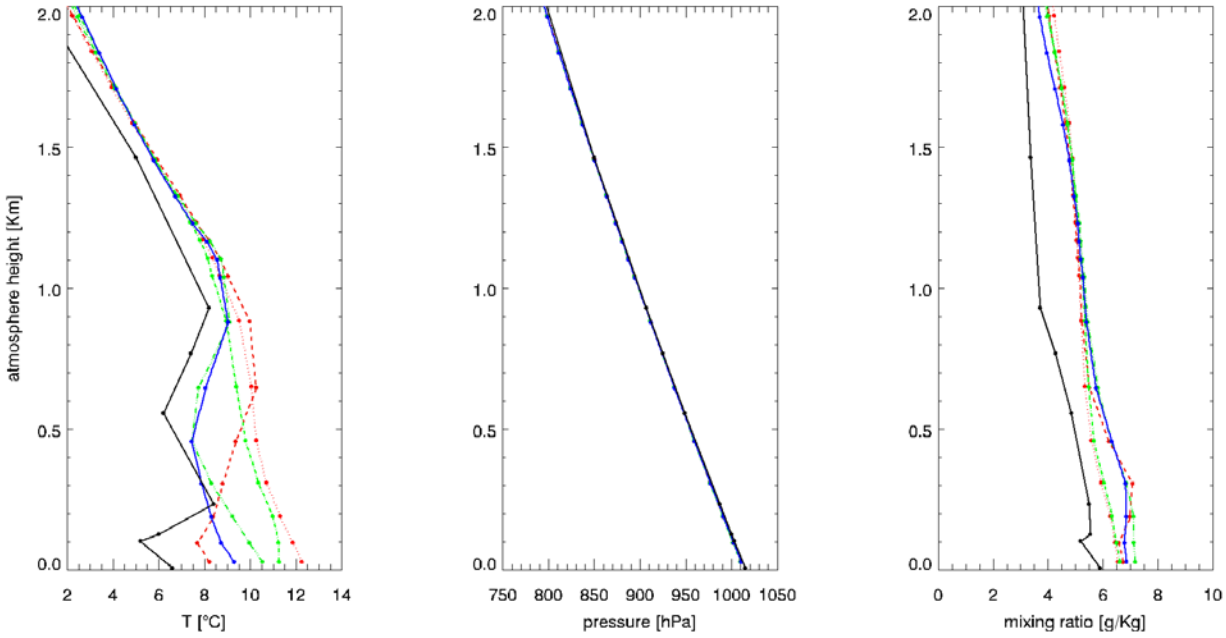

Figure 48: winter validation of different physics options in NWP (red dotted: physics options set two, red dashed: physics options set three, green dash-dotted: physics options set four, green dash-dot-dot-dotted: physics options set five, blue: default physics options set one, black: independent sounding data)

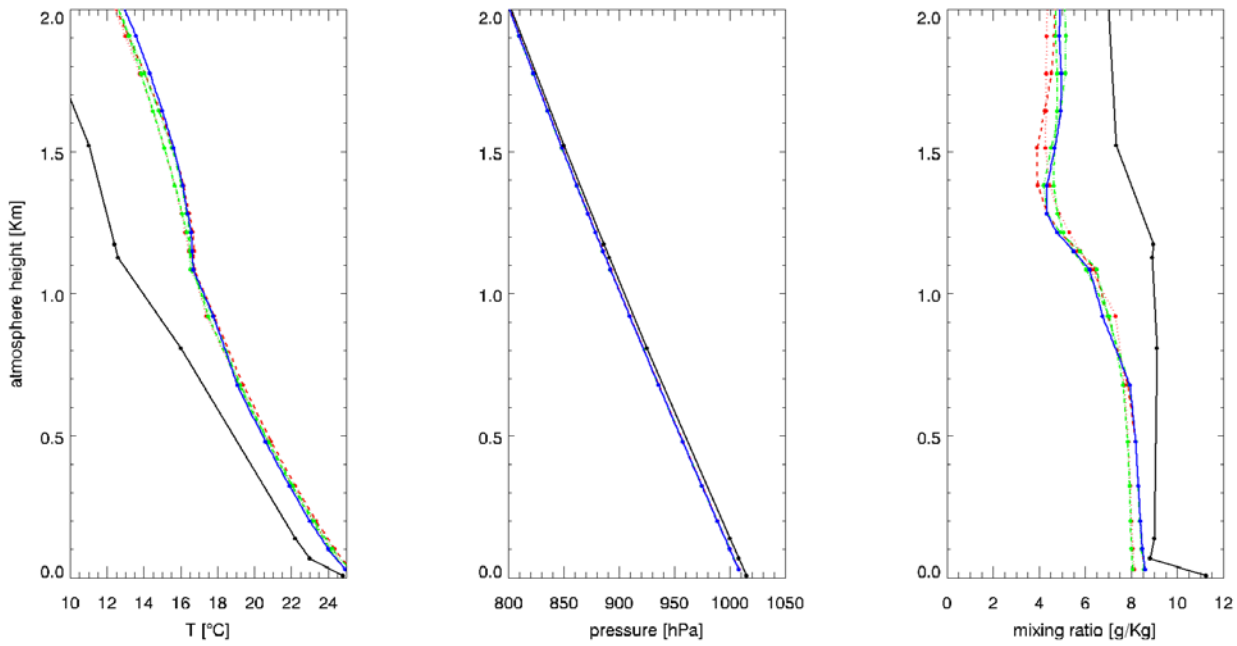

Figure 49: summer validation of different physics options in NWP (red dotted: physics options set two, red dashed: physics options set three, green dash-dotted: physics options set four, green dash-dot-dot-dotted: physics options set five, blue: default physics options set one, black: independent sounding data)

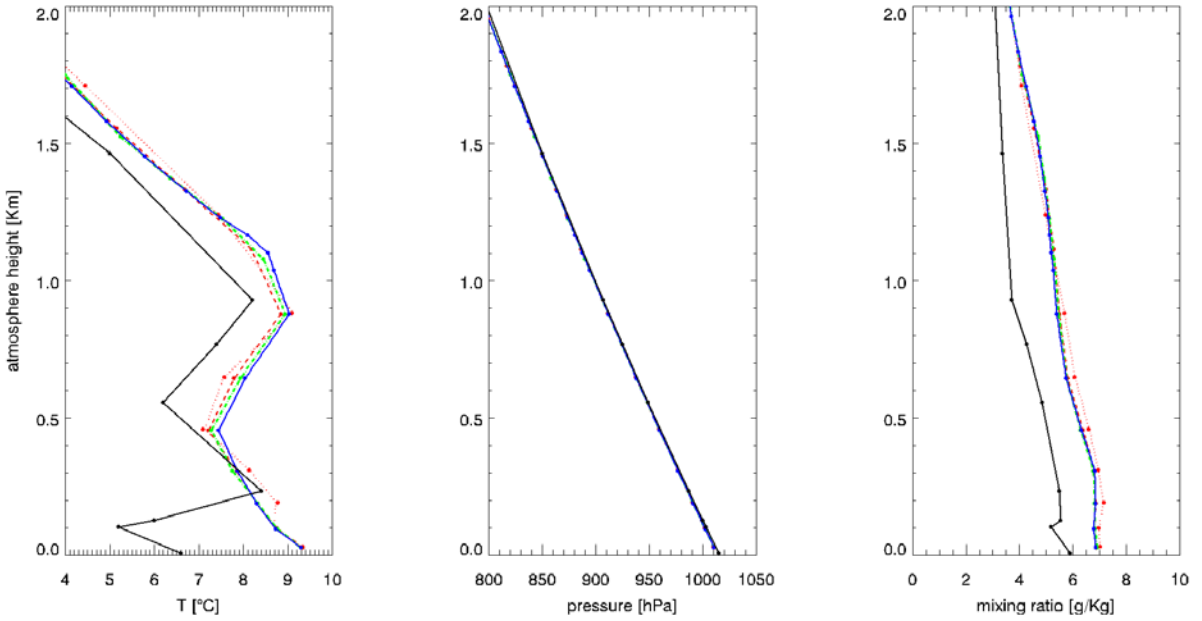

Figure 50: Assessment of the required vertical resolution in the hindcast: 28 levels (red dotted), 50 levels (red dashed), 70 levels (green dash-dotted), 150 levels (blue). Fifty vertical levels are sufficient for this example from the winter test case.

8.2.2 EXPECTED PRECISION OF NWP

In this test, the parameters related to the atmosphere physics are kept constant. However, the NWP resolution is varied to demonstrate the sensitivity of the WRF processing parameters. In the end, the result is an ensemble of atmosphere parameters which facilitate the precision assessment.

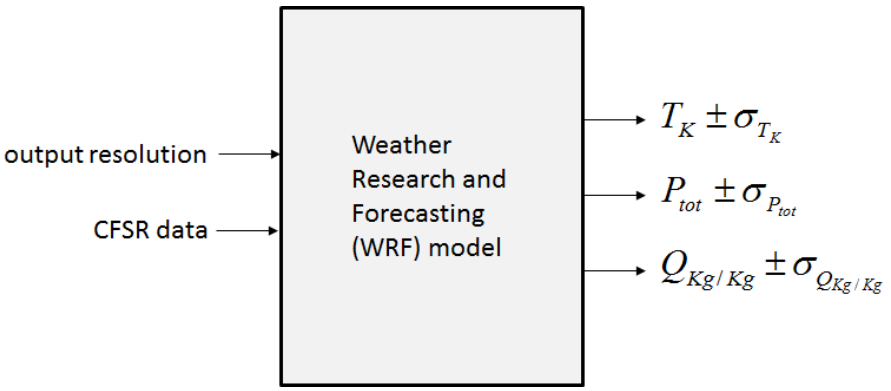

Figure 51: setup to estimate the precision of the WRF output parameters

The NWP is computed for 100 m, 150 m, 200 m, 300 m and 1 km resolution. Figure 52, Figure 53 and Figure 54 show the respective profiles (for a small altitude) for a fixed i.e. one and the same location. These figures demonstrate the variation and finally the precision of the predicted troposphere temperature, water vapour mass mixing ratio and the total atmosphere pressure. Notably, the NWP cannot perfectly model the high turbulence near the ground (i.e. the boundary layer).

Figure 55, Figure 56 and Figure 57 visualize the respective profiles up to an altitude of 20 km. The basically similar graph proves the stability of the WRF processing which is a challenge for high resolution because of the small model time step. Practically, the time step is limited by the Courant number. An estimation of the prediction parameter uncertainty is presented in Table 5. Actually, the standard deviation of the WRF output parameters varies with the altitude caused by the wide range of values of the output parameters. This is the reason the percent error (i.e. the relative error) is presented in Figure 58, Figure 59 and Figure 60. Typically, the percent error $\Delta x_{rel[\%]}$ for a measurement $\hat{x}$ is defined with respect to the true value x_{true} by

$$\Delta x_{rel[\%]} = \left| \frac{\hat{x} - x_{true}}{x_{true}} \right| \cdot 100\% \quad , \left(x_{true} \neq 0 \right) \tag{57}$$

In this assessment, it is estimated from the data using the standard deviation of the measurements $\sigma_{\hat{x}} = \sqrt{Var\{\hat{x}\}}$ by

$$\Delta x_{rel[\%]} = \left| \frac{\sigma_{\hat{x}}}{E\{\hat{x}\}} \right| \cdot 100\% \quad , \left(E\{\hat{x}\} \neq 0 \right) \tag{58}$$

This definition of the percent error describes an interval $\hat{x} \pm \sigma_{\hat{x}}$ around the estimated value by the precision uncertainty $\sigma_{\hat{x}}$ based on the measurement $\hat{x}$.

$$\hat{x} \pm \sigma_{\hat{x}} = \hat{x} \pm \left(\hat{x} \cdot \frac{\Delta x_{rel[\%]}}{100\%} \right) \quad , (\hat{x} \neq 0) \tag{59}$$

The interval $\hat{x} \pm \sigma_{\hat{x}}$ covers 68.3% of all measurement errors assuming a normal distribution of the measurement error. Equation (59) allows a straight forward description of the input parameters precision for the error propagation assessment.

Table 5: Precision of the WRF atmosphere parameters

	0-2 km	2-10 km	10-20 km
std. dev. of pressure [hPa]	0.24	0.2	0.1
std. dev. of abs. temperature [K]	0.2	0.2	0.5
std. dev. of vapour mixing ratio [g/Kg]	0.15	0.033	0.0006

The shown variation of the result parameters with respect to different WRF-setup parameters provides the information on the precision of the NWP. In contrast, the following comparison with independent sounding data provides the accuracy of the NWP.

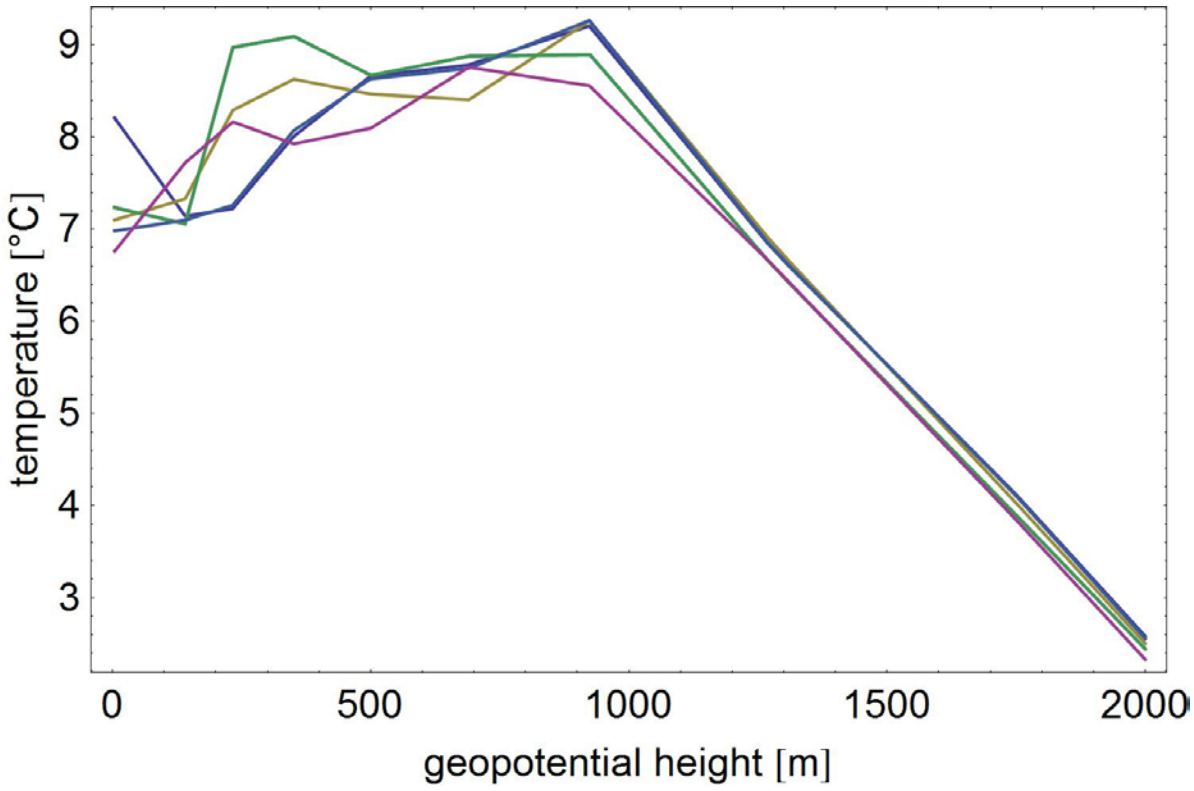

Figure 52: variation of temperature prediction depending on the NWP resolution (100m, 150m, 200m, 300m and 1km resolution) with the range of typical topography

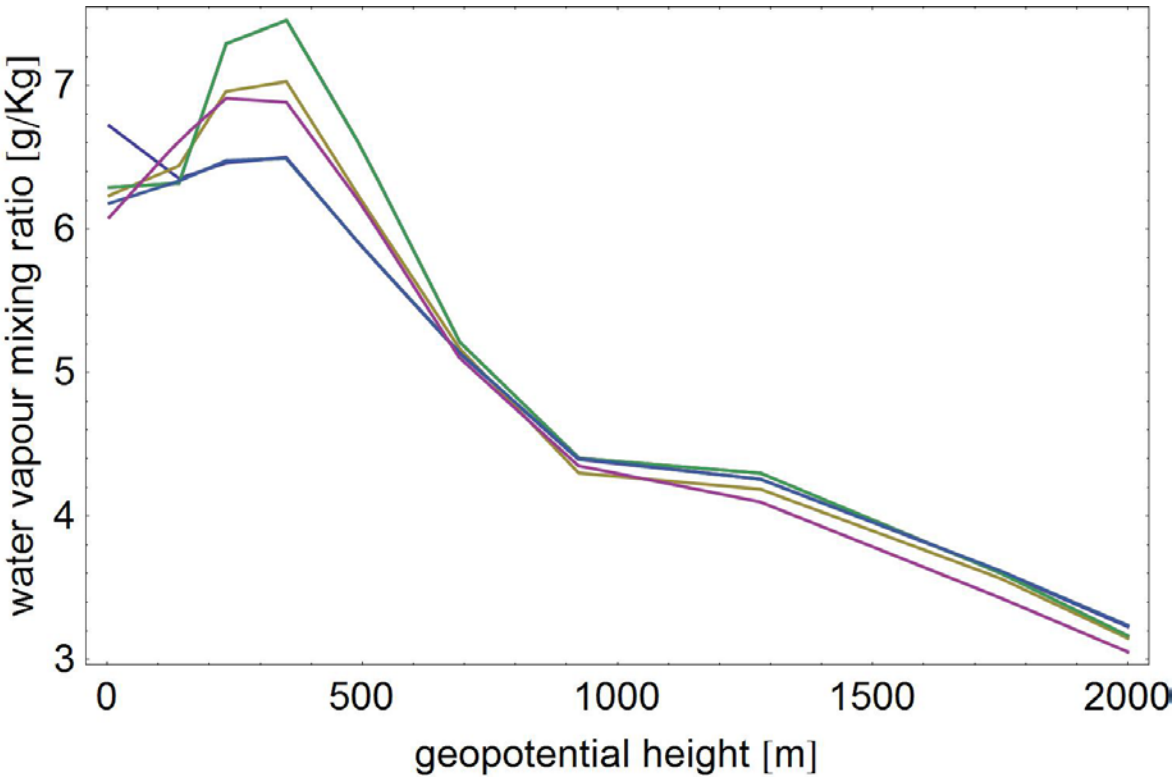

Figure 53: variation of water vapour mass mixing ratio prediction depending on the NWP resolution (100m, 150m, 200m, 300m and 1km resolution) with the range of typical topography

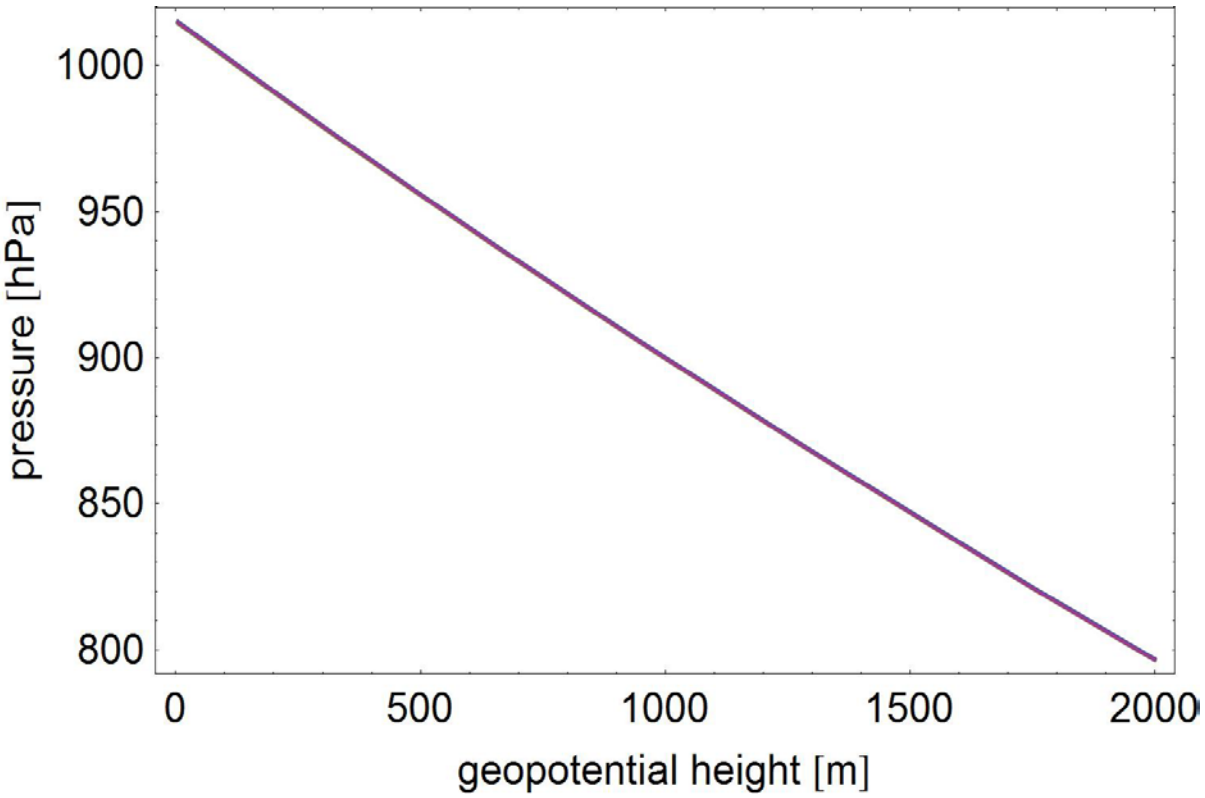

Figure 54: variation of the total pressure prediction depending on the NWP resolution (100m, 150m, 200m, 300m and 1km resolution) with the range of typical topography

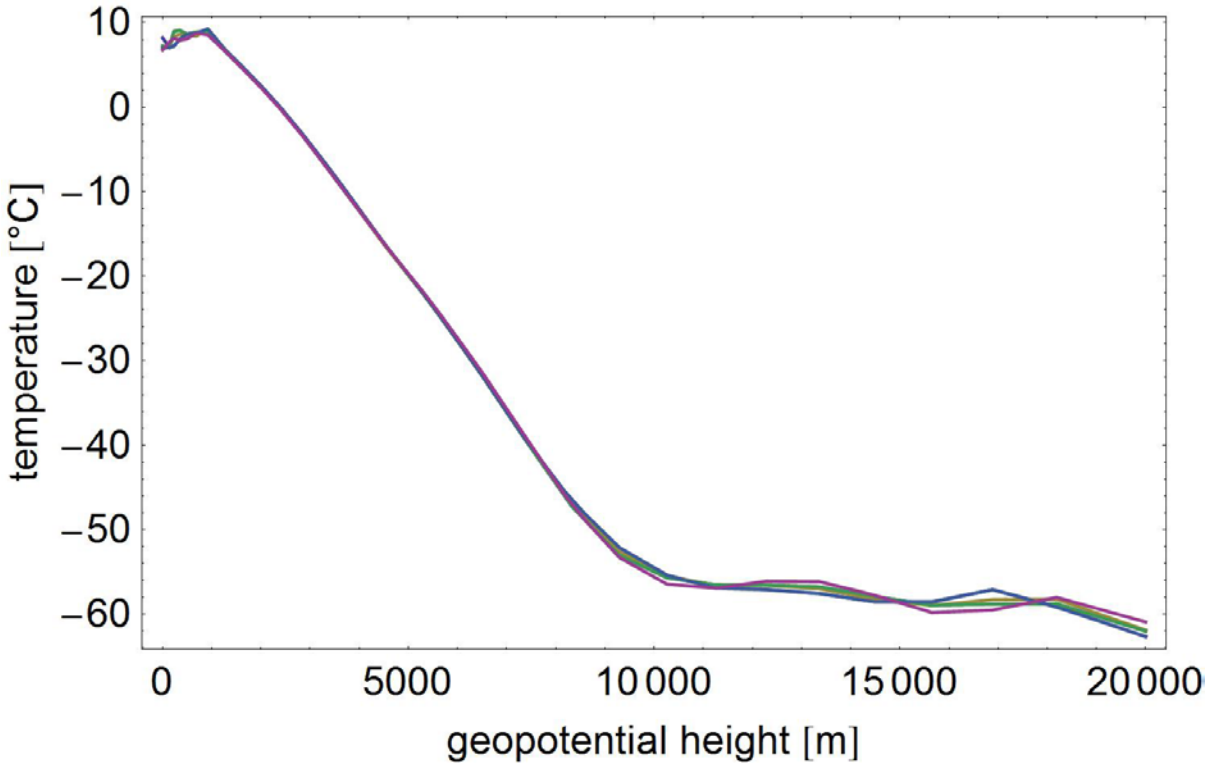

Figure 55: variation of temperature prediction depending on the NWP resolution (100m, 150m, 200m, 300m and 1km resolution) on the total relevant range.

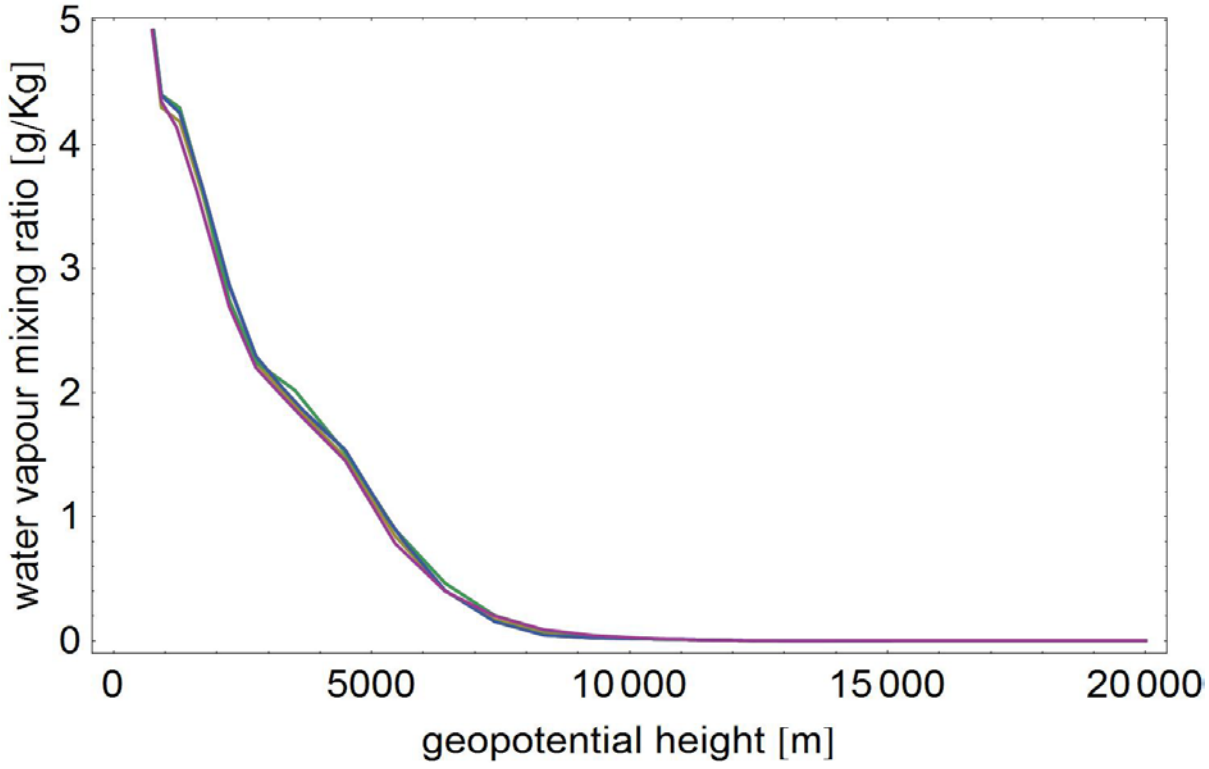

Figure 56: variation of water vapour mass mixing ratio prediction depending on the NWP resolution (100m, 150m, 200m, 300m and 1km resolution) on the total relevant range

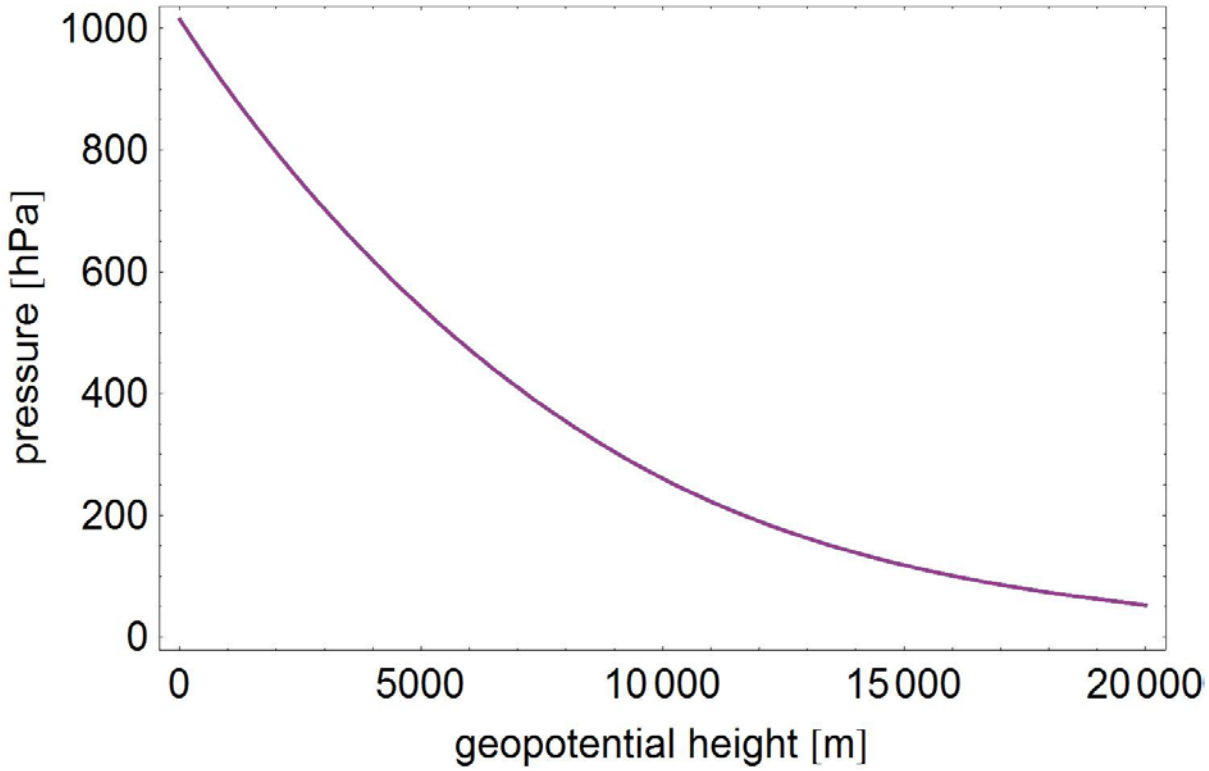

Figure 57: variation of the total pressure prediction depending on the NWP resolution (100m, 150m, 200m, 300m and 1km resolution) on the total relevant range

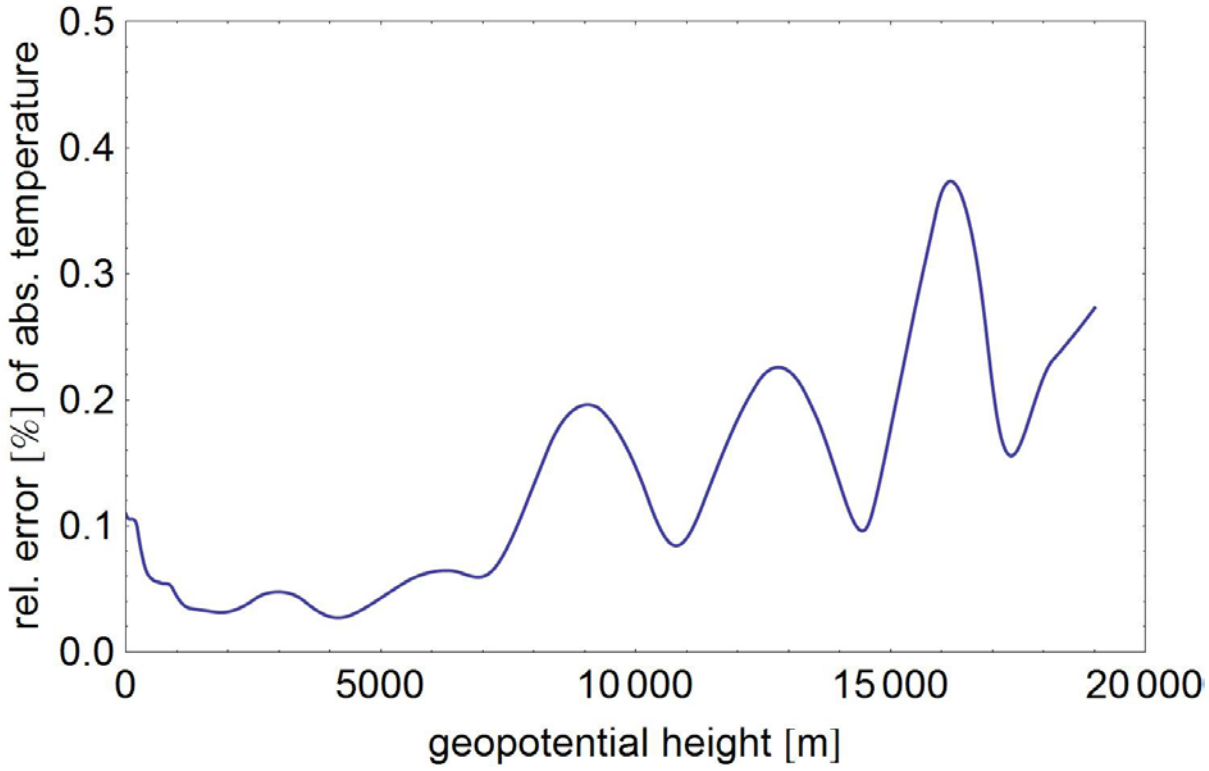

Figure 58: percent error (relative error) of absolute temperature $\Delta T_{rel\,[\%]}$ [%]

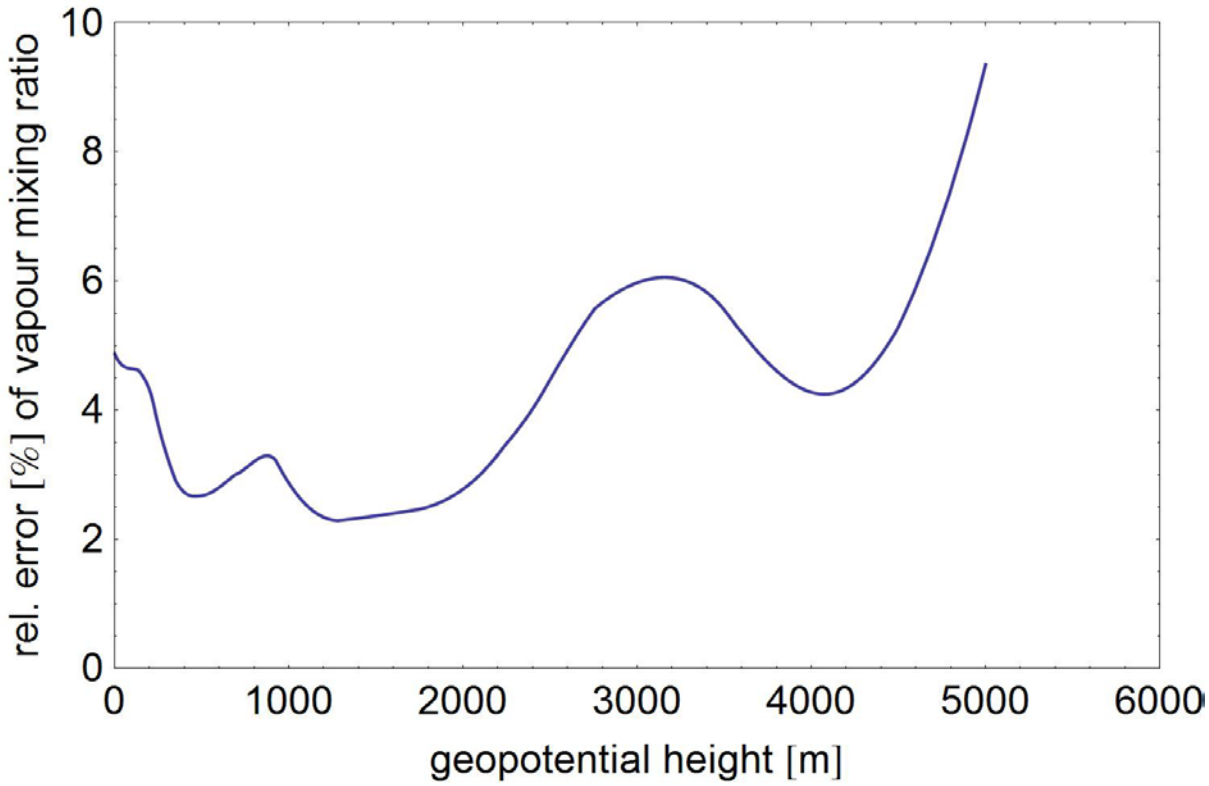

Figure 59: percent error (relative error) of vapour mixing ratio $\Delta Q_{rel[\%]}$ [%]

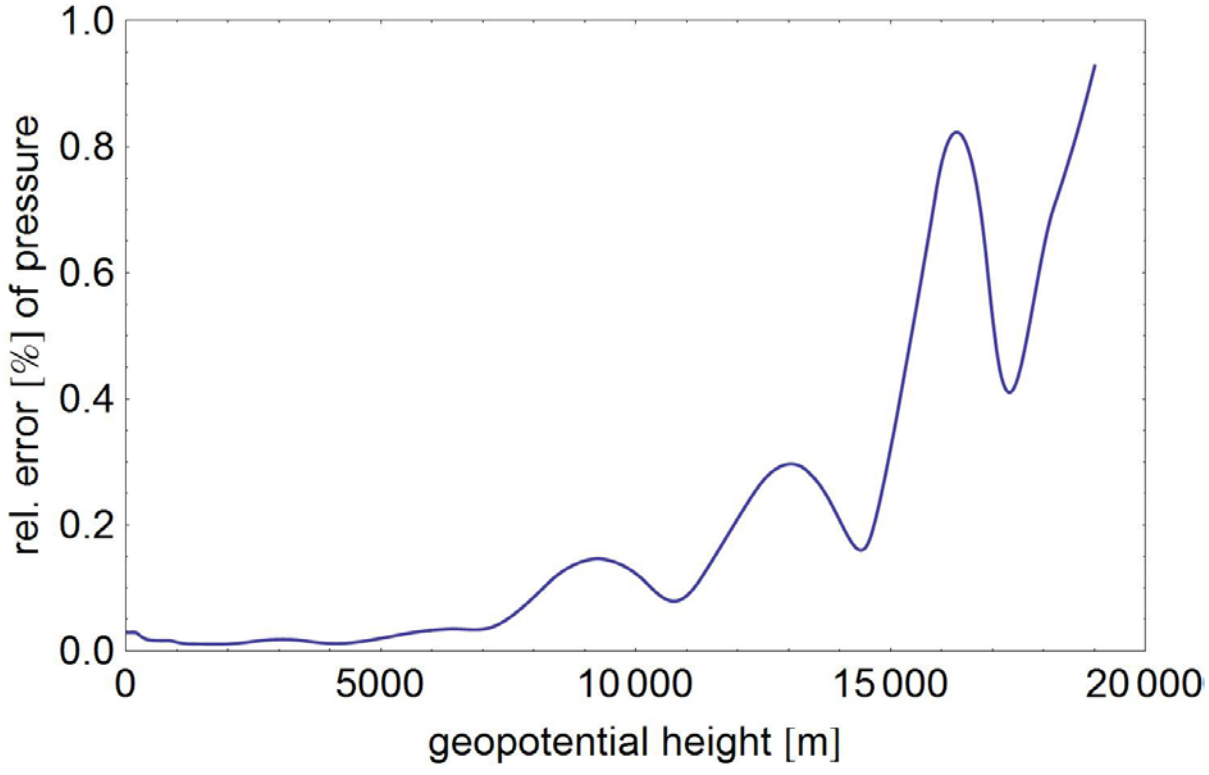

Figure 60: percent error (relative error) of total pressure $\Delta P_{rel[\%]}$ [%]

8.2.3 EXPECTED ACCURACY OF NWP

Sounding data are used to compare the NWP with the real atmosphere state. These data are an alternative data source which also makes the troposphere parameters (temperature, pressure and partial water vapour pressure) available for the refractivity estimation. For this assessment, the high vertical resolution and the direct measurement in the lower troposphere of the sounding are utilized. The University of Wyoming provides historical and actual sounding data [19] which are typically based on the Integrated Global Radiosonde Archive (IGRA) [20]. Figure 61 shows the world wide available sounding stations. Actually, two stations are covered by the Greece WAP test site. In this report, the sounding station at the Thessaloniki Airport is used in order to assess the accuracy of the numerical weather hindcast and finally the refractivity estimation. The station has the identifier “GR 16622” and is located at the longitude of 40.52 degree and latitude of 22.97 degree at height of 8 m. The respective sounding data tables are listed in Appendix 12.

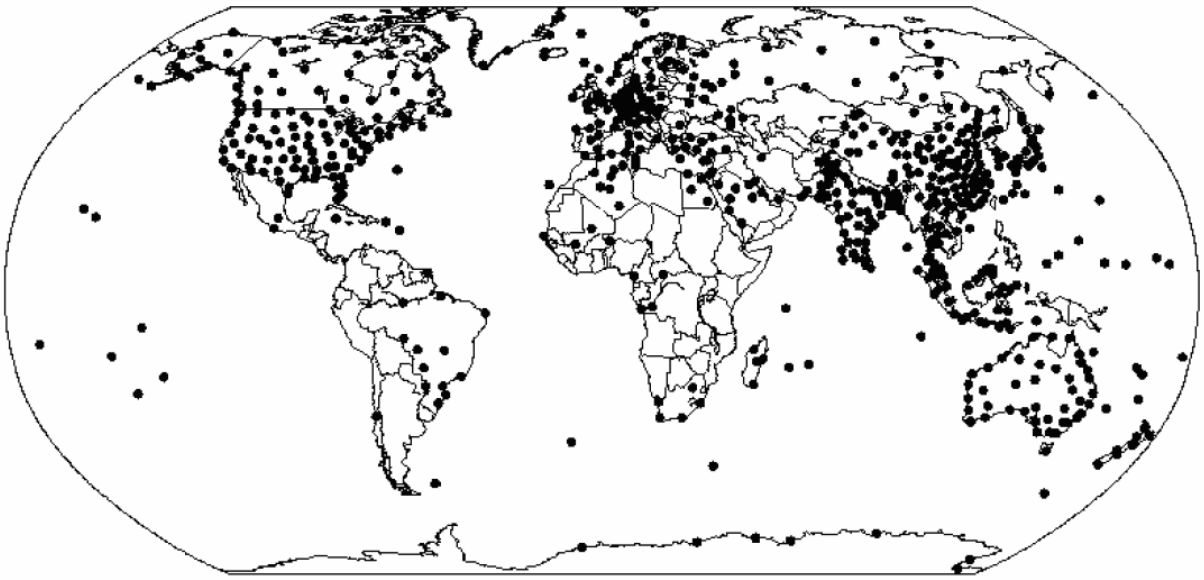

Figure 61: IGRA active stations with half-day acquisition cycle (taken from [20])
(source: https://www.ncdc.noaa.gov/oa/hofn/guan/igra-overview.pdf)

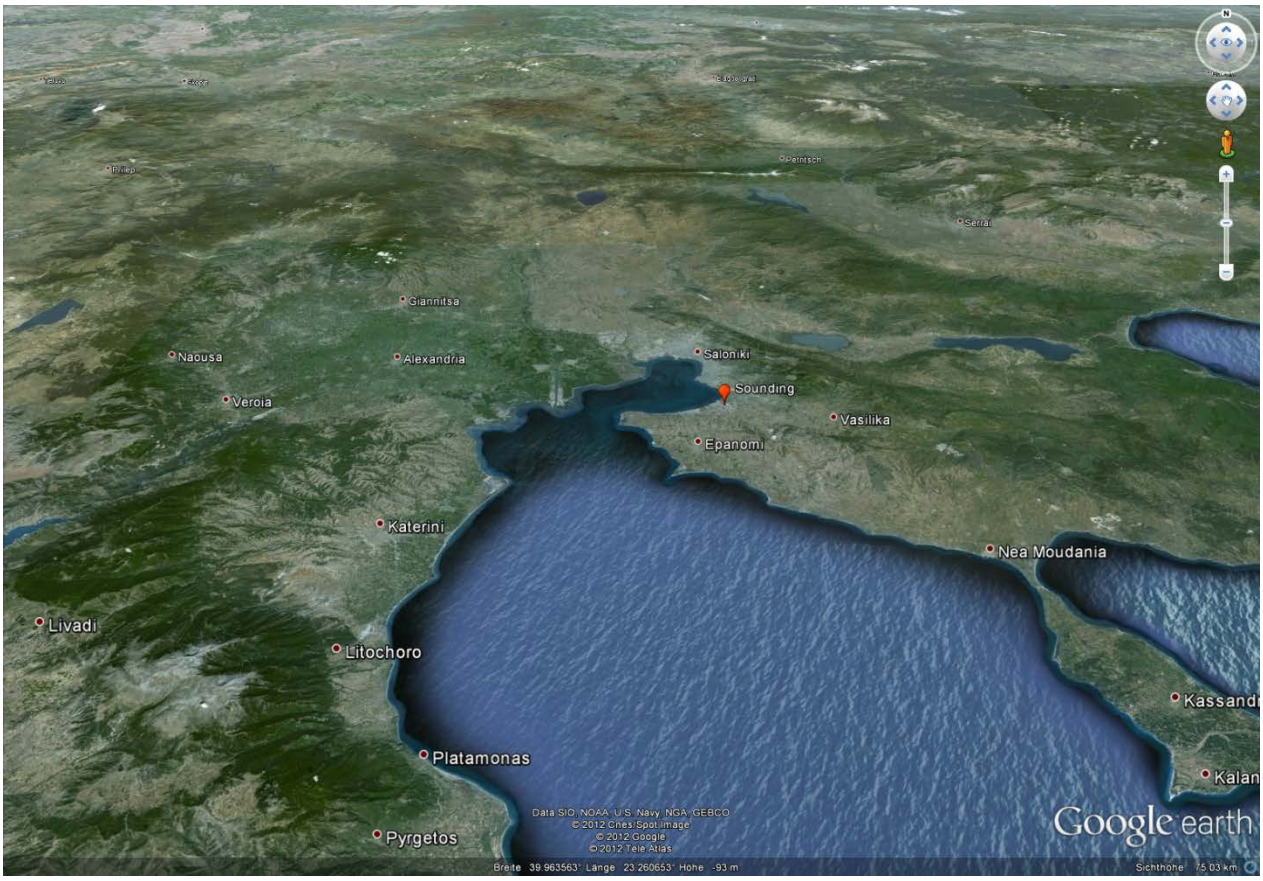

Figure 62: The test site Thessaloniki airport for the inter comparison of sounding and NWP profiles is highlighted in red.

The sounding data are available daily at midnight and at noontime. This is the reason, the NWP is performed for this particular time instead of the time of the SAR acquisition. In this report the noontime is chosen. Because of the sun illumination, the test case is more realistic and difficult for two reasons. First, the temperature is higher and consequently the refractivity is more severe. Second, the troposphere turbulence is increased as well.

Figure 63 provides an example for the comparison of temperature of the NWP and the measured vertical atmosphere profile by sounding. Two different effects can be immediately noticed which affect the precision of the refractivity estimation and are visualized in Figure 64. First, atmospheric temperature measured by sounding (blue graph) has more variation (turbulence) near the ground compared to the predicted from NWP (green graph) which is rather smooth. The dots in the graphs indicate the given measurement points. In this example, the green dots could follow the turbulent temperature profile of the sounding. Consequently, the too smooth characteristic of the NWP is not an effect of vertical under-sampling of the vertical profile. Second, the NWP data close to the ground are missing. It is a consequence of the coarse DEM in the NWP. An extrapolation (e.g. linear or nearest neighbour) introduces noticeable errors in the input parameters which propagate into the final refractivity estimation.

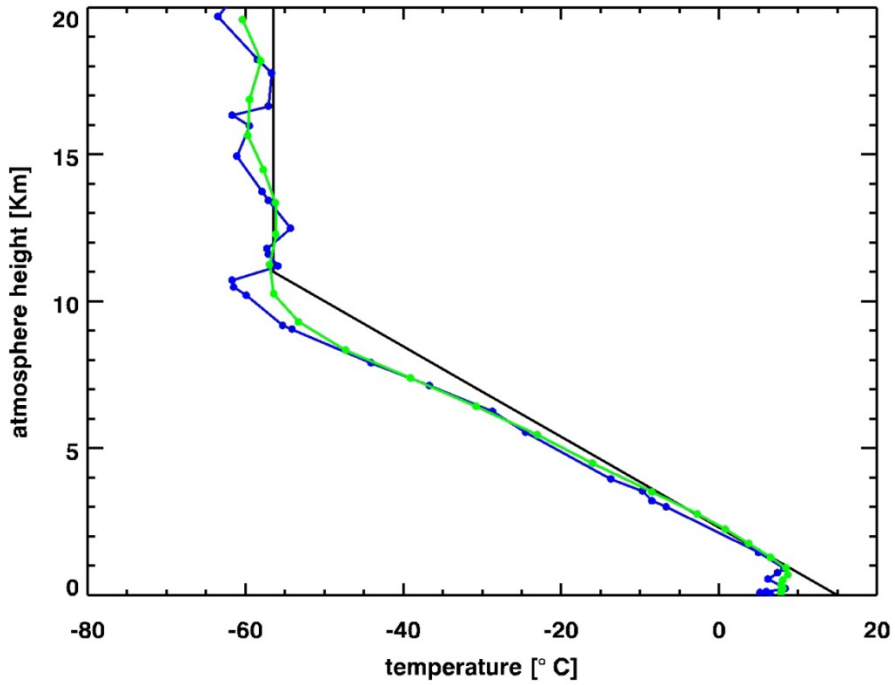

Figure 63: atmospheric temperature measured by sounding (blue) and predicted from NWP (green) over the test site Thessaloniki (31. December 1996 12:00) Black: standard atmosphere temperature.

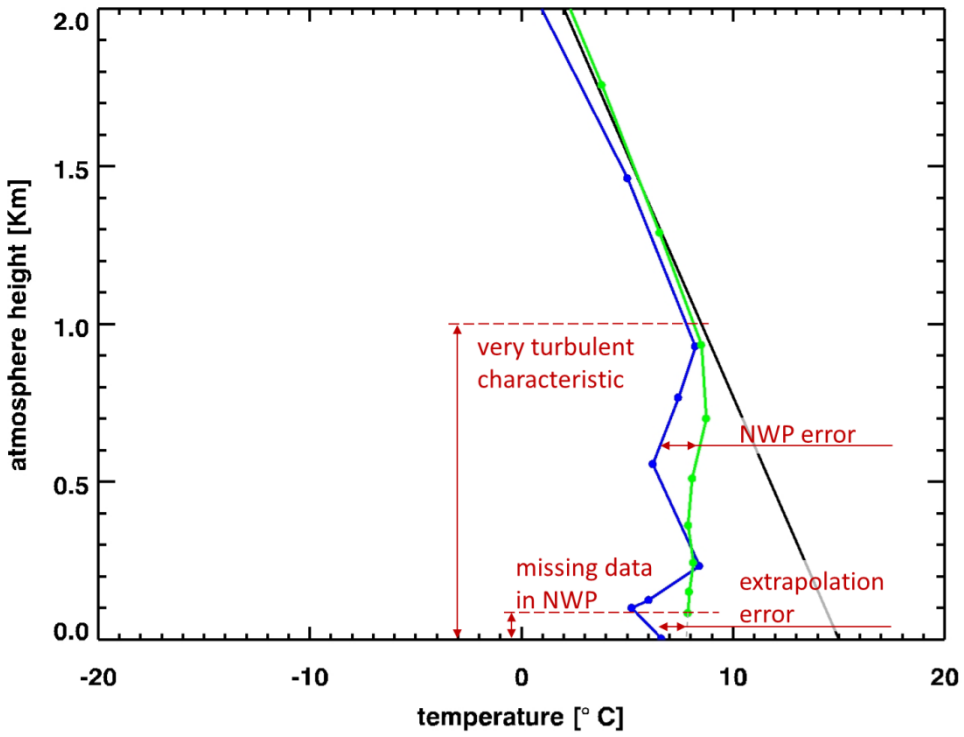

Figure 64: effects in the NWP temperature prediction affecting the precision of the refractivity estimation.

The following inter-comparison of NWP and sounding data is based on the given and straight forward nadir geometry i.e. on the pure vertical profile. Practically, it provides the absolute deviation of temperature, total pressure and water vapour mixing ratio as a sample from the typical error distribution and also illustrates the typical vertical regions with the respective different hindcast accuracies. The root-mean-square deviation (RMSD)

$$RMSD = \sqrt{\frac{\sum_{i=1}^{N} \left(x_{sounding}[i] - x_{wrf}[i] \right)^2}{N}} \qquad (60)$$

is a suitable measure of the differences between the measured and hindcast values. In contrast to the standard deviation, it includes the actual bias between the two data sets and is finally used as an estimate of the expected standard deviation. Table 6 summarizes the WRF accuracy values which can be generally taken for the error propagation. Examples for the respective parameters follow in the subsequent sub-sections. These examples finally confirm the incredible accuracy of WRF hindcast for temperature and pressure to be better than one percent in the relative error.

Table 6: expected standard deviations of the WRF output parameters

	0-3 km	3-10 km	10-20 km
std. dev. of pressure [hPa]	3.0	3.0	1.0
std. dev. of abs. temperature [K]	2.0	1.0	1.5
std. dev. of vapour mixing ratio [g/Kg]	1.5	0.5	0.0

8.2.3.1 TEMPERATURE EXAMPLE

Figure 65 visualizes the two independent atmospheric temperature profiles measured by the sounding and predicted by the NWP. Obviously, the vertical spatial NWP is smoother compared to sounding. From the absolute error in Figure 66, the expected standard deviation of the temperature error can be estimated. The visualised examples represent two samples from the ensemble of typical hindcasts. This is the reason, the RMSDs of the examples are taken as samples for the WRF temperature standard deviation and finally as a rough approximation of the expected WRF accuracy throughout of this assessment. For completeness, the relative error of the temperature profile is provided in Figure 67. This figure also makes the different regions of accuracy visible. In these examples, the planetary boundary layer has a height of approximately four kilometres. Another region is above ten kilometres. Both regions are indicated in the figures by dashed grey lines.

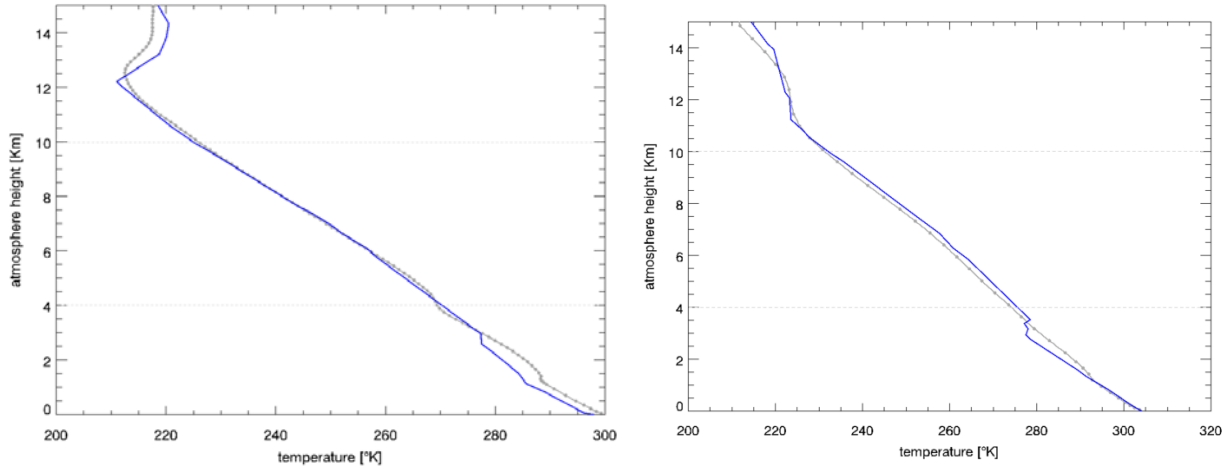

Figure 65: atmospheric temperature measured by sounding (blue) and predicted from NWP (grey) over the test site Thessaloniki. left: 6. June 1992 at 12:00 and right: 27. July 1997 at 12:00.

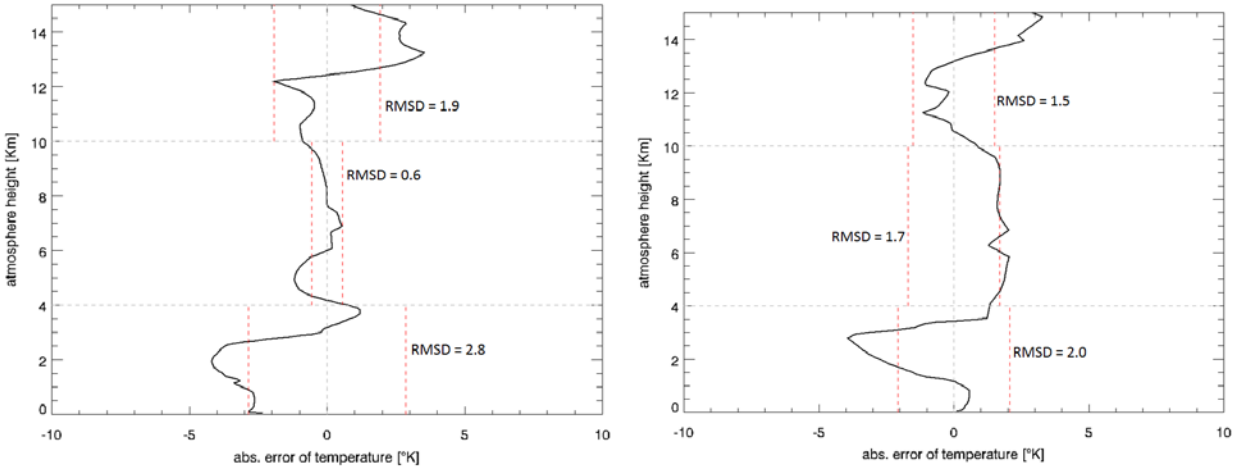

Figure 66: absolute error of temperature for the test site Thessaloniki. left: 6. June 1992 at 12:00 and right: 27. July 1997 at 12:00. Red dashed lines represent the expected absolute standard deviation of temperature in °K characteristic for the WRF hindcast.

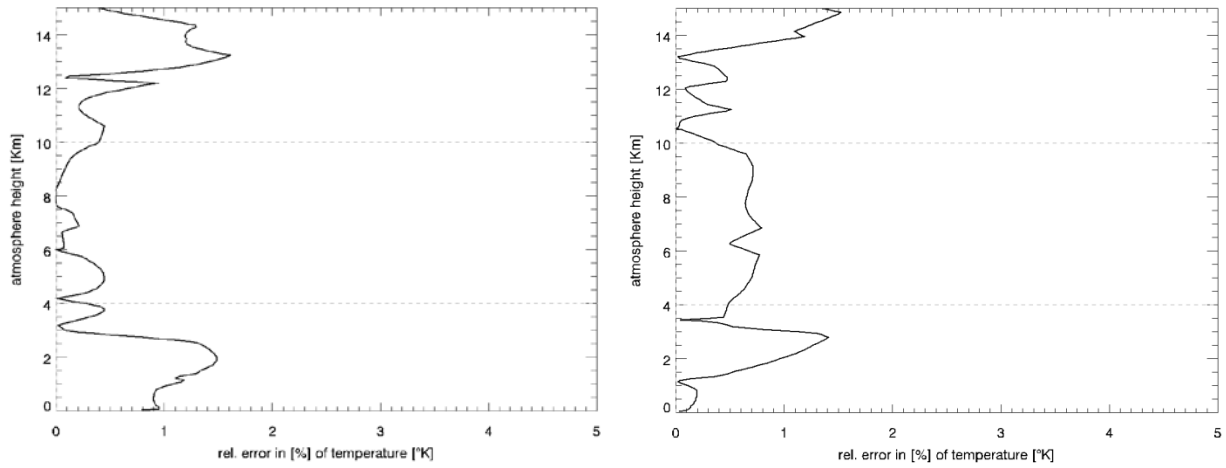

Figure 67: relative error in % of temperature for the test site Thessaloniki. left: 6. June 1992 at 12:00 and right: 27. July 1997 at 12:00.

8.2.3.2 TOTAL PRESSURE EXAMPLE

Figure 68 visualizes the two independent atmospheric total pressure profiles measured by the sounding and predicted by the NWP. Because of the smooth characteristic of this parameter, both signals have only a very small deviation. The respective absolute deviations are plotted in Figure 69 and the relative hindcast error in Figure 70.

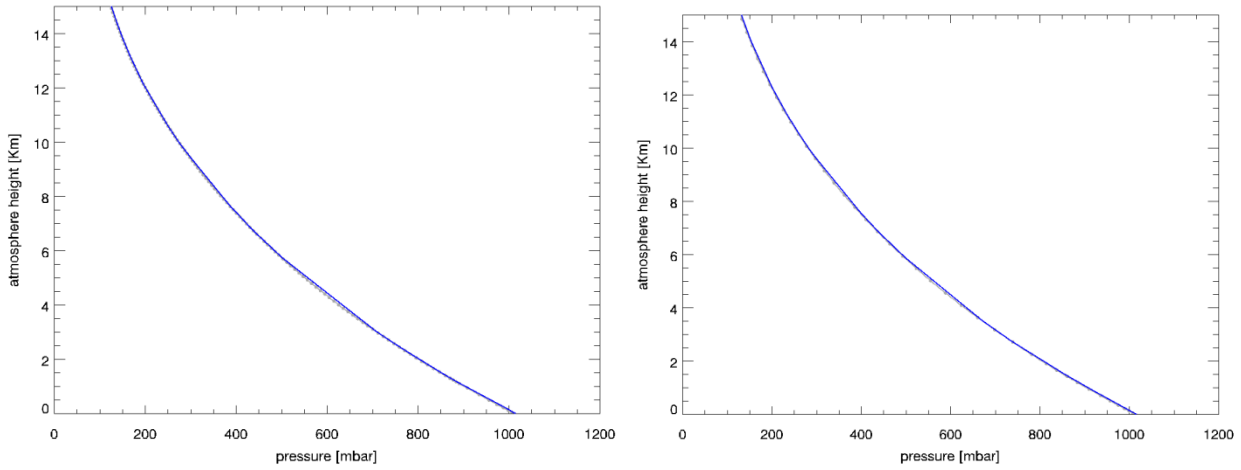

Figure 68: atmospheric total pressure measured by sounding (blue) and predicted from NWP (grey) for the test site Thessaloniki. left: 6. June 1992 at 12:00 and right: 27. July 1997 at 12:00.

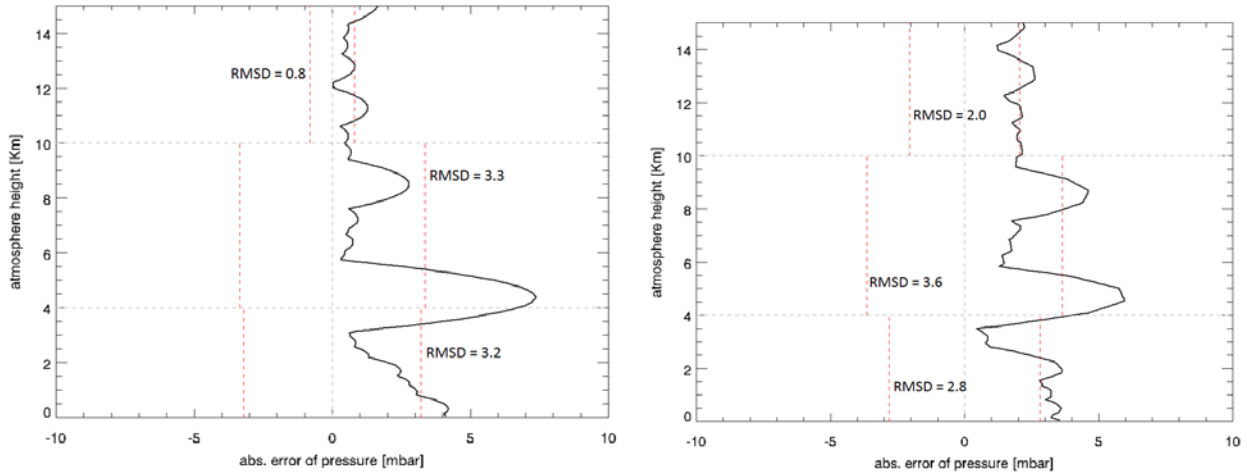

Figure 69: absolute error of the atmospheric total pressure for the test site Thessaloniki. left: 6. June 1992 at 12:00 and right: 27. July 1997 at 12:00. Red dashed lines represent the expected standard deviation of pressure in hPa characteristic for the WRF hindcast.

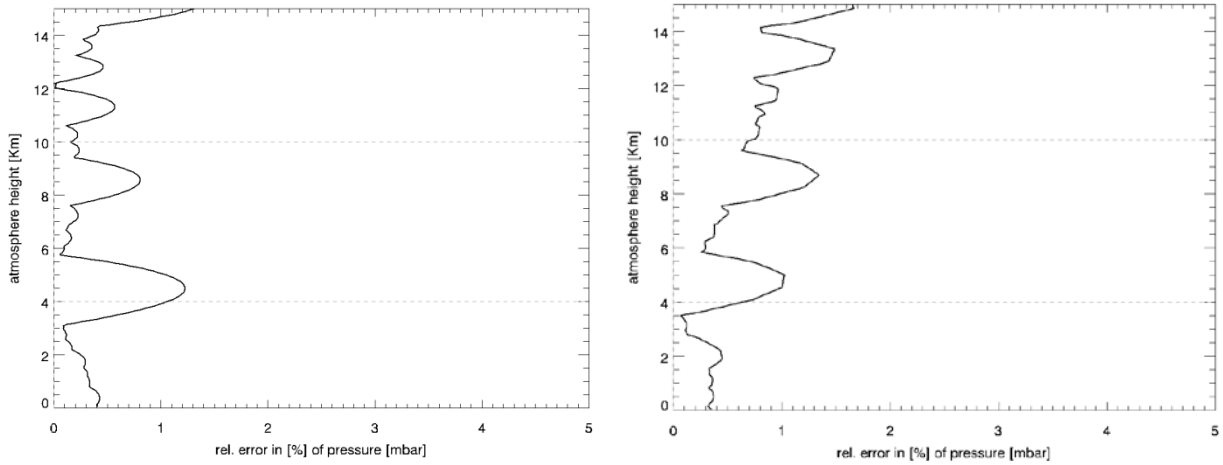

Figure 70: relative error in % of the atmospheric total pressure for the test site Thessaloniki. left: 6. June 1992 at 12:00 and right: 27. July 1997 at 12:00.

8.2.3.3 WATER VAPOUR MIXING RATIO EXAMPLE

Figure 71 visualizes the two independent atmospheric water vapour mixing ratio profiles measured by the sounding and predicted by the NWP. The sounding indicates abrupt changes in the water vapour mixing ratio corresponding to different atmospheric layers. In contrast, the WRF hindcast provides smooth variations of this parameter over height. However, it indeed follows in mean the real water vapour. Most of the water vapour is collected close to the ground in the planetary boundary layer. Above an altitude of eight kilometres, the water vapour mixing ratio can be assumed to be zero. The plot of the relative error is skipped - it does not support this assessment.

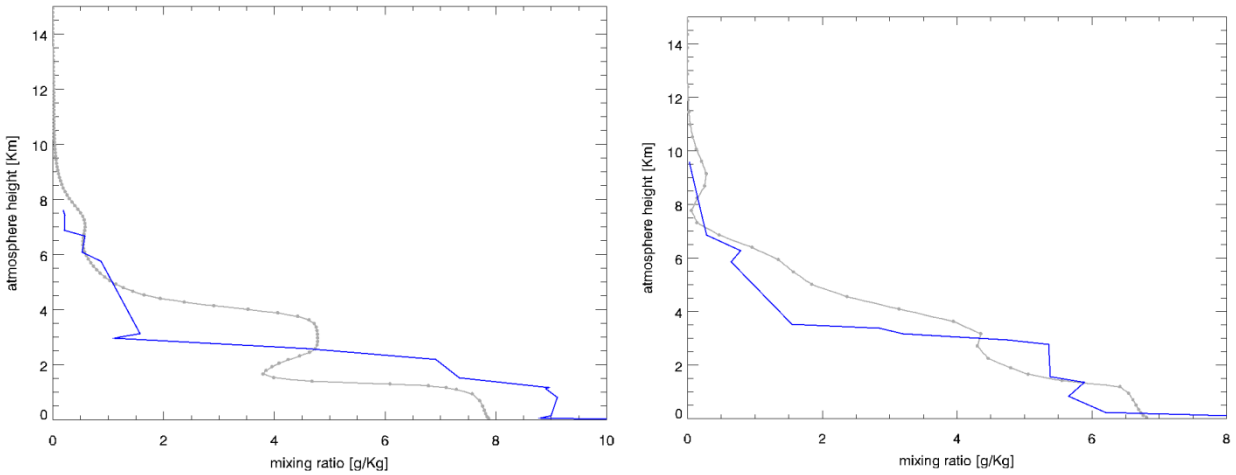

Figure 71: atmospheric total water vapour mixing ratio measured by sounding (blue) and predicted from NWP (red) for the test site Thessaloniki (6. June 1992 at 12:00).

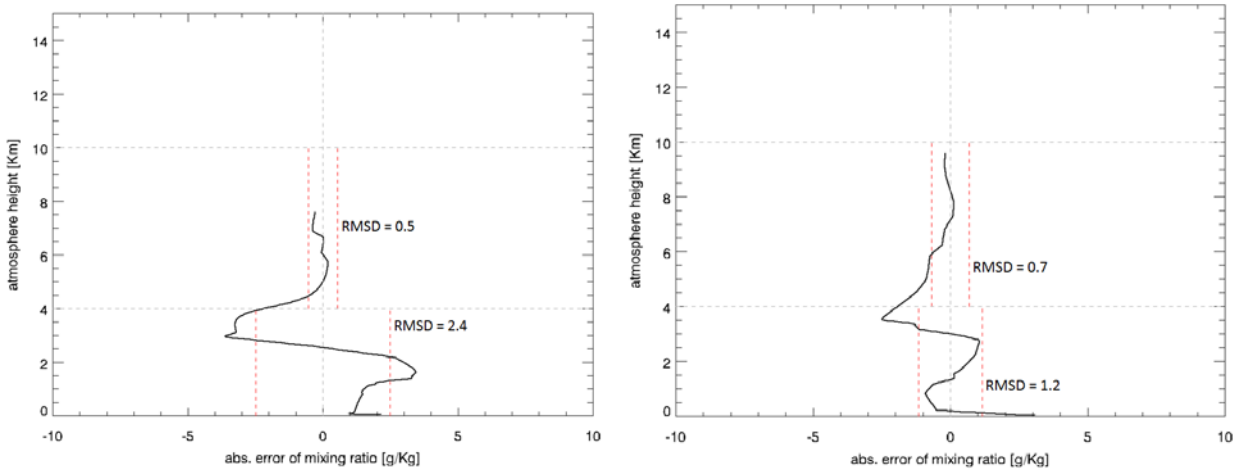

Figure 72: absolute error of water vapour mixing ratio for the test site Thessaloniki (6. June 1992 at 12:00).

8.3 PRACTICAL RESULTS FROM THE NWP METHOD

For the mitigation of troposphere effects, an operational processor named *Troposphere Effect Mitigation Processor* (TEMP) has been developed i.e. practically for the three dimensional refractivity estimation. It is based on numerical weather prediction (NWP) using the WRF software system. The hindcast is performed for each radar acquisition and for the closest full minute related to the acquisition time and actually with a resolution of 2 km. The inclusion of the full SAR observation geometry and the integration along the line of sight (LOS) using the precise scatterer height allow to compensate for topography dependent troposphere effects. Figure 73 visualizes the implemented principle for the mitigation of the stratification effect using NWP. The NCEP Climate Forecast System Reanalysis (CFSR) is the independent (from InSAR) input data set. It provides the

atmosphere state 6-hourly for a time span from January 1979 to December 2010 with about 30 x 30 km spatial sampling.

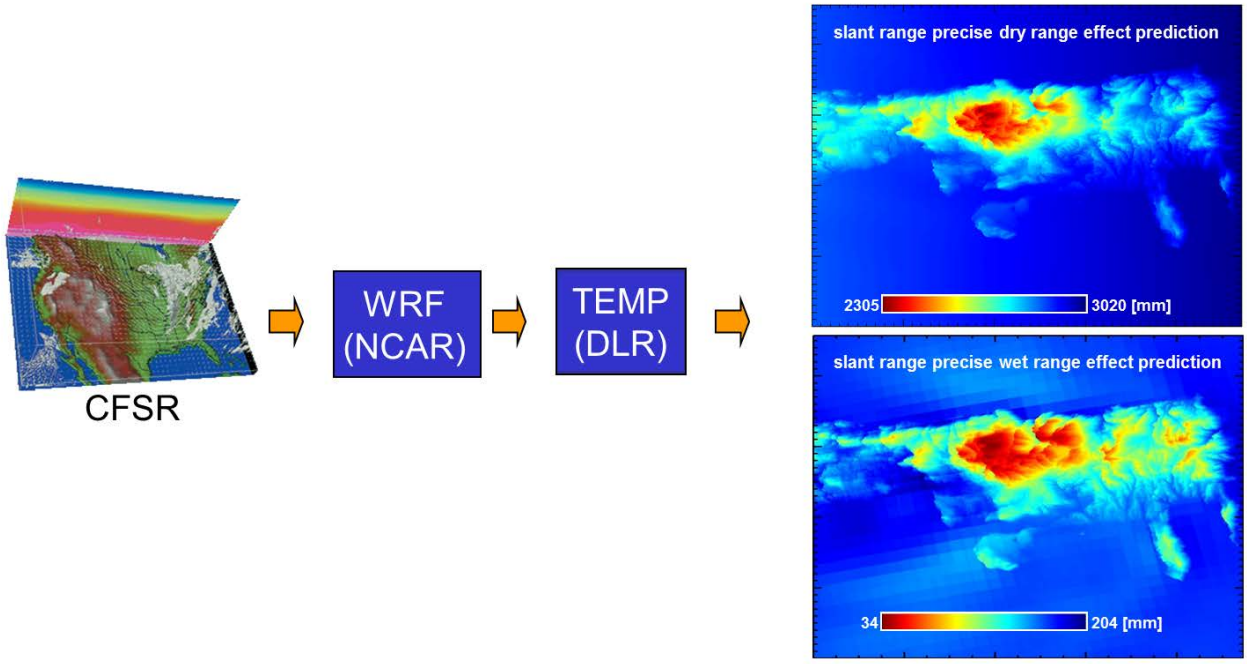

Figure 73: implemented principle for the mitigation of the stratification effect using NWP. TEMP is the abbreviation for the newly developed *Troposphere Effect Mitigation Processor.*

The implementation of the LOS algorithm presented in section 8.1.2 is ongoing. This is the reason, the current algorithm results are presented and this report will be updated as soon as new processing results are available. In the actual implementation, the processor (TEMP) estimates the wet and the dry delay for each scene according to algorithm 3 on page 42 i.e. using the numeric integration for the delay estimates in a radar acquisition. These delay estimates are combined according to the interferometric pairs. In the next step, the height dependence of this phase is estimated and finally modelled by a third order polynomial. As a result, the estimated atmosphere effect phase (black graph) and the modelled atmosphere effect phase (green graph) are obtained. Both are visualized exemplarily in Figure 74. This figure also proves the third order model to be sufficient for an approximation of the effect. The atmosphere stratification phase φ_{tropo} [rad] depending on the height h [m] is consequently fitted by:

$$\varphi_{tropo} = \varphi_0 + \varphi_1 \cdot h + \varphi_2 \cdot h^2 + \varphi_3 \cdot h^3 \qquad (61)$$

As a result, the PSI phase correction depends on the actual height of a scatterer and not just on the height difference of a scatterer pair. Also, the processing makes these correction values for each detected scatterer available (independent of its quality and height).

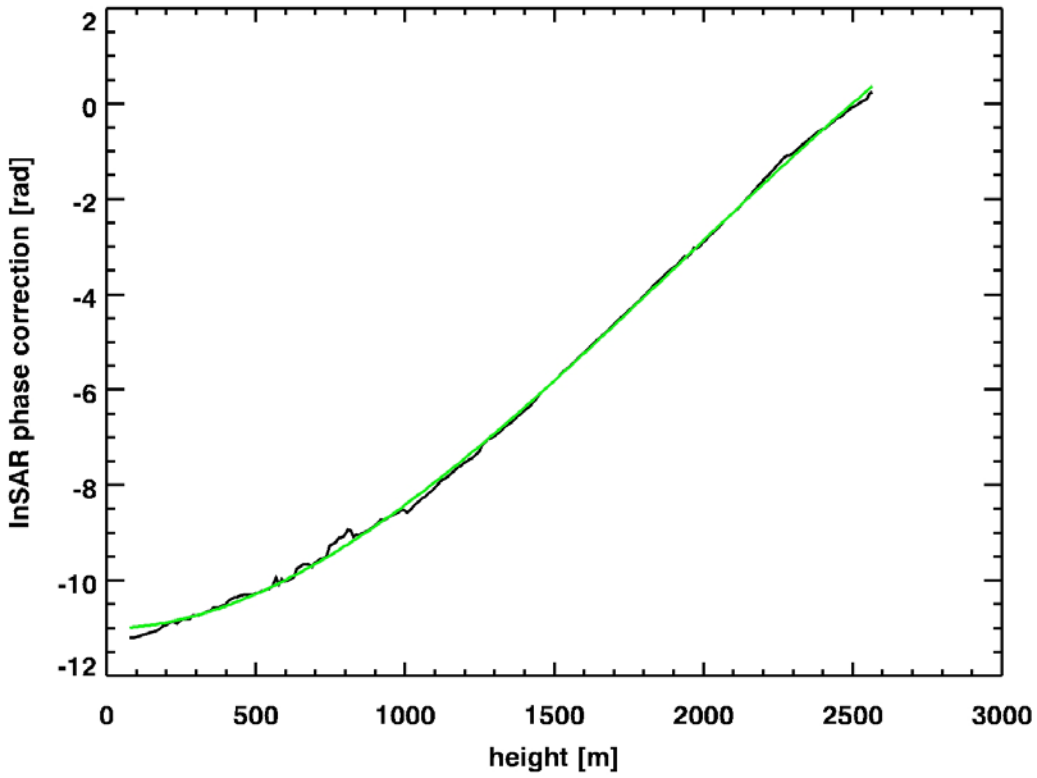

Figure 74: black line: estimated atmosphere effect from NWP; green line: third order modelled dependency of the interferometric correction phase with respect to height; This estimate can be obtained for each persistent scatterer in a test site.

In the following, the test cases for the direct estimation from section 6 are also used to demonstrate the performance and the applicability of this newly developed method. The results are summarized in Table 7 and can be compared with Table 1. To begin with, the results for the selected interferograms are reported in groups of three figures for each test case. The first figure visualizes the estimated atmosphere effect from NWP by a black line and the corresponding third order modelled dependency of the interferometric correction phase with respect to height by a green line. The second figure provides the interferometric phase of the modelled atmosphere effect obtained from NWP for the respective overall interferogram. Subtracting this phase from the original interferogram should mitigate the atmosphere effect and remove the residual fringes in the newly generated interferogram. In order to visualize this improvement, the third figure shows the uncorrected interferogram including the stratification effect on the left hand side and the atmosphere corrected interferogram on the right hand side.

Table 7: Estimates of the atmosphere correction for the test cases

slave orbit	φ_0	φ_1	φ_2	φ_3
11155	-10.144800	0.0011808756	1.8668459e-06	-2.8932336e-10
12658	-5.6314136	0.00053734654	2.9365606e-06	-8.0750712e-10
17668	-17.586678	0.0060414425	6.0344208e-07	-2.5617154e-10
24682	6.7161189	0.00048464523	-2.6960944e-07	1.9194963e-11

The test case of the interferogram with the slave 11155 is visualized in the following Figure 75, Figure 76 and Figure 77. Over the height range of 2500 m the atmosphere effect is about 10 rad (visible in the first figure). This strong effect is a result of the combination of a winter and a summer scene.

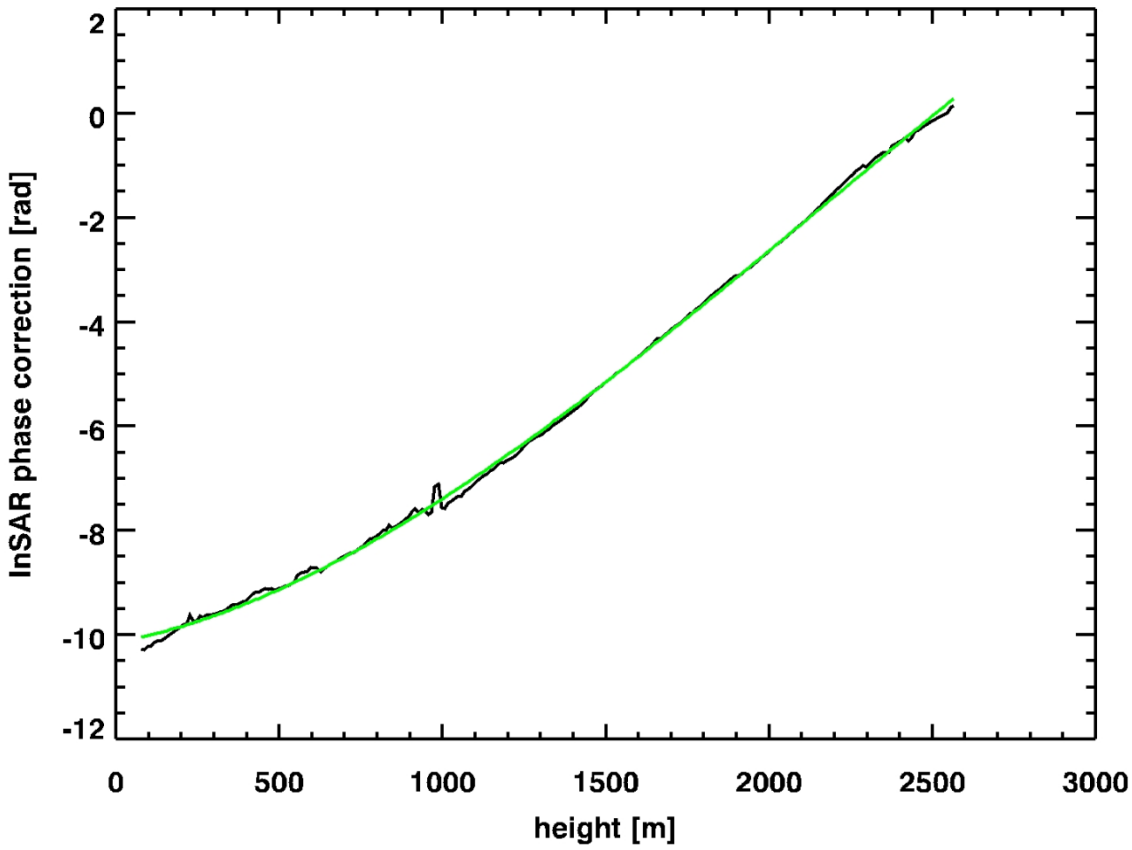

Figure 75: test case interferogram 11155 (winter - summer): black line: estimated atmosphere effect from NWP; green line: third order modelled dependency of the interferometric correction phase with respect to height

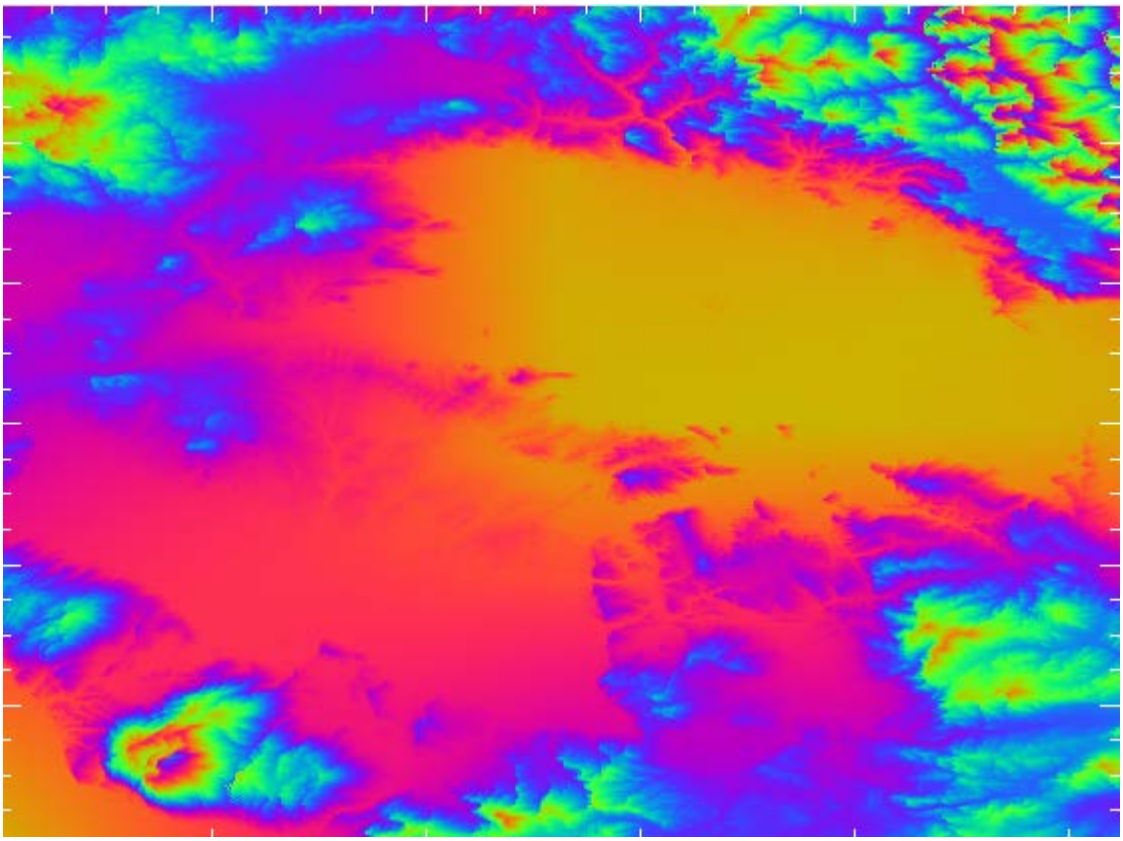

Figure 76: test case interferogram 11155: phase of the modelled atmosphere effect obtained from NWP (Figure 75)

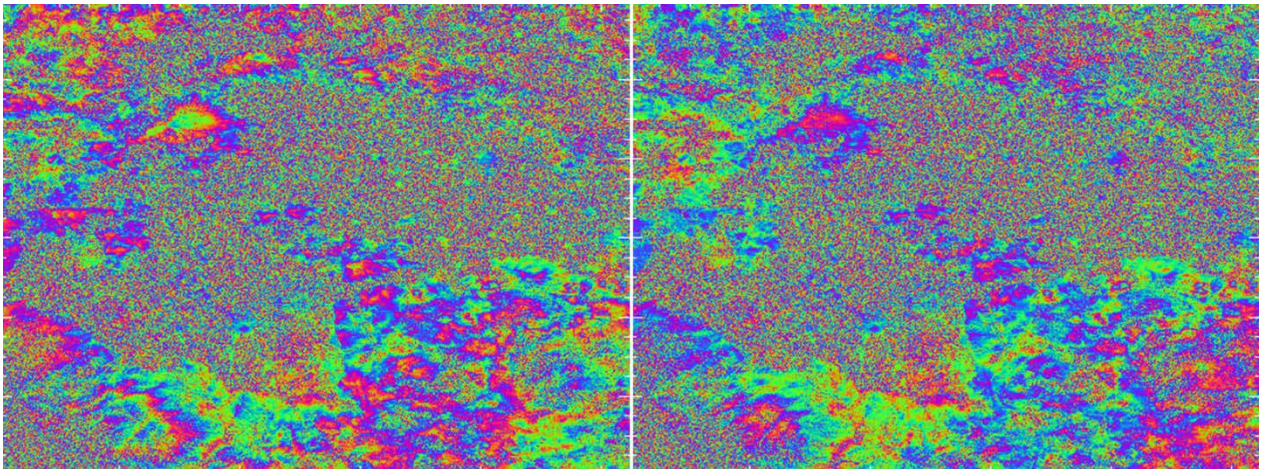

Figure 77: left: summer – winter interferogram (11155) with vertical stratification effect; right: stratification corrected interferogram using estimated atmosphere phase visualized in Figure 76

The test case of the interferogram with the slave 112658 is visualized in the following Figure 78, Figure 79 and Figure 80. Over the height range of 2500 m the atmosphere effect is about 7 rad (visible in the first figure). This strong effect is a result of the combination of a winter and a late summer scene. However, the effect is reduced compared to the pure winter – summer combination from example with scene 11155.

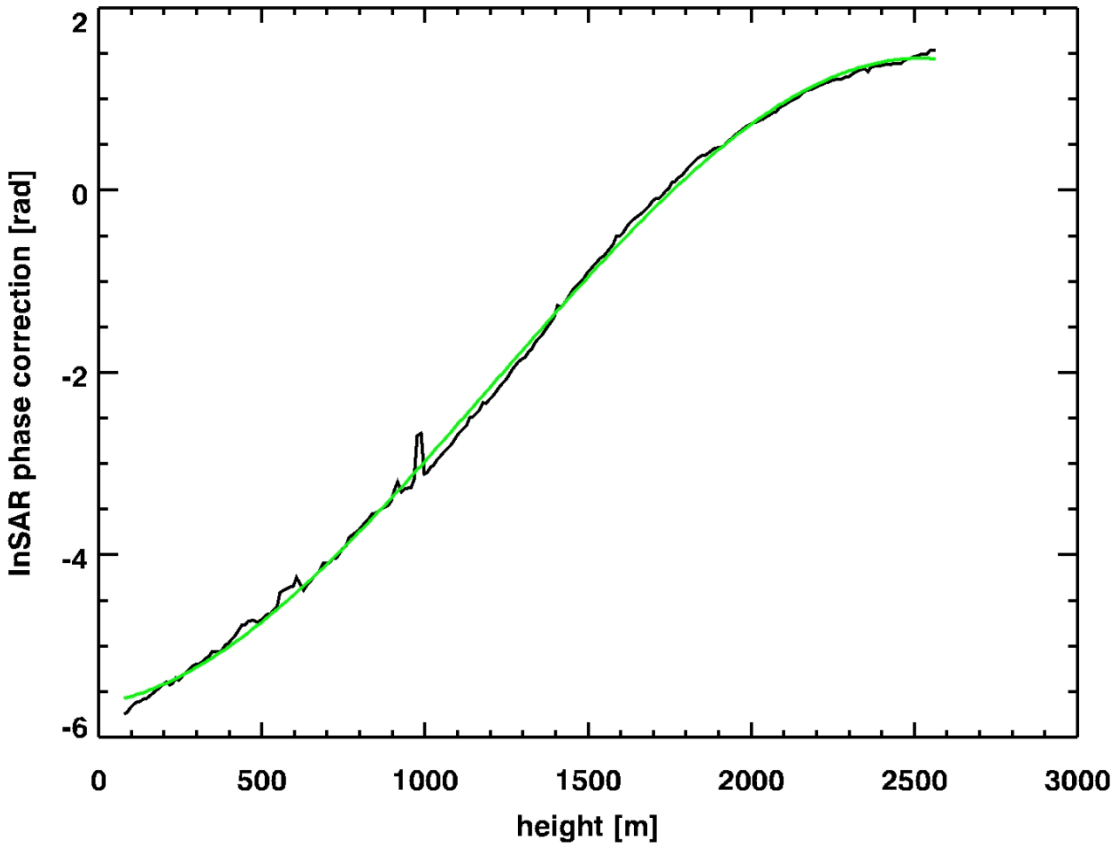

Figure 78: test case interferogram 12658 (winter – late summer): black line: estimated atmosphere effect from NWP; green line: third order modelled dependency of the interferometric correction phase with respect to height

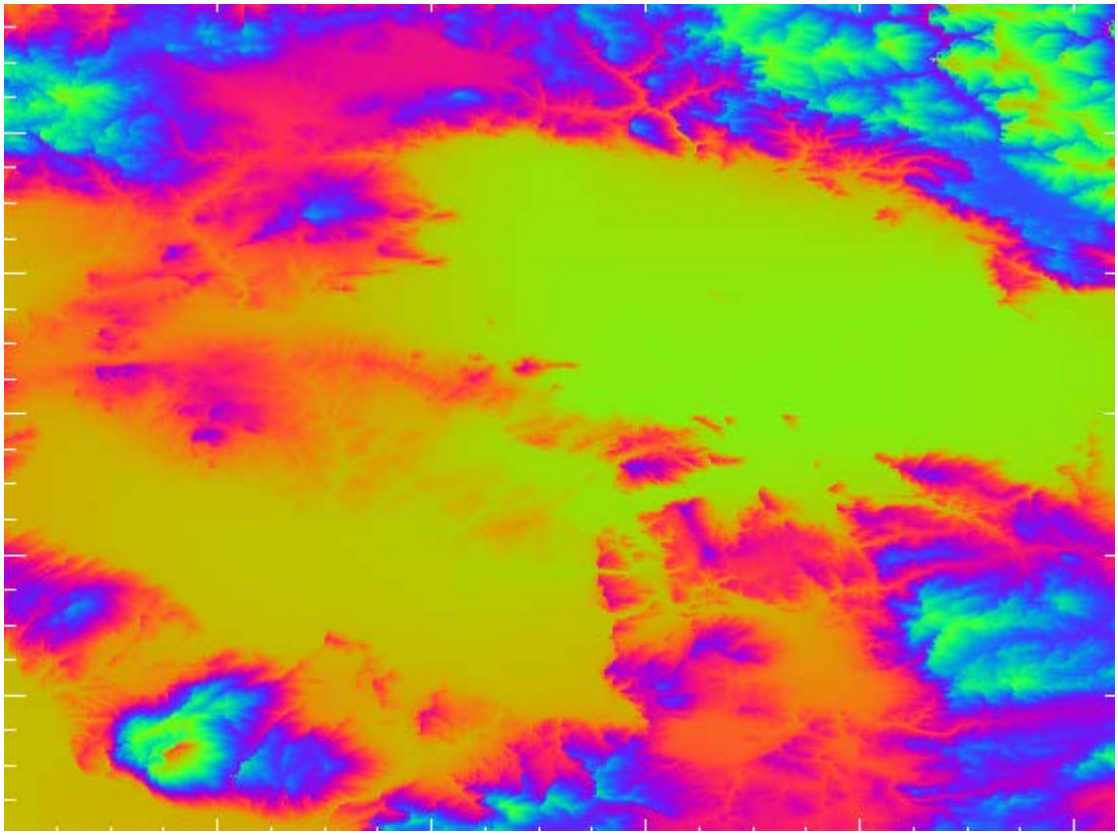

Figure 79: test case interferogram 12658: phase of the modelled atmosphere effect obtained from NWP (Figure 78)

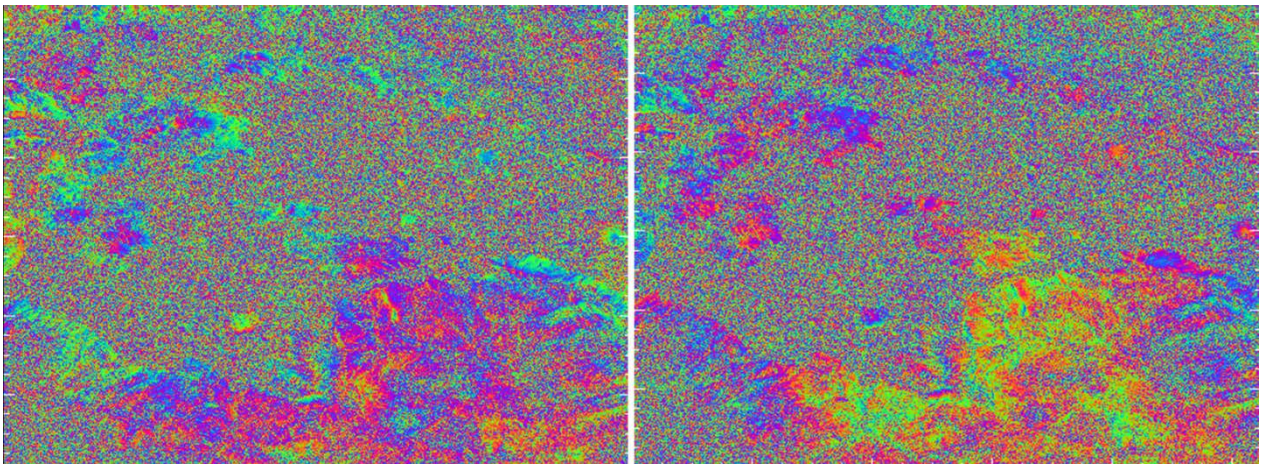

Figure 80: left: winter – late summer interferogram (12658) with vertical stratification effect; right: stratification corrected interferogram using estimated atmosphere phase visualized in Figure 79

The test case of the interferogram with the slave 17668 is visualized in the following Figure 78, Figure 79 and Figure 80. In this example, the height range of 2500 m results in an atmosphere effect of more than 10 rad (visible in the first figure). Again, this strong effect is a result of the combination of a winter and a summer scene.

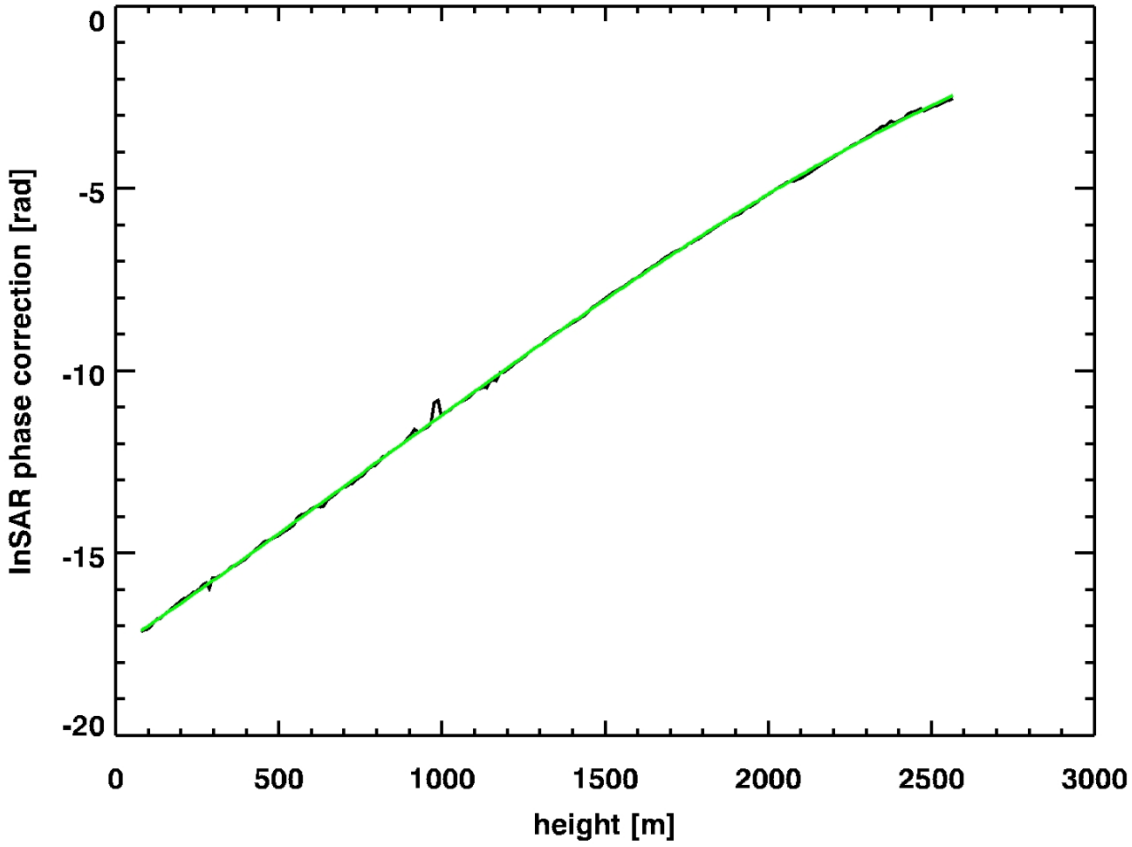

Figure 81: test case interferogram 17668 (winter - summer): black line: estimated atmosphere effect from NWP; green line: third order modelled dependency of the interferometric correction phase with respect to height

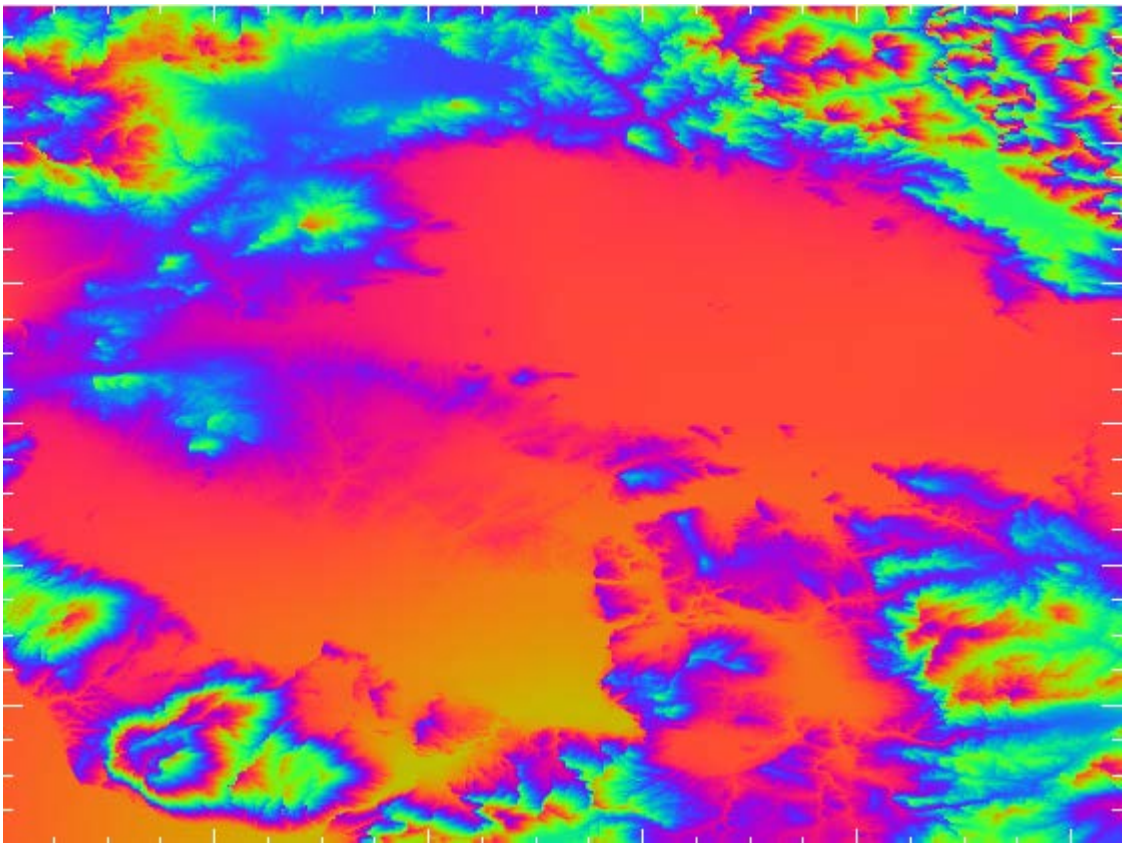

Figure 82: test case interferogram 17668: phase of the modelled atmosphere effect obtained from NWP (Figure 81)

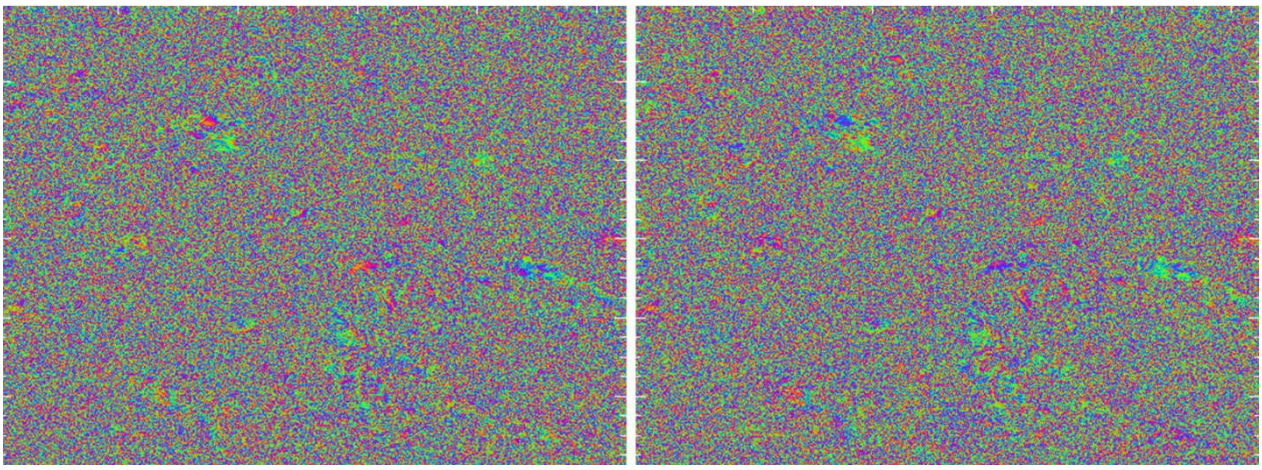

Figure 83: left: winter – summer interferogram (17668) with vertical stratification effect; right: stratification corrected interferogram using estimated atmosphere phase visualized in Figure 82

The test case of the interferogram with the slave 24682 is visualized in the following Figure 84, Figure 85 and Figure 86. In this example, the height range of 2500 m results in a very small atmosphere effect of less than 1 rad (visible in the first figure). Of course, this little effect is a result of the combination of a winter and another winter scene.

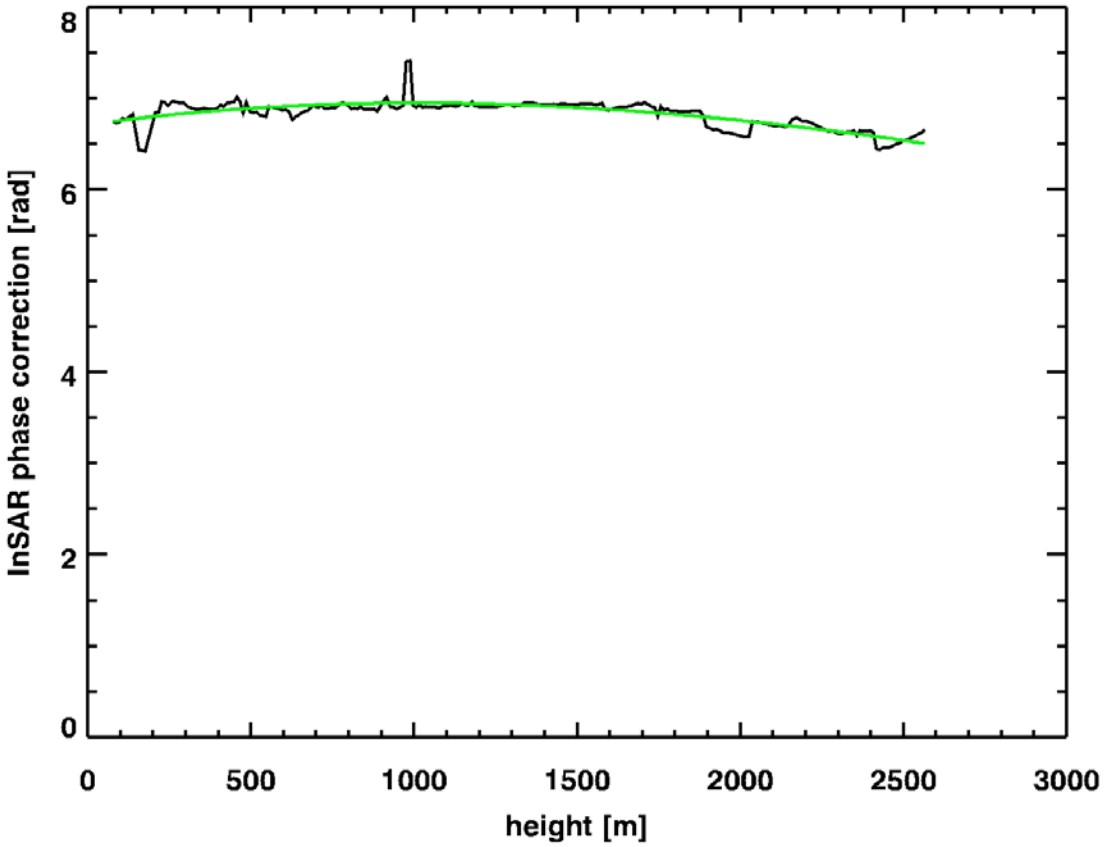

Figure 84: test case interferogram 24682 (winter - winter): black line: estimated atmosphere effect from NWP; green line: third order modelled dependency of the interferometric correction phase with respect to height

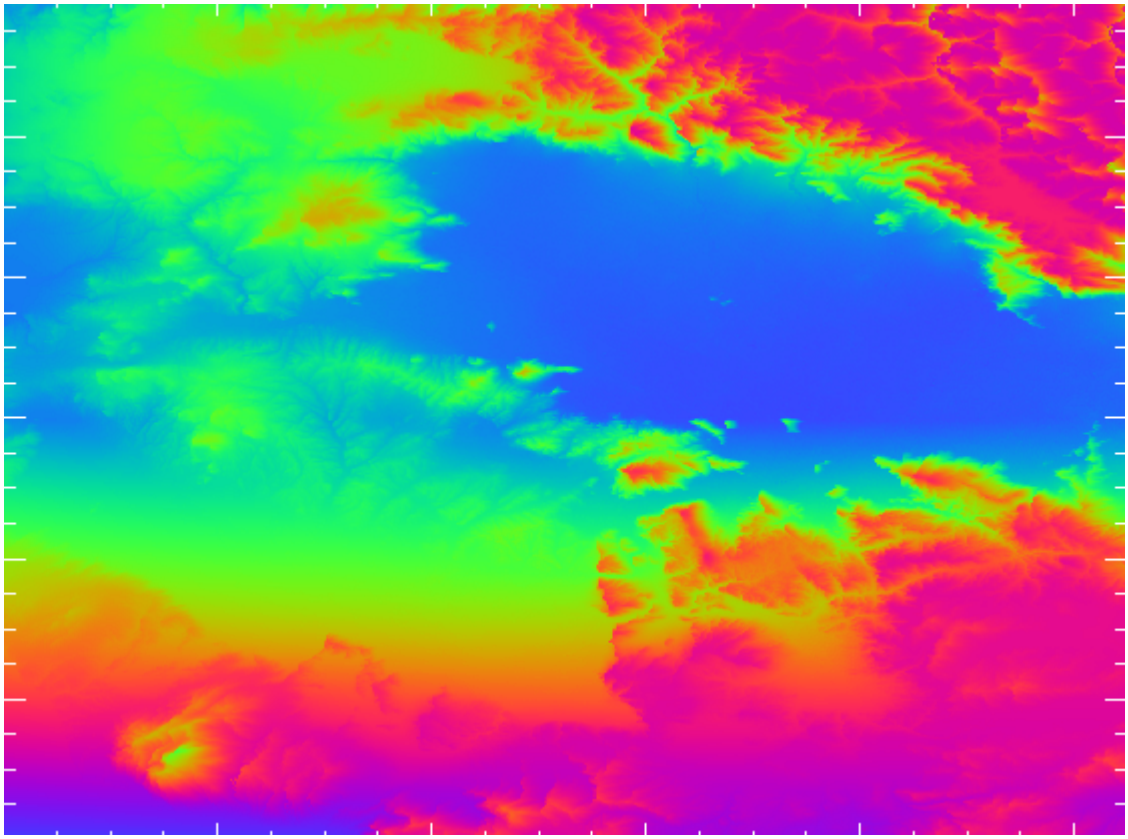

Figure 85: test case interferogram 24682: phase of the modelled atmosphere effect obtained from NWP (Figure 84)

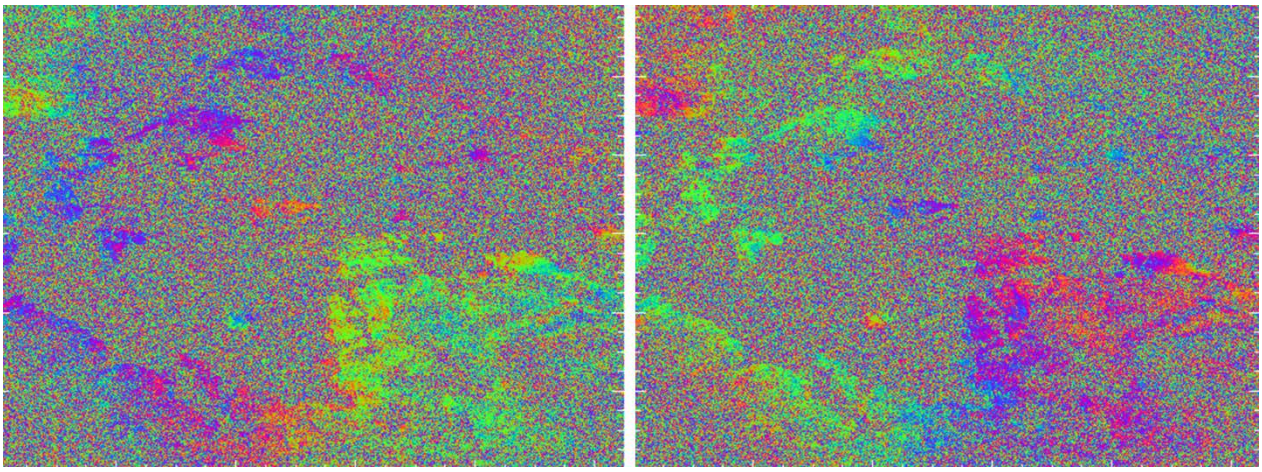

Figure 86: left: winter – winter interferogram (24682) with little vertical stratification effect; right: stratification corrected interferogram using estimated atmosphere phase visualized in

As mentioned before, this NWP based correction method is independent from the coherence of the interferometric input data. This is the reason, the complete time series can be corrected with the estimated data directly. Examples for the atmosphere correction signal are shown in Figure 87, Figure 88, Figure 89 and Figure 90 for some randomly selected PS pairs. These figures visualize in the right part a small mountainous area of the Larissa test site. The background is the radar brightness, the points are detected persistent scatterers and their colour corresponds to their respective topography height. The left plot in these figures visualizes the estimated atmosphere correction signal for the persistent scatterers connected by the white arrow in the right image. Table 8 summarizes the parameters of these PSI examples. Clearly, the gain in coherence increases with the height difference between the scatterers.

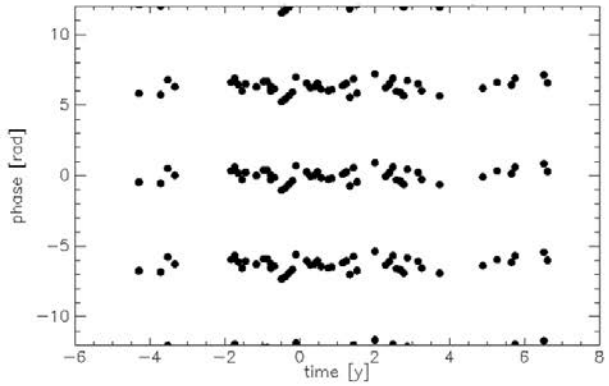

$h_{PS1} = 583\ m$
$h_{PS2} = 395\ m$
$dist_{PS\,1-2} = 1420\ m$
$\gamma_{gain} = 0.1$

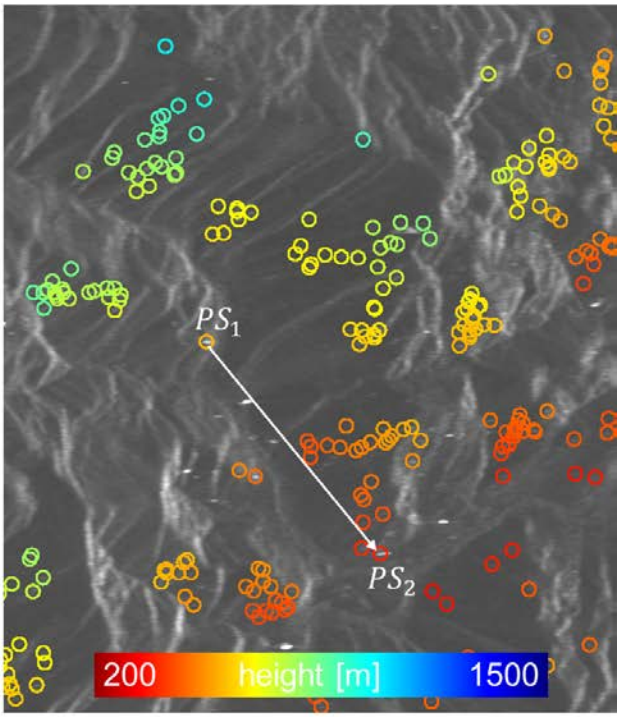

Figure 87: PSI example 1 with a height difference of 188 m between the scatterers. The gain in coherence by the atmosphere compensation (upper left phase) is 0.1.

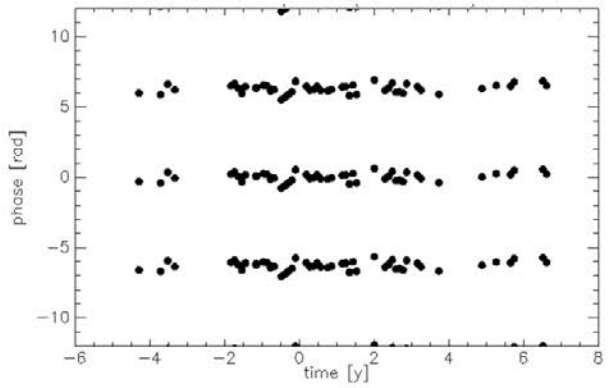

$h_{PS1} = 714\ m$
$h_{PS2} = 583\ m$
$dist_{PS\,1-2} = 502\ m$
$\gamma_{gain} = 0.05$

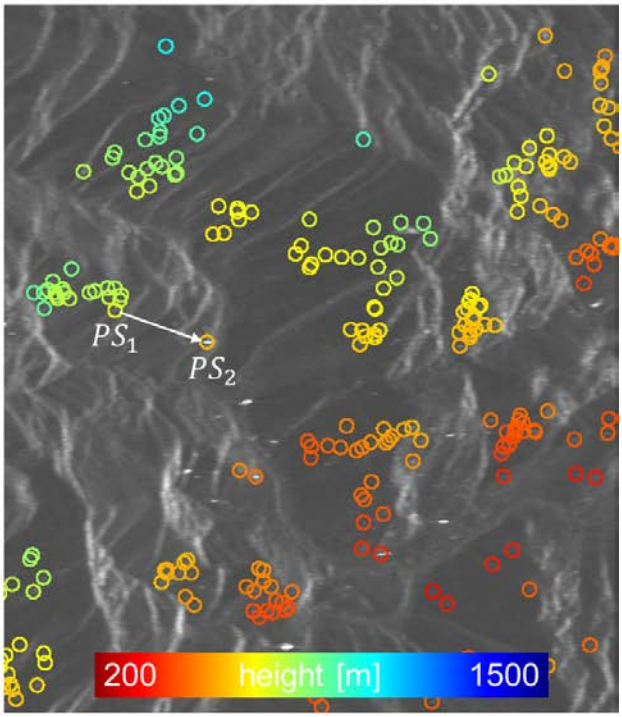

Figure 88: PSI example 2 with a height difference of 131 m between the scatterers. The gain in coherence by the atmosphere compensation (upper left phase) is 0.1.

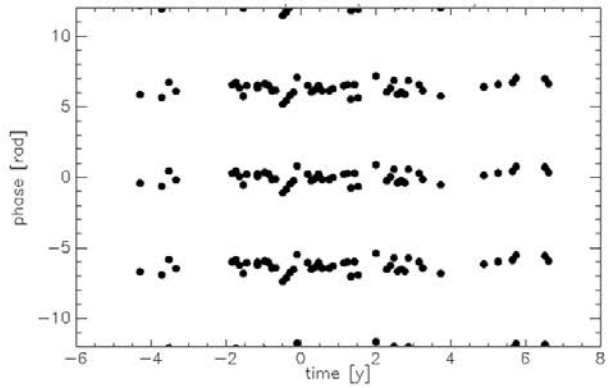

$h_{PS1} = 904\ m$
$h_{PS2} = 717\ m$
$dist_{PS\,1-2} = 500\ m$
$\gamma_{gain} = 0.1$

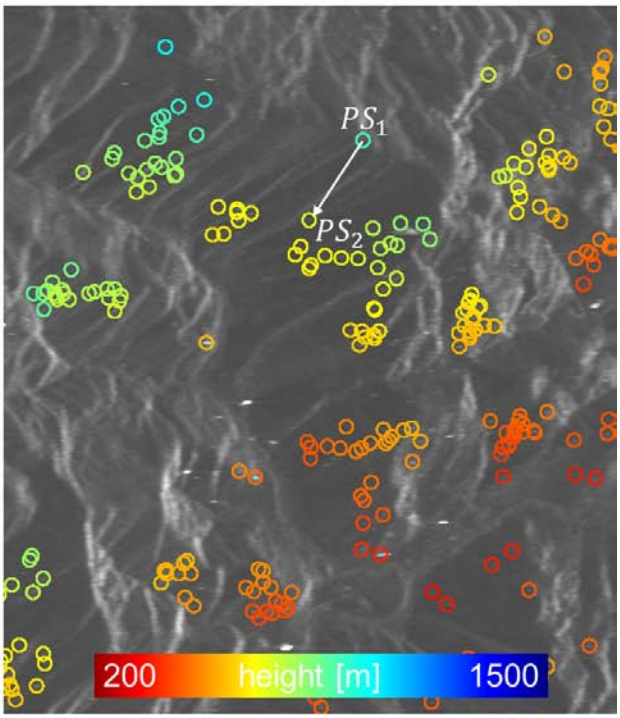

Figure 89: PSI example 3 with a height difference of 187 m between the scatterers. The gain in coherence by the atmosphere compensation (upper left phase) is 0.1.

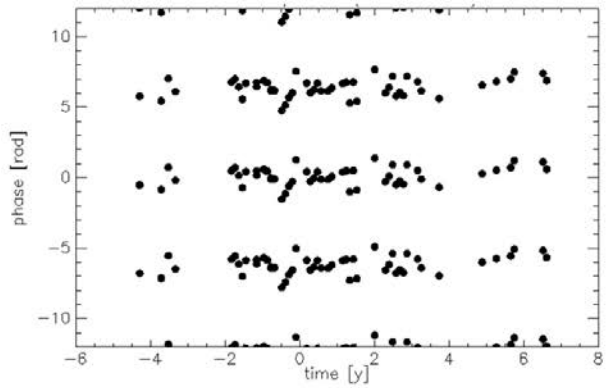

$h_{PS1} = 965\ m$
$h_{PS2} = 693\ m$
$dist_{PS\ 1-2} = 560\ m$
$\gamma_{gain} = 0.19$

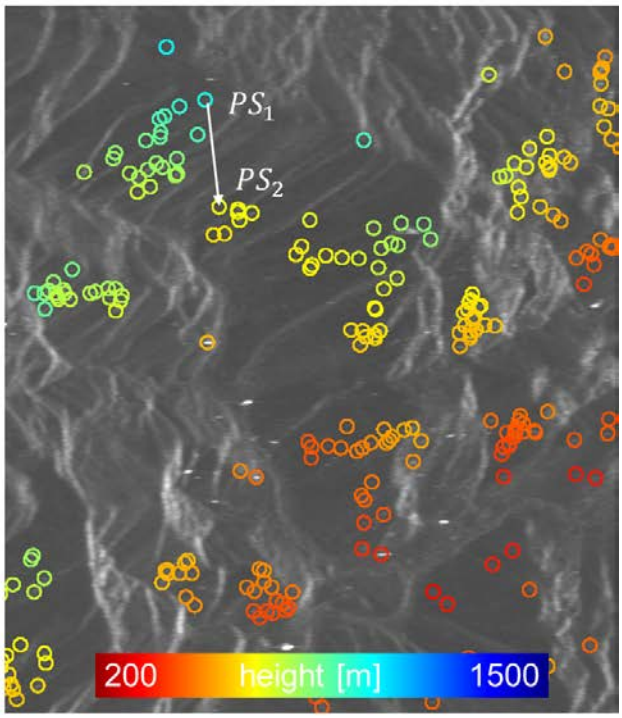

Figure 90: PSI example 4 with a height difference of 272 m between the scatterers. The gain in coherence by the atmosphere compensation (upper left phase) is 0.19.

Table 8: experimentally measured parameters of PSI examples

example	distance	height difference	coherence gain
1	1420 m	188 m	0.1
2	502 m	131 m	0.05
3	500 m	187 m	0.1
4	560 m	272 m	0.19

The values in Table 8 allow to predict the coherence gain for other given PS height differences. Assuming that the gain is zero for no height difference, a quadratic function describes the respective relation. It is graphed in Figure 91. For a height difference of 500 m a coherence gain of nearly 0.6 can be expected. Some predicted values are provided in Table 9.

Table 9: some predicted values for the coherence gain

PS height difference	predicted coherence gain
100 m	0.034
200 m	0.110
300 m	0.228
400 m	0.388
500 m	0.590

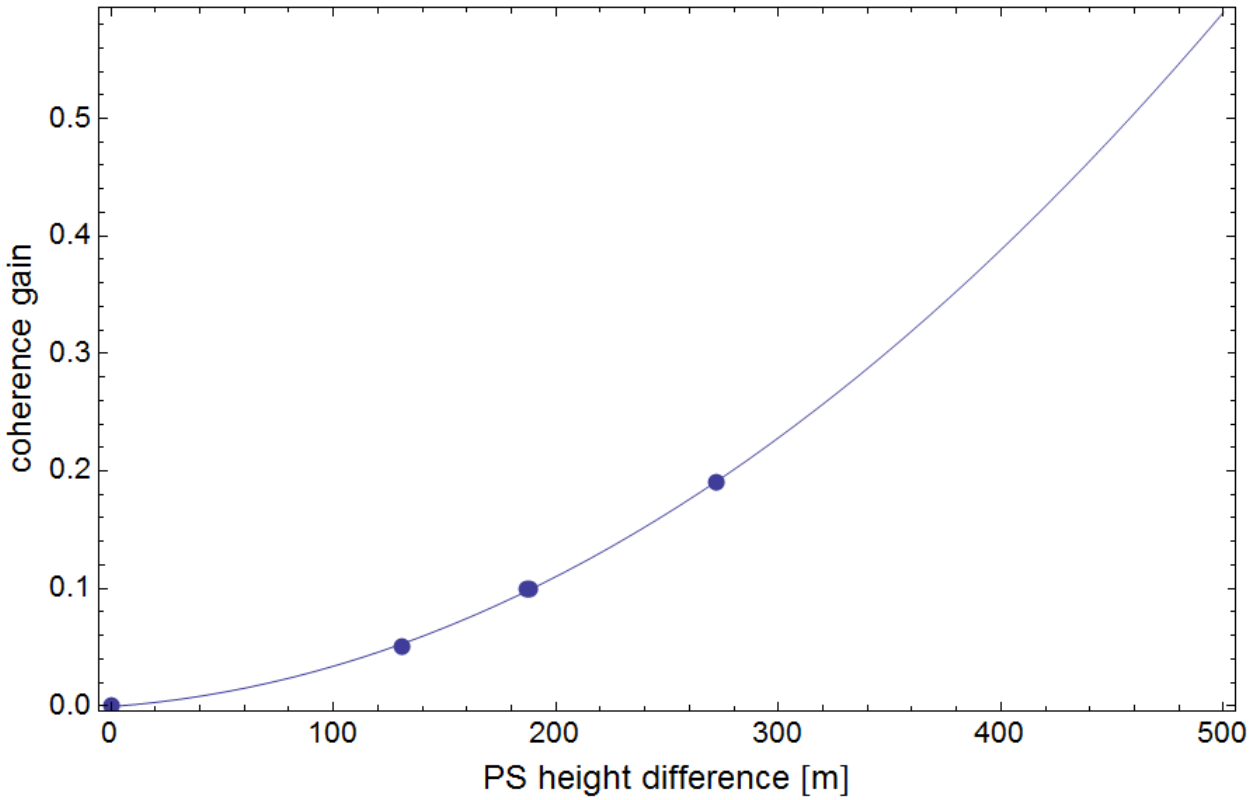

Figure 91: predicted coherence gain for a given PS height difference based on the measured values (blue dots) by a quadratic fit.

The practically measured coherence gain of 0.1 can make a significant difference for the estimation in mountainous areas. In every periodogram, sidelobes result caused by the limited observation time and baseline range. Sidelobes can be amplified by large data gaps and the irregular sampling. Now, the estimation can better detect the most likely estimate in the periodogram. Two examples are visualized in Figure 92 and Figure 93. The first example demonstrates that even a distance of over 2000 m can be bridged with the atmosphere correction in a difficult mountainous area.

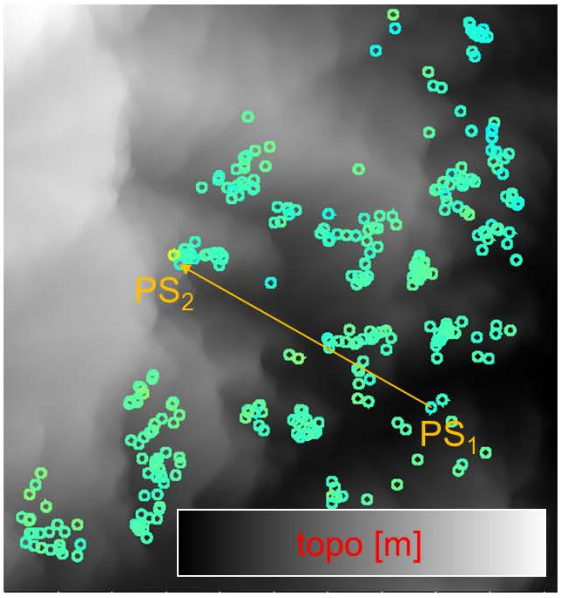

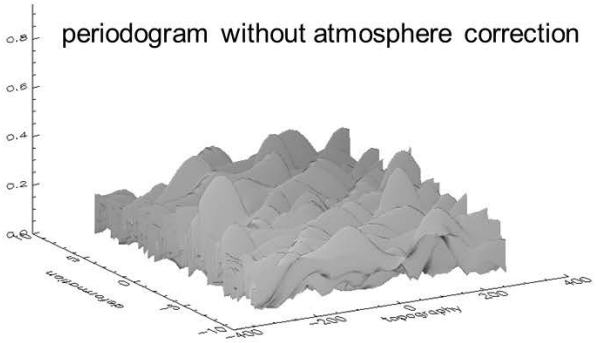

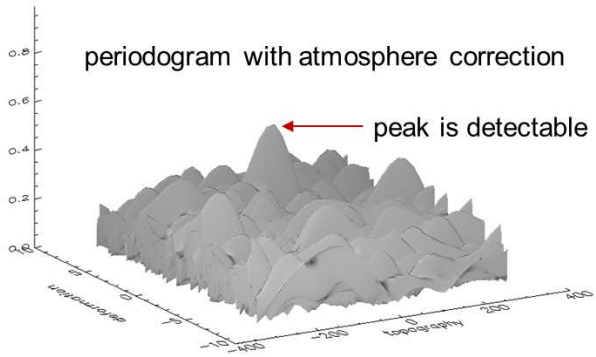

$\Delta h_{PS} = 480\ m$
$dist_{PS\ 1-2} = 2670\ m$

$\gamma_{uncorrect} = 0.4467$
$\gamma_{corrected} = 0.51978$
$\gamma_{gain} = 0.07$

Figure 92: only the atmosphere correction allows the estimation over the arc between PS_1 and PS_2. In this example, a distance of 2600 m can be bridged.

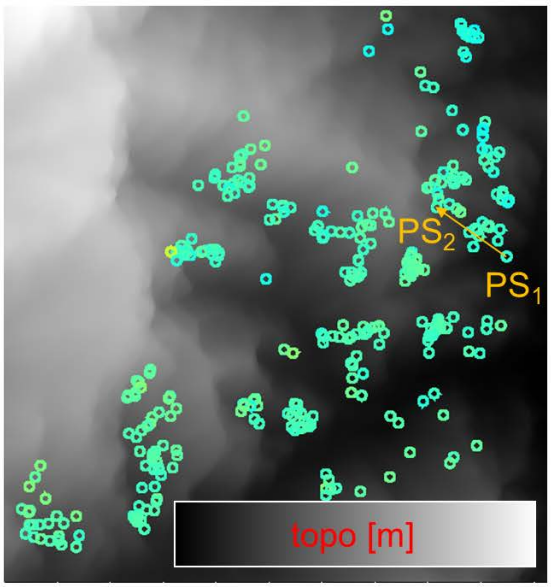

$\Delta h_{PS} = 280\ m$
$dist_{PS\ 1-2} = 800\ m$

$\gamma_{uncorrect} = 0.4680$
$\gamma_{corrected} = 0.5587$
$\gamma_{gain} = 0.09$

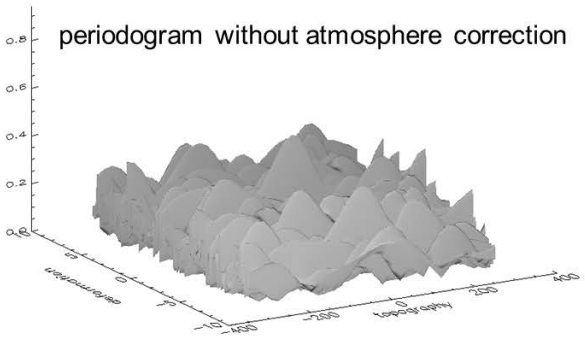

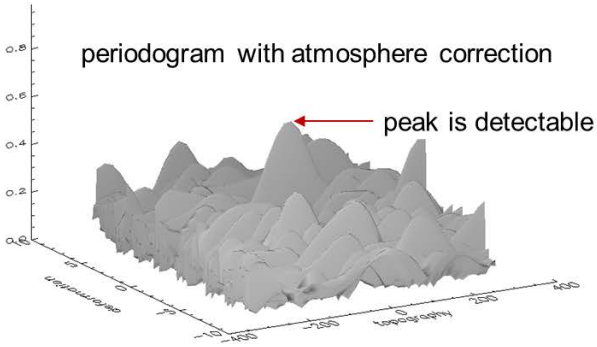

Figure 93: only the atmosphere correction allows the estimation over the arc between PS_1 and PS_2.

9 SUMMARY

Three different methods to estimate the vertical stratification effect in InSAR are described in this technical note. Their complexity is different and as a consequence also their characteristics are not the same.

The estimation directly from the InSAR data itself is most straight forward. The implementation of such a module is in the order of hours only. However, the atmosphere compensation which results from such a simple method is quite powerful and very good usable. It corrects for the dry as well as for the wet atmosphere effect without the need for additional data. Taking special care selecting suitable areas for the extraction of support points, the method is robust and can reduce the stratification effect even for long time interferograms. Nevertheless, the demonstrated limitations caused by the data quality dependence require an extrapolation in space and in time. The interpolation in space is necessary because the estimation is not possible at each scatterer location. Additionally, support points are difficult to find on top of the mountains Therefore, the estimation is based on moderate heights typically. And the extrapolation in time (e.g. by a cosine model fit) is required because of the temporal decorrelation in long time interferograms. The method gains robustness by limiting the estimation to a linear model only for the description of the vertical stratification. This makes the correction in the PSI processing straight forward. This is a consequence of the correction of a height difference only. I.e. the correction does not depend on the actual absolute height of a scatterer. However, the fitted dependency (third order) in the NWP (Figure 74) shows that the linear approximation by the direct estimation is a coarse approximation only and valid only for the small height range supported by the data. Another drawback is the limited applicability in case the test site is a volcano. In such a case, motion can be expected and interferes with the stratification estimation introducing a systematic bias. As a consequence, the stratification compensation biases the deformation estimation.

The GPS based zenith path delay provides an alternative data source for the troposphere effect mitigation. The technical problems as the large distance of the GPS station to the PS location, the deviation in the altitude of the GPS and the PS as well as the line of sight effect in contrast to the zenith GPS measurement are solved. However, the applicability of this method is limited due to the temporal availability of GPS measurements (typically later than year 2000) and the spatial coverage of GPS station. This is the reason, the zenith path delay cannot be used for ERS data processing.

The estimation from NWP is a newly developed method and considered the state of the art at the moment and an ongoing evolving technique. The effort to implement such a processor prototype is in the order of one to two years. In practice, this technique estimates the wet and dry delay from independent input data about the atmosphere state on a coarse grid. This assessment demonstrated a systematic gain in the coherence for the relative PSI estimation (i.e. between two persistent scatterers) in mountainous areas. Typically, the coherence improvement is in the order of ten percent compared to uncompensated estimations. Besides, this coherence gain allows bridging larger topography differences avoiding isolated i.e. unreferenced PS-clusters. In the developed troposphere effect mitigation processor (TEMP), the vertical stratification effect can be

estimated for any location in the scene including the top of the mountains. Compared to the straight forward direct estimation, the model copes with non-linear effects and considers also the absolute height of a scatterer.

10 BIBLIOGRAPHY

[1] Z. Li, E. Fielding, P. Cross and P. Muller, “Interferometric synthetic aperture radar atmospheric correction: GPS topographytopography-dependent,” *J. Geophys. Res,* vol. 111, 2006.

[2] Cong and M. Eineder, “Volcano Deformation Measurement Using Persistent Scatterer Interferometry With Atmospheric Delay Corrections,” *Proceedings EUSAR 2012,* 2012.

[3] R. Holley, G. Wadge and M. Zhu, “New insights into the nature and effects of the water vapour field on InSAR measurements over Etna,” *Proceedings of FRINGE,* p. http://earth.esa.int/fringe07/participants/159/pres_159_holley.pdf, 2007.

[4] D. Perissin, E. Pichelli, A. Ferretti, F. Rocca and N. Pierdicca, “The MM5 Numerical Model to correct PSInSAR Atmospheric Phase Screen,” *Proceedings of FRINGE,* 2009.

[5] R. F. Hanssen, “Atmospheric heterogeneities in ERS tandem SAR interferometry,” *DEOS Report No.98.1,* 1998.

[6] E. K. Smith and S. Weintraub, “The constants in the equation for atmospheric refractive index at radio frequencies,” *Proc. IRE,* vol. 41, pp. 1035-1037, 1953.

[7] C. Bruyninx, “The EUREF permanent network: A multi-disciplinary network serving surveyors as well as scientists,” *GeoInformatics,* vol. vol. 7, p. pp. 32–35, 2004.

[8] “SINEX file format,” [Online]. Available: ftp://epncb.oma.be/pub/data/format/sinex_tropo.txt. [Accessed Jan. 2012].

[9] “EUREF product download,” [Online]. Available: ftp://igs.bkg.bund.de/EUREF/products/. [Accessed Jan. 2012].

[10] M. Eineder, C. Minet, P. Steigenberger, X. Y. Cong and T. Fritz, “Imaging geodesy - toward centimeter-level ranging accuracy with TerraSAR-X,” *IEEE Trans. Geosci. Remote Sens.,* Vols. vol. 49, no. 2, p. pp. 661–671, Feb. 2011.

[11] “EUREF stations map,” [Online]. Available: http://www.epncb.oma.be/_networkdata/stationmaps.php. [Accessed Jan. 2012].

[12] J. Boehm, A. Niell, P. Tregoning and H. Schuh, “Global Mapping Function (GMF): A new empirical mapping function based on numerical weather model data,” *Geophys. Res. Lett.,* vol. LXXXXX, no. doi:10.1029/2005GL025546, 2006.

[13] H. Breit, T. Fritz, U. Balss, M. Lachaise, A. Niedermeier and M. Vonavka, “TerraSAR-X SAR processing and products,” *IEEE Trans. Geosci. Remote Sens.,* vol. vol. 48, no. no. 2, p. pp. 727–740, Feb. 2010.

[14] National Center for Atmospheric Research (NCAR), “http://www.wrf-model.org,” [Online]. [Accessed 2012].

[15] W. C. Skamarock, J. Klemp, J. Dudhia, D. Gill, D. Barker, W. Wang and J. Powers, "A Description of the Advanced Research WRF Version 3," *NCAR Technical Note TN-468+STR,* p. 113, 2008.

[16] S. Saha, S. Moorthi, X. Wu, J. Wang, S. Nadiga, P. Tripp, H.-L. Pan, D. Behringer, Y.-T. Hou, H.-y. Chuang, M. Iredell, M. Ek, J. Meng and R. Yang, "The NCEP Climate Forecast System Version 2," 2011.

[17] J. Mangum, "Atmospheric Refractive Signal Bending and Propagation Delay," *online: https://safe.nrao.edu/wiki/pub/Main/RefBendDelayCalc/RefBendDelayCalc.pdf,* 16 August 2009.

[18] J. M. Rüeger, "Refractive Index Formulae for RadioWaves," *JS28: Integration of Techniques and Corrections to Achieve Accurate Engineering,* 19-26 April 2002.

[19] University of Wyoming, 2012. [Online]. Available: http://weather.uwyo.edu/upperair/sounding.html. [Accessed 2012].

[20] I. Durre, R. S. Vose and D. B. Wuertz, "Overview of the Integrated Global Radiosonde Archive," *Journal of Climate,* vol. 19, pp. 53-68, 1 2006.

[21] G. Brussaard and P. A. Watson, "Atmospheric modeling and millimetre wave propagation," p. 254, 1995.

[22] X. Y. Cong, U. Bals, M. Eineder and T. Fritz, "Imaging Geodesy—Centimeter-Level Ranging Accuracy With TerraSAR-X: An Update," *Geoscience and Remote Sensing Letters,* vol. 9, no. 5, 2012.

11 ACKNOWLEDGEMENT

This research was partially funded by ESA in the course of the Terrafirma project. I would like to thank Philippe Bally for the respective management and support. Finally, I also wish to acknowledge the help of Larry Oolman from the Department of Atmospheric Science at the University of Wyoming for the uncomplicated help allowing the full and practical exploitation of the Integrated Global Radiosonde Archive (IGRA) data as well as of Dr. Lifeng Luo at Michigan State University for the support regarding the CFSR data.

12 APPENDIX

All the following data are obtained from the university Wyoming [19].

12.1 NWP DATA OF THESSALONIKI (06. JUNE 1992 12:00)

PRES hPa	HGHT m	TEMP C	DWPT C	RELH %	MIXR g/kg	DRCT deg	SKNT knot	THTA K	THTE K	THTV K
1015.0	4	24.8	15.8	57	11.24	220	6	296.7	329.4	298.7
1008.0	66	23.0	12.0	50	8.81	190	7	295.5	321.2	297.0
1000.0	138	22.2	12.2	53	9.00	155	8	295.4	321.6	296.9
925.0	808	16.0	11.2	73	9.11	145	8	295.7	322.2	297.3
891.0	1125	12.6	10.3	86	8.90	158	6	295.3	321.2	296.9
886.0	1173	12.4	10.3	87	8.95	160	6	295.6	321.7	297.2
850.0	1521	11.0	6.8	75	7.34	175	4	297.7	319.4	299.0
785.0	2181	7.0	4.8	86	6.91	216	8	300.2	320.9	301.5
748.0	2577	4.4	-1.6	65	4.57	241	10	301.6	315.6	302.4
714.0	2955	4.2	-19.8	16	1.12	265	12	305.4	309.2	305.6
710.0	3001	4.0	-19.0	17	1.21	268	12	305.6	309.7	305.9
700.0	3116	3.0	-16.0	23	1.58	275	13	305.8	311.0	306.1
500.0	5750	-14.7	-26.7	35	0.87	265	25	315.1	318.1	315.2
479.0	6075	-16.5	-32.5	24	0.52	269	26	316.7	318.6	316.8
442.0	6677	-21.3	-32.3	36	0.58	276	28	318.0	320.1	318.1
430.0	6881	-22.5	-42.5	14	0.21	279	29	319.0	319.8	319.0
400.0	7410	-26.9	-42.9	21	0.22	285	31	319.9	320.8	320.0
389.0	7610	-28.8	-44.8	20	0.18	284	31	320.0	320.7	320.1
300.0	9410	-43.3				275	34	324.2		324.2
275.0	9989	-48.1				277	38	325.4		325.4
250.0	10610	-52.5				280	43	327.9		327.9
200.0	12020	-61.1				270	43	335.9		335.9
194.0	12209	-62.1				280	46	337.2		337.2
165.0	13228	-54.3				277	42	366.2		366.2
150.0	13840	-53.1				275	40	378.4		378.4
139.0	14331	-52.7						387.4		387.4

12.2 NWP DATA OF THESSALONIKI (31. DECEMBER 1996 12:00)

PRES hPa	HGHT m	TEMP C	DWPT C	RELH %	MIXR g/kg	DRCT deg	SKNT knot	THTA K	THTE K	THTV K
1015.0	4	6.6	6.2	97	5.89	0	0	278.6	294.8	279.6
1003.0	101	5.2	4.2	93	5.18	124	11	278.1	292.4	279.0
1000.0	126	6.0	5.1	94	5.54	155	14	279.1	294.5	280.1
987.0	234	8.4	4.8	78	5.49	161	13	282.6	298.0	283.5
949.0	557	6.2	2.5	77	4.85	179	9	283.6	297.3	284.4
925.0	768	7.4	0.4	61	4.28	190	7	286.9	299.3	287.6
907.0	930	8.2	-1.8	49	3.71	203	9	289.3	300.3	290.0
850.0	1463	5.0	-4.0	52	3.36	245	14	291.4	301.4	292.0
700.0	3014	-6.7	-9.9	78	2.59	255	23	295.0	303.0	295.5
682.0	3217	-8.5	-11.3	80	2.38	254	23	295.2	302.6	295.7
653.0	3553	-9.7	-18.7	48	1.35	252	24	297.6	301.9	297.8
619.0	3962	-13.7	-18.4	68	1.46	250	25	297.6	302.2	297.8
500.0	5550	-24.5	-35.5	35	0.37	240	28	303.1	304.4	303.2
453.0	6263	-28.7	-50.7	10	0.08	236	28	306.5	306.8	306.5
400.0	7140	-36.7	-54.7	14	0.06	230	28	307.2	307.4	307.2
357.0	7917	-44.1				236	30	307.4		307.4
300.0	9060	-54.1				245	32	309.0		309.0
294.0	9189	-55.3				247	34	309.1		309.1
250.0	10210	-59.9				265	48	316.9		316.9
239.0	10490	-61.5				265	53	318.6		318.6
230.0	10728	-61.7				265	52	321.8		321.8
213.0	11210	-55.9				265	51	337.9		337.9
200.0	11610	-57.1				265	50	342.2		342.2
194.0	11803	-57.3				264	51	344.9		344.9
174.0	12495	-54.3				260	55	360.7		360.7
150.0	13440	-57.1				255	61	371.5		371.5
143.0	13740	-57.9				260	67	375.2		375.2
118.0	14947	-61.1				263	58	390.5		390.5
100.0	15980	-59.5				265	50	412.5		412.5
94.4	16339	-61.7				263	46	415.0		415.0
89.8	16652	-57.1				262	43	430.1		430.1
75.2	17777	-56.7				257	32	453.4		453.4
70.0	18230	-58.5				255	27	458.9		458.9
55.2	19705	-63.5						479.7		479.7
51.8	20096	-62.3						491.3		491.3

12.3 NWP DATA OF THESSALONIKI (23. FEBRUARY 1997 12:00)

PRES hPa	HGHT m	TEMP C	DWPT C	RELH %	MIXR g/kg	DRCT deg	SKNT knot	THTA K	THTE K	THTV K
1023.0	4	16.2	6.2	52	5.84	270	10	287.5	304.2	288.5
1013.0	87	15.8	-3.2	27	2.99	293	12	287.9	296.8	288.4
1006.0	146	15.4	-3.1	28	3.04	310	14	288.0	297.1	288.6
1000.0	196	15.0	-3.0	29	3.08	315	15	288.1	297.3	288.7
925.0	849	9.6	-4.4	37	3.00	325	16	289.1	298.1	289.6
850.0	1543	3.0	-5.0	56	3.12	345	21	289.3	298.6	289.8
844.0	1600	2.6	-5.4	56	3.04	346	22	289.4	298.5	290.0
771.0	2322	-2.2	-10.2	54	2.29	0	31	291.8	298.9	292.2
733.0	2725	-4.9	-12.9	53	1.94	0	33	293.1	299.2	293.5
700.0	3087	-6.1	-16.1	45	1.56	0	35	295.7	300.7	296.0
690.0	3200	-6.9	-16.9	45	1.48	358	36	296.0	300.8	296.3
664.0	3499	-8.1	-30.1	15	0.48	351	38	297.9	299.6	298.0
660.0	3546	-8.3	-30.3	15	0.47	350	38	298.2	299.9	298.3
627.0	3943	-9.9	-31.9	15	0.42	348	39	300.8	302.3	300.9
598.0	4307	-11.9	-40.9	7	0.18	346	40	302.6	303.3	302.6
500.0	5650	-22.3	-46.3	9	0.12	340	43	305.8	306.2	305.8
409.0	7090	-32.7	-50.4	15	0.09	335	48	310.4	310.7	310.4
400.0	7250	-33.9	-50.9	16	0.09	335	47	310.9	311.2	310.9
398.0	7285	-34.1	-50.1	18	0.10	335	47	311.0	311.4	311.1
377.0	7662	-35.1	-69.1	2	0.01	332	48	314.6	314.6	314.6
300.0	9210	-47.1				320	54	318.9		318.9
289.0	9454	-49.0				320	53	319.5		319.5
253.0	10324	-55.9				320	51	321.7		321.7
250.0	10400	-56.3				320	51	322.2		322.2
226.0	11025	-59.9				325	51	326.2		326.2
204.0	11659	-63.5				335	49	330.2		330.2
200.0	11780	-63.3				335	50	332.4		332.4
189.0	12134	-55.5				343	52	350.3		350.3
179.0	12483	-53.5				351	54	359.1		359.1
177.0	12555	-52.9				353	54	361.2		361.2
174.0	12665	-53.0				355	55	362.8		362.8
150.0	13620	-54.3				350	47	376.3		376.3
109.0	15628	-61.9				345	52	397.9		397.9
100.0	16160	-62.5				340	44	406.7		406.7
82.0	17388	-60.6				325	36	434.2		434.2
80.8	17480	-60.5				327	35	436.4		436.4
70.0	18370	-61.5				345	22	452.5		452.5
68.0	18549	-61.5				345	20	456.2		456.2
66.0	18732	-62.9				345	17	457.1		457.1
63.0	19016	-65.1				340	15	458.3		458.3
61.2	19193	-66.5				331	16	459.1		459.1
57.0	19627	-64.2				310	20	473.7		473.7
54.4	19911	-62.7				312	21	483.5		483.5
50.0	20430	-62.9				315	22	494.8		494.8
47.0	20812	-62.3				320	22	505.2		505.2
41.9	21522	-61.1				311	28	524.9		524.9
39.0	21968	-60.9				305	31	536.3		536.3
36.0	22466	-60.7				315	27	549.3		549.3
31.3	23336	-60.3				287	17	572.7		572.7
31.0						285	16			

12.4 NWP DATA OF THESSALONIKI (27. JULY 1997 12:00)

PRES hPa	HGHT m	TEMP C	DWPT C	RELH %	MIXR g/kg	DRCT deg	SKNT knot	THTA K	THTE K	THTV K
1012.0	4	27.0	13.0	42	9.38	340	28	299.1	326.9	300.8
1000.0	105	25.0	6.0	30	5.90	350	33	298.1	315.8	299.2
974.0	333	22.8	5.9	33	6.00	355	31	298.2	316.2	299.3
925.0	780	18.6	5.6	42	6.20	345	31	298.3	316.9	299.4
882.0	1186	14.2	5.2	55	6.32	339	32	297.9	316.7	299.0
850.0	1497	11.6	3.6	58	5.86	335	33	298.3	315.9	299.3
811.0	1887	8.0	2.0	66	5.48	335	34	298.5	315.0	299.5
796.0	2040	7.4	0.8	63	5.11	335	34	299.4	314.9	300.4
732.0	2726	4.6	-4.7	51	3.69	340	20	303.7	315.3	304.4
718.0	2884	4.0	-6.0	48	3.42	331	20	304.7	315.5	305.3
708.0	2998	3.2	-6.8	48	3.27	325	20	305.0	315.4	305.6
700.0	3090	2.6	-7.4	48	3.15	325	19	305.3	315.4	305.9
655.0	3618	-1.0	-11.0	47	2.53	345	17	307.1	315.3	307.6
601.0	4303	-5.7	-15.7	45	1.88	328	24	309.3	315.6	309.7
589.0	4461	-4.7	-20.7	27	1.26	324	25	312.3	316.6	312.5
563.0	4814	-6.4	-25.1	21	0.89	315	29	314.4	317.5	314.5
552.0	4968	-7.1	-27.1	19	0.76	315	30	315.3	318.0	315.4
500.0	5730	-12.7	-31.7	19	0.54	315	34	317.5	319.5	317.6
462.0	6331	-17.1	-43.1	9	0.18	315	36	319.3	320.0	319.3
446.0	6593	-19.1	-39.7	14	0.27	315	37	320.0	321.1	320.0
411.0	7201	-23.7	-31.7	48	0.66	311	47	321.6	324.0	321.7
400.0	7400	-25.1	-33.1	47	0.59	310	50	322.3	324.5	322.4
339.0	8577	-34.1	-50.1	18	0.12	301	74	325.6	326.1	325.6
320.0	8980	-32.9	-58.9	6	0.04	298	83	332.7	332.9	332.7
300.0	9430	-36.3	-62.3	5	0.03	295	92	334.1	334.2	334.1
289.0	9684	-38.2				295	93	335.0		335.0
251.0	10643	-45.3				300	78	338.2		338.2
250.0	10670	-45.3				300	78	338.6		338.6
200.0	12140	-50.9				295	59	352.0		352.0
174.0	13039	-54.8				270	49	359.9		359.9
165.0	13382	-56.3				275	48	362.9		362.9
150.0	13990	-55.9				300	40	373.6		373.6
149.0	14032	-55.9				300	39	374.2		374.2
125.0	15146	-56.4				260	22	392.7		392.7
100.0	16560	-56.9				240	18	417.5		417.5
96.0	16819	-56.1				250	15	423.9		423.9
95.8	16832	-56.1						424.2		424.2

-- End of document --